The University of Sheffield

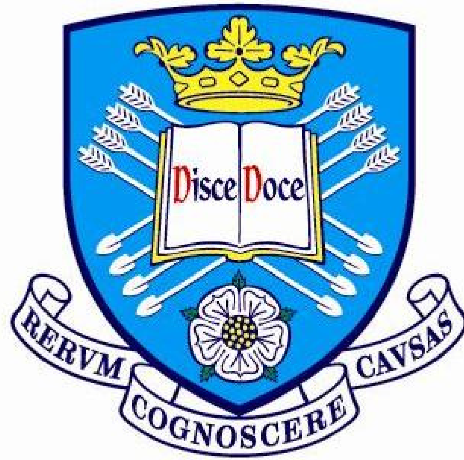

Application of Focused Ion Beam for Micro-machining and Controlled Quantum Dot Formation on Patterned GaAs Substrate

by

Haoyu Zhang

A thesis submitted for the degree of Doctor of Philosophy

Department of Electronic and Electrical Engineering

December 2013

Abstract

This project is a study based on the application of focused ion beam (FIB) instrumentation, which has been widely used in fields such as electronic engineering, materials science, semiconductor technology and nanotechnology. We used a Ga^+ source focused ion beam column from Orsay Physics mounted on a JEOL 6500F scanning electron microscopy, which forms a SEM-FIB dual-beam instrument.

This project consists of a few experimental projects based on the applications of the FIB in electronic engineering. The experimental work will demonstrate the micro-machining capability of the FIB system. The projects include the TEM/STEM cross-sectional sample preparation and the fabrication of a ring shaped aperture and a coded aperture for (S)TEM imaging.

The major project is to study InAs quantum dots grown on a FIB patterned GaAs (100) substrate, in order to produce regular arrays of quantum dots at specific sites. In(Ga)As quantum dots have been a very popular topic in electronic engineering for a long time. InGaAs quantum dots have an energy band gap between 0.66eV and 1.41eV, covering the range from infrared (IR) to visible light, which can be used for constructing infrared detectors, solar cells and etc. Regular quantum dot arrays are expected to have better size distribution and high uniformity over a small area with respect to randomly located self-assembled quantum dots, which results in better opto-electronic performance. Overgrowth of a FIB patterned substrate is one of the techniques to produce regular quantum dot arrays. Island-shaped quantum dots are nucleated at specific locations where the ion beam has formerly patterned the surface. Different ion beam patterning parameters are compared and optimized, including accelerating voltage, probe current, dwell time, pitch, growth temperature and thickness of deposited InAs. We have determined the range of the ion beam parameters and the overgrowth conditions, which consistently produce regular quantum dot arrays at the patterned areas without nucleation outside the patterned areas. The relationship between the size of the formed islands and the patterning parameters is investigated by analysing SEM images and AFM images. Micro-photoluminescence and TEM EDX analysis are applied to study the islands formed, to find out the optoelectronic performance and the chemical composition.

Acknowledgement

During the last few years of my academic career, there are many people have kindly offered me advice and help. The list is too long to name them all, but there are some people, who must be mentioned by name.

First of all, I'd like to acknowledge my supervisor, Dr. Thomas Walther, for his continuing support, wise advice and guidance through my entire PhD study. I really appreciate his patience and understanding of my language problems, especially at my writing up stage. By studying in his group, I have learned how to systemically plan and manage the project, and also critically and objectively analyse results. I always learn something new from the discussion with him, which is a very enjoyable experience. I also want to express my sincere appreciation to Prof. Anthony George Cullis, who introduced me to Dr. Walther and offered me this opportunity to work in this group.

I also want to thank Dr. Ian Mark Ross, who gaves me the training in SEM-FIB dual-beam microscopy. Thanks for spending a great amount of time and effort to maintain all the equipment and labs, which has kept my work going smoothly. He kindly offers me all his valuable knowledge and experience concerning the operation of the microscope and micro-machining. When I was confused about the project or faced technical issues, the discussions with him have been always helpful and productive.

Many thanks to all the people who helped me and contributed to my project in the last few years, from the EEE department, North Campus, Sorby centre etc. I would like to acknowledge in particular Prof. Mark Hopkinson, Dr. Shiyong Zhang, Dr. David Child and Dr. Peng Zeng for helping me growing, investigating and testing the sample and producing fruitful results.

I have been enjoying my PhD career very much both inside and outside the lab. Many thanks to our group members who had inspired me and shared coffee with me: Arefeh Taghi Khani, Dr. Leonardo Lari, Dr Houari Amari and Dr. Yang Qiu.

I'd like to thanks all my friends and family in the UK and China, who makes my life so colourful and full of laughs. Especially my mother, Zhihong Zhang; she always encourages and supports me in all aspects, shares my happiness and cheers me up when I feel depressed and struggle; without her love and care, it is impossible to make this come ture. In the end, thanks to my lovely chinchilla, Xiaoguai: you did well, you are the best.

Published work

1. H. Amari, L. Lari, **H. Y. Zhang**, L. Geelhaar, C. Cheze, M. J. Kappers, C. McAleese, C. J. Humphreys and T. Walther, "Accurate calibration for the quantification of the Al content in AlGaN epitaxial layers by energy-dispersive X-ray spectroscopy in a Transmission Electron Microscope," in *17th International Conference on Microscopy of Semiconducting Materials 2011*. J. Phys.: Conf. ser. (eds: T. Walther and P. A. Midgley) vol. 326.

2. H. Amari, **H. Y. Zhang**, L. Geelhaar, C. Cheze, M. J. Kappers and T. Walther "Nanoscale EELS analysis of elemental distribution and band-gap properties in AlGaN epitaxial layers," in *17th International Conference on Microscopy of Semiconducting Materials 2011*. J. Phys.: Conf. ser. (eds: T. Walther and P. A. Midgley) vol. 326.

3. **H. Zhang**, I. M. Ross, M. Hopkinson, S. Zhang and T. Walther, *Study of Controlled Quantum Dot Formation on Focused Ion Beam Patterned GaAs Substrates*, Proc. IEEE-Nano, Brimingham, 2012.

4. **H. Zhang**, I. M. Ross, T. Walther, and Iop, "Study of site controlled quantum dot formation on focused ion beam patterned GaAs substrate," in: *18th Microscopy of Semiconducting Materials Conference*. vol. 471, 2013.

5. **H. Zhang** and T. Walther, “Controlled Quantum Dot Formation on Focused Ion Beam-patterned GaAs Substrates” in: *FIB Nanostructures*, Z. M. Wang, Eds., Switzerland: Springer International, 2014, chapter 11.

Table of contents

Chapter 1. Introduction 1

Chapter 2. Literature review of focused ion beam technology and strained-layer epitaxy 4

2.1. Focused ion beam instrumentation 4

2.1.1. Sample chamber 5

2.1.2. Source of ions 7

2.1.3. Ga^{+} Ion column design 10

2.1.4. Secondary electron detector 12

2.1.5. Beam alignment techniques 15

2.1.6. Micro manipulator 16

2.2. Focused ion beam damage 17

2.2.1. Ion beam milling and sputter yield 17

2.2.2. Nano-patterning surfaces 22

2.3. Molecular beam epitaxy 24

2.4. Strained-layer epitaxy of InGaAs/GaAs (001) 26

Chapter 3. FIB characterisation and milling of lamellae samples 28

3.1. Probe current measurement 28

3.2. Ion beam size measurement 29

3.2. TEM/STEM cross-sectional sample preparation by FIB 37

3.2.1. Standard experimental work procedure 37

3.2.2. Possible problems and solutions 39

Chapter 4. Aperture micro-machining for TEM applications 42

4.1. Ring shaped aperture fabrication 42

4.2. Coded aperture fabrication 43

Chapter 5. Controlled quantum dot formation on FIB patterned (001) GaAs substrates 50

5.1. Motivation of fabricating QD arrays 50

5.2. Localized QD growth on patterned substrates 51

Chapter 6. Patterning and growth in practice 54

6.1. Overgrowth of the 1st wafer 54

6.1.1. Pattern design and fabrication 54

6.1.2. Difficulties during fabrication 58

6.1.3. Result and further improvement 58

6.2. Overgrowth of the 2nd Wafer 61

6.2.1. Improved wafer layout, pattern design and overgrowth 61
6.2.2. Results for wafer 2 65
6.2.3. Micro-photoluminescence investigation 72
6.2.4. TEM cross-sectional study of InGaAs QDs grown 75
6.3. Overgrowth of 3rd wafer 81
6.3.1. Improved wafer layout and pattern design and overgrowth 81
6.3.2. Results 85
Chapter 7. Conclusion 94
7.1. Summary of the main results 94
7.2. Outlook for further study and research 97
Reference 99

Abbreviations:

ABF: annular bright-field

ADF: annular dark-field

AFM: atomic force microscope

BSE: backscattered electron

CVD: Chemical vapor deposition

EDXS: energy dispersive X-ray spectroscopy

FFT: Fast Fourier Transform

FIB: focused ion beam

GIS: gas injection system

ISRT: Ion Stopping and Range Tables

LED: light-emitter diode

LMIS: liquid metal ion source

MBE: molecular beam epitaxy

MURA: modified uniformly redundant array

PL: micro-photoluminescence

PMT: Photomultiplier tubes

QD: quantum dot

RHEED: reflection high-energy electron diffraction

SE: secondary Electron

SEM: scanning electron microscopy

SK: Stranski-Krastanow

SRIM: The Stopping and Range of Ion in Matter

STEM: scanning transmission electron microscope

TEM: transmission electron microscopy

UHV: ultra-high vacuum

URA: uniformly redundant array

Chapter 1. Introduction

This project is a study based on the use and application of focused ion beam (FIB) instrumentation, which has played a critical role in micro-engineering and nano-science for many years, to fields such as electronic engineering, materials science [1], semiconductor technology [2], nanotechnology, microscopy analysis etc. Since engineers and scientists have stepped into the world of micrometres, even nanometres, demand for high precision machining and fabrication is increasing.

A FIB system has certain advantages and disadvantages compared with other lithographic and microscopy instrumentation. Compared with optical lithography, ion beam patterning is a much easier and quicker way to produce patterns. Because it dose not involve any chemical resist or physical mask preparation. Also, FIB has fewer restrictions on the materials used as the substrates and does not induce any contamination. However, the undesirable but also unavoidable Ga^+ implantation and the crystallographic damage induced by this can cause problems. The working field-of-view of our ion beam patterning system is smaller than typical field-of-view in e-beam lithography, which is a major limitation of the ion beam patterning in industry-level fabrication. When the FIB is used as an imaging tool, the inherent heavy mass of the primary ions and the solid-ion interaction provides more information than the standard SEM. Comparing to electron microscope, the ion beam microscope takes less effect from the built up static charge, which makes it a better imaging tool for insulating material. The sputtered atoms from the target can produce both a mass spectrum image and a backscattered ion image with corresponding equipments and detectors being added, which our FIB dose not have. The channelling effect of the implanted ions also provides contrast based on crystal orientation differences in the target. 3D-nanotomography is a unique imaging technology of a FIB-SEM dual-beam platform, which can be used to investigate complex microstructures. The specimen is sliced by FIB and imaged by SEM with a narrow and reproducible spacing. The slice spacing can have a thickness in the same range of magnitude of the resolution of the SEM images. By stacking and applying drift correction algorithms to these captured secondary electron images, a 3D model of the specimen can be built with a voxel resolution in the nanometre scale, which is useful for materials science.

This project consists of a few experimental projects based on the applications of FIB in the Department of Electrical and Electronic Engineering of the University of Sheffield, which has a Ga^+ source focused ion beam column from Orsay Physics mounted on a JEOL 6500F scanning electron microscopy (SEM). This combination forms a SEM-FIB dual-beam instrument, which is described in detail in chapter 2. Some literature and background reviews related to later experimental work are presented in chapter 2 as well. Then, the experimental work starts with measuring the beam size of the SEM and FIB and describes the application of FIB to Transmission Electron Microscope (TEM) cross-sectional sample preparation in chapter 3. In the following chapter 4, a ring shaped aperture with a diameter of 40µm and a 100µm x 100µm coded aperture are designed and fabricated by FIB machining. This work demonstrates the micro-machining capability of the FIB in practical application. Chapter 5 contains a presentation of the main project, which is the study of InAs quantum dots grown on a FIB patterned GaAs (100) substrate. Regular arrays of quantum dot have been produced by molecular beam epitaxy deposition on the patterned areas. The following chapter 6 will present all the practical experiments sequentially, including patterning, overgrowth and investigation of each individual wafer. The conclusion chapter summaries all the results and provides an outlook onto possible further work.

InGaAs quantum dots (QD) have been a very popular topic in electronic engineering for a long time. InGaAs QDs have an energy band gap between 0.66eV and 1.41eV, covering the range from infrared (IR) to visible light and can be used for constructing infrared detectors, light-emitting diodes (LEDs), laser diodes and solar cells. Regular quantum dot arrays are expected to have better opto-electronic performance than randomly located self-assembled quantum dots. Overgrowth of a FIB patterned substrate is one of the techniques to produce regular quantum dot arrays. We studied the ion beam patterning parameters and resulting nano-structures before and after overgrowth. We structured three GaAs wafers with different ion beam parameters, including different accelerating voltages, probe currents, dwell times and pitches of the arrays. The patterning parameters and growth conditions were optimized to consistently produce regular QD arrays over the patterned substrates. We also changed the overgrowth procedure for the 3rd wafer to evaluate the influence of different thicknesses of InAs. The influences of these parameters are systematically analysed, focusing on the rate of successful island formation, dimension, photoluminescence performance and the chemical composition of the formed islands. The heights and diameters of the islands were measured

by atomic force microscope (AFM) imaging and scanning electron microscope (SEM) secondary electron imaging. Micro-photoluminescence was performed inside and outside patterned regions, in order to compare their optoelectronic properties. STEM cross-sectional analysis has been performed for a row of quantum dots to estimate the chemical composition inside the structures.

Chapter 2. Literature review of focused ion beam technology and strained-layer epitaxy

This section will introduce the instrumental principles and some background theory of focused ion beam technology and its applications. The content is divided into four parts, which consist of focused ion beam (FIB) instrumentation, ion beam damage, InGaAs/GaAs epitaxial growth and molecular beam epitaxy. In this chapter, no experimental work is described apart from some simulations.

2.1. Focused ion beam instrumentation

In this project, a JEOL JSM-6500F SEM combined with an Orsay Physics CANION 31 MPlus ion column is used as the main experimental platform. Occasionally, an FEI Quanta3D FIB was used for specific applications, such as TEM sample preparation and lift-out.

Figure 2-1 A photograph of the FIB system being used in this project, a JEOL JSM-6500F SEM combined with an Orsay Physics CANION 31 MPlus ion column.

A FIB system can be separated into several sub-systems. These are the source of ions, the ion optic column, the sample chamber and the detector. Some essential tools are introduced as well, such as the gas injection system and manipulator. The ion optics column alignment technique used is involved to provide a better understanding about how FIB lenses and components work. The FIB is a high vacuum system. In air, collisions would happen between the gas atoms or molecules and the ions travelling from the source to the sample. The source and column environment require ultra-high vacuum (order of 1.5×10^{-8} mbar) to avoid contamination and prevent electrical discharges in the high voltage ion column.

2.1.1. Sample chamber

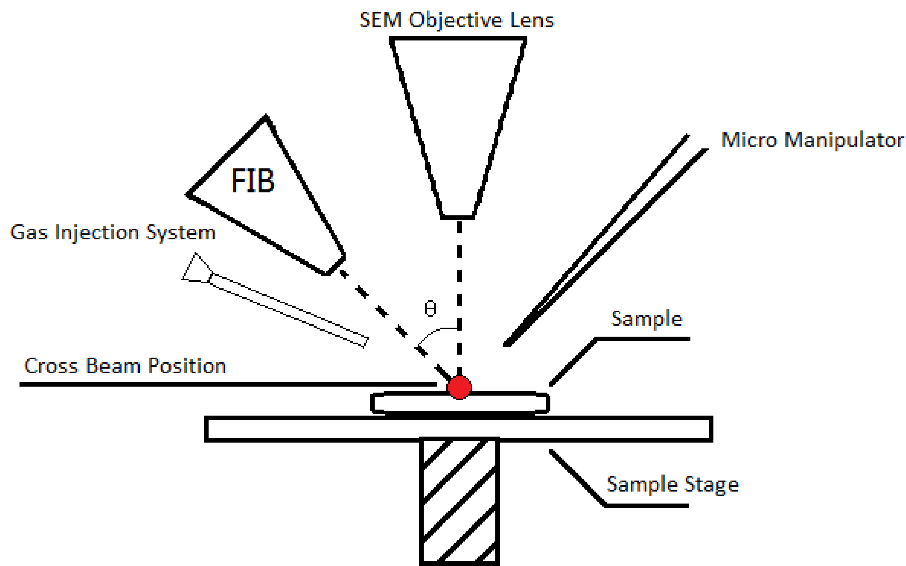

Figure 2-2 Sample chamber layout, including gas injection system and micro manipulator.

In a SEM/FIB dual beam system, two optical columns and a sample stage are positioned as shown in figure 2-2. The combination of the SEM and the FIB in one instrument pushes the capability of both techniques to a new level. FIB milling and SEM secondary electron imaging can operate simultaneously, which makes 'cut, look and measure' possible. By using the electron beam to image instead of using the ion beam, the damage is reduced or eliminated. It also makes material removal more controllable. Further tools can be added to the sample chamber, such as a gas injection system and a micro manipulator, to provide more functionality.

A standard sized sample (smaller than 1.5 inches) is loaded into the chamber through a loadlock. This design aims at preserving the high vacuum environment inside the chamber and reducing pumping time. Apart from the loadlock, a larger side door can be opened to load larger samples or for module installation and maintenance. The sample is placed on a five-axis stage. It can shift along X, Y and Z directions, and rotate or tilt. The stage movements in X and Y directions are driven by two stepper motors for location of sites at the micrometre scale. There is an angle ϴ of 55° between the ion beam column and the electron beam

column. During standard FIB operation, the stage moves along Z direction to position the sample at the cross-beam position; the sample can be tilted 55° to face the ion beam column perpendicularly, so that ion beam will have a vertical incidence.

Most modern FIBs are equipped with a gas injection system (GIS) and a micro manipulator, to enhance the capability and functionality. The major function of the GIS is site specific deposition or etching. For different applications, the material deposited varies. For prototype microcircuit repair or construction, the most widely used metals for deposition are tungsten and platinum, as a result of their excellent electric conductivity and availability of appropriate organo-metallic compound. Conducting metal is used to build circuits or establish connections between components. Another very useful application of a GIS is depositing a protection layer (carbon or tungsten) to prevent ion beam damage. A typical example is TEM sample preparation, which needs a protection layer deposited to protect the region of interest from ion implantation during milling. To produce deposition, a controllable amount of gas compound flows into the chamber through a sharp capillary, which is placed very close to the ion beam scanning area (less than 200μm from the sample surface) and points to the site of deposition. For example, $W(CO)_6$ and $C_9H_{16}Pt$ precursors can be used for tungsten and platinum deposition respectively [3]. The gas molecules are adsorbed onto the substrate and decompose at the region if hit by the ion beam. As a result, material builds up in the region scanned by the ion beam. A balance between sputtering and deposition is required in ion beam assisted chemical vapour deposition (CVD). If the probe current is too high, sputtering will occur rather than material deposition. In practice, both the ion beam and the electron beam can be used for deposition. Ion beam deposition will induce a thin amorphous layer (<15nm at 30keV ion energy), which can cause problems if the top surface of sample is of interest. Electron beam deposition does not have such a problem. However, electron beam deposition builds up much slower, so it is barely used in practice unless a perfectly undamaged interface between the coating layer and the sample is required. The gas injection system has also been used to pattern masks or films directly on substrates [4] or as a doping tool to fabricate quantum effect devices [2]. Halogen-based gases are used to enhance the sputtering yield of the Ga^+ ion beam. Gas molecules interact with the sputtered atoms (non-volatile species) to form volatile halogenides that evaporate. This action reduces local re-deposition at the sputtering site, so that it improves the sputtering yield and provides better milling results.

2.1.2. Source of ions

The FIB uses a hairpin emitter liquid metal ion source (LMIS) [5] as originally designed by Wagner and Hall [6]. Molten Ga metal (melting temperature 30°C) is placed in a reservoir coil at the end of a tungsten needle pointing downwards, as figure 2-3 shows. Ga wets the sharp needle and flows down along the tungsten needle to the tip. An electrical field is applied between the aperture and the tip, so that the tip experiences a high electrical field. The small volume of electrically conductive liquid Ga at the tip is affected by both surface tension and electric field and forms a cone with concave sides and a rounded tip, the so-called Taylor cone [7]. When the electric field given by the extraction voltage, which is the difference between tip (V_{source}) and extractor (V_{extr}) voltage is above a certain threshold, emission will start. The most widespread ion source is the Ga liquid metal source. There are a number of reasons for that: (i) its low melting point helps avoid any inter diffusion between liquid Ga source and the tungsten needle, (ii) its low volatility at the melting point provides a long source life, (iii) its low vapour pressure allows Ga to be used in its pure form rather than an alloy, (iv) it has excellent mechanical, electrical and vacuum properties and (v) its emission characteristic enables high brightness with a small energy spread, which means the ion beam output from the ion source has the potential to produce a high imaging/machining resolution [8]. There is a concentric ring aperture under the tip. The aperture is fixed and designed to stop ions which do not have a vertical velocity straight into the ion optical column.

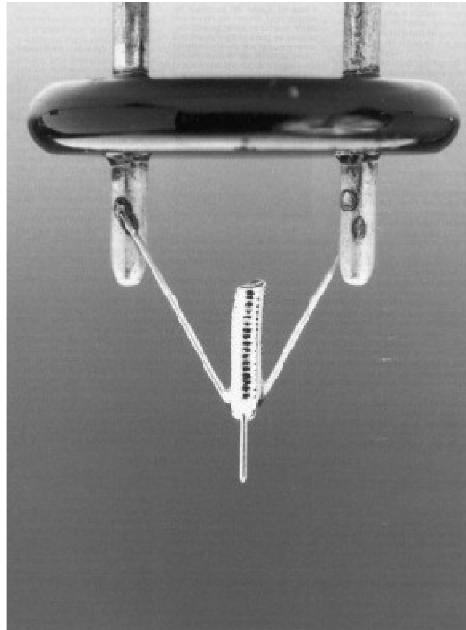

Figure 2-3 Ga liquid metal field ionization source and Taylor cone [8].

The FIB has two operation modes, high energy mode (standard mode) and low energy mode. The extraction electrode works differently for both modes. As mentioned above, the extraction voltage is typically set to a constant value to provide a constant electrical field which forms the Taylor cone at the tip of needle. An additionally applied suppressor voltage is automatically varying in a range of 0~2kV, to maintain a constant emission beam current (i.e. extraction current) of 1-3 μA. The emission current is set to a low value to provide a stable beam with low energy spread. At a high voltage of 30kV, a typical extraction voltage of 8kV as displayed in the software menu means another acceleration voltage of 22kV is applied at the electrode before the condensor. At lower energy of 5kV, an 8kV extraction voltage means a -3kV voltage will have to be applied at the source electrode, i.e. the polarity of the second electrode needs to be reversed.

When the suppressor voltage cannot keep the beam current constant or generate an ion beam of sufficient current any more, the source can be heated or a high (~15kV) but short period (~10 seconds) extraction voltage can be applied to re-activate the liquid Ga source. This heating process might lead to an unstable beam current for a short period of time (a few ours), but should stabilize thereafter.

Due to ions being much heavier than electrons, they can produce more secondary electrons from surfaces, which generates high signal-to-noise ratio secondary electron images. Compared with scanning electron microscopy, the ion microscope has a smaller virtual source size, significantly higher brightness, smaller intrinsic energy spread and smaller interaction volume within the sample analysed. In addition, the ion induced secondary electron (SE) imaging contains extra information about the crystal orientation by providing channelling contrast [9]. Thereby, the ion microscope has the ability to display material contrast. The FIB also sputters Rutherford backscattered ions (RBI), which can be used in mass-spectrum analysis and imaging of insulating samples [10, 11]. However, the damage induced by ion implantation is one of the disadvantages of FIB, which will be covered later. Some SEM images and FIB images will be compared and discussed in secondary electron detector section.

In recent years, gas field ion sources (GFIS) have been developed and applied to ion microscopy [12], which cause less radiation damage to the sample. The most typical gas sources are He and Ne. Due to the different fundamental mechanisms, the GFIS has a smaller probe size than Ga^+ LMIS and completely different damage type, which will be shown by simulations in section 2.2.1. The GFIS with its alternative damage type developed some new applications for FIB rather than traditional TEM sample preparation and semiconductor nano-machining [13].

2.1.3. Ga^+ Ion column design

The ion optic column is placed between the ion source and the sample chamber. It has multiple electromagnetic lenses for focusing and two-fold astigmation correction to help focus ions from the source into a tiny spot on the sample. The ion beam determines the FIB system's performance. The beam size varies from 100nm to 5nm in diameter, which also determines the resolution in secondary electron imaging when the ion beam is used for illumination. A typical ion column includes condenser lens, objective lens, **E**x**B** mass filter, beam blanker and aperture mechanism as shown in figure 2-4 [14].

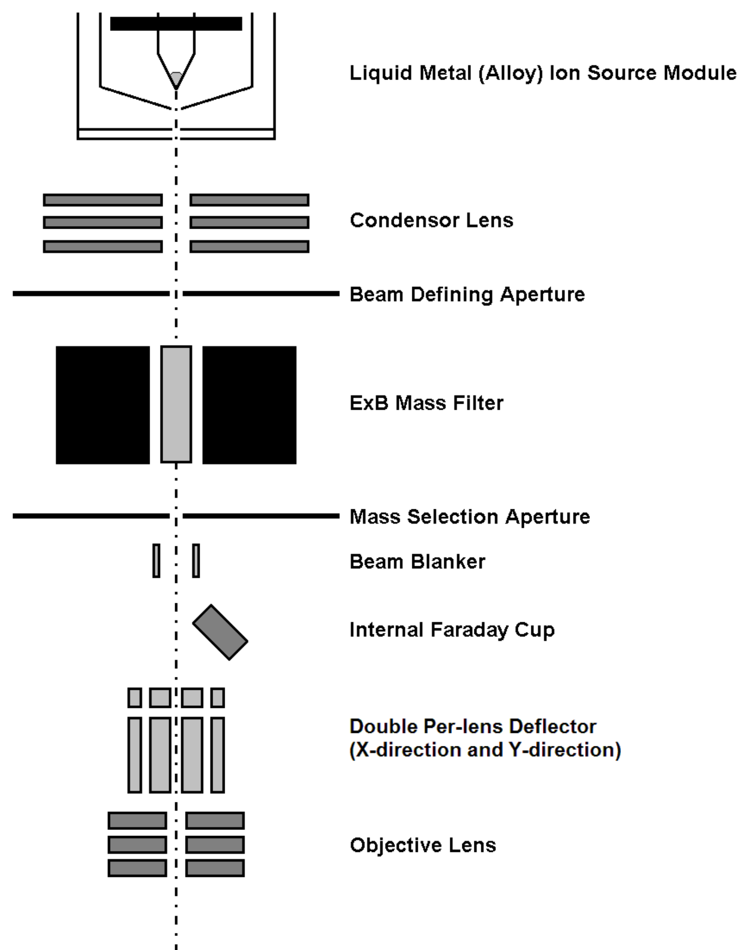

Figure 2-4 Ion optical column sketch of CANION 31Mplus [14].

The first electromagnetic lens, the condensor lens, is the probe forming lens, which is placed straight after the beam acceptance aperture. The second electromagnetic lens, the objective lens, is used to focus the ion beam at the sample surface, which is placed at the end of the

optic column. There is no cross-over of the beam from condensor lens to objective lens, which minimizes the beam broadening due to Coulomb interactions [15, 16].

The next parts below the condenser lens are a mechanical valve and an aperture belt mechanism. The valve can be closed to keep the ultra-high vacuum environment inside the ion source chamber when the sample chamber is vented due to sample loading or for any other reason. The aperture belt mechanism is a metal strip with multiple apertures of various diameters. The belt is driven by two motors to each saved aperture position when switching between different apertures. Mechanical fine alignment might be needed to ensure the beam perfectly passes through its centre on the optic axis. The aperture size defines the flux of ions entering the column, thus it controls the ion beam current intensity (in the range of 1pA to 20nA). Different probe currents are chosen for different tasks. A small aperture produces an ion beam with smaller probe size, which has the capability to generate high resolution secondary ion images and produce accurate milling/patterning. The small aperture produces a lower probe current, which significantly reduces ion beam damage to the sample by reducing the total ion dose to the sample. Combining with a large ion beam incident angle, the smaller aperture is also used for final polishing of TEM membranes to remove amorphous surfaces due to the ion-solid interaction. The larger apertures produce higher beam currents and faster ion milling with a large ion beam probe size.

Aperture Number	Aperture Size (μm)	Probe current (pA)
#1	10	1.5
#2	20	4
#3	50	40
#4	50	40
#5	100	200
#6	200	800
#7	400	2900

Table 2-1 The diameter of the condenser aperture and corresponding probe current. Data are measured from the FIB CANION 31Mplus column.

The mass separator designed for the FIB is primarily made to perform maskless implantation of semiconductors. As maskless n-type and p-type doping and lithography may require the implantation of other atoms alloy sources for n-type or p-type doping may be used. An **E***x***B** mass separator (Wien filter) is placed after the condenser lens, in order to ensure that the ion beam contains only one species of ions of constant energy (velocity). Ions entering the separator from the source have different axial velocities. This difference leads to different positions inside the electric field. This process results in different acceleration for every

particle. Particles travelling away from the central axis, which have different velocity vector, are filtered by the mass selecting aperture below, thus the ion chromaticity is improved.

The deflection of ions is achieved by a cylindrical octupole lens. Electronic signals applied to the octupole plate are accurately controlled to form a transverse electric field. The octupole lens has three major functions: beam deflection, alignment and stigmation correction. More detail about the stigmator alignment is provided later. It can also perform scan field rotation and shifting. A dc voltage added to the deflection signal is used to shift the scan view over small distances (<100μm) in the quadrupole direction (2-dimensions). Before the deflector, there is a beam blanker device. It can deflect the beam away from the centre of the column into a Faraday cup to quickly switch the beam on and off. The Faraday cup is also used for the output probe current measurement, which will be covered in chapter 3.1 in more detail. The signal for ion beam deflection can be sent from either the Orsay system or the Raith lithography software. The former is used for the ion beam alignment and tuning, the latter is better for milling and patterning. An ion beam pattern can be generated by sending pre-programmed correlated signals to the blanker and deflectors from the Raith software.

2.1.4. Secondary electron detector

When the electron beam is scanning the target, the electron-solid interaction generates different types of signals. Secondary and backscattered electrons, X-rays, cathodoluminescence and Auger electrons can be produced, as shown in figure 2-5. We are mainly talking about the electron beam in this section; ion beam implantation and ion-solid interaction are discussed in chapter 2.2 'Focused ion beam damage'. Of major interest in this chapter are secondary electrons (SE), which are collected by the secondary electron detector and form an image. For the SEM, secondary electrons are generated due to inelastic scattering by electrons in K-orbitals of specimen atoms. The SEs have a very shallow escape depth thus the secondary electron image only provides information on surface features. It also explains why the SE image is very sensitive to surface roughness. Backscattered electrons escape from deeper regions of the specimen with a projected range of 30~50nm. The escaping electron yield is measured as an average number of electrons produced per incident electron or ion (in general, <1). The yield of backscattered electrons is relatively low in contrast to secondary electrons.

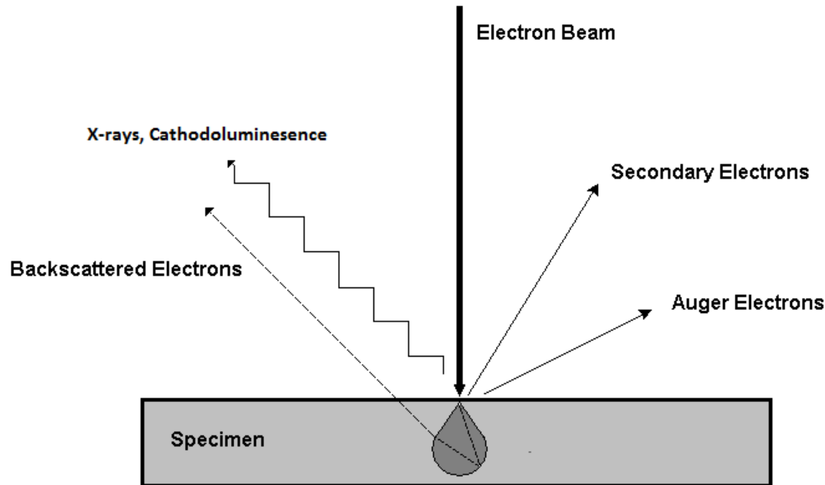

Figure 2-5 Electron-solid interaction and the escaping signals.

One type of secondary electron detector in SEM is called Everhart-Thornley detector. It uses a positively biased electrode to attract and collect the secondary electrons. The secondary electron signal is amplified and a signal-to-noise improvement is obtained by a scintillator-photomultiplier system as shown in figure 2-6. The collected SEs are converted into photons by a scintillator. Then the photons travel through a light pipe and hit a photocathode placed at the entrance of a photomultiplier tube (PMT). Inside the PMT, several dynodes are positioned as shown. They are positively biased to accelerate photoelectrons travelling towards them. When the photoelectrons hit the first dynode next to the photocathode, secondary electrons are generated and accelerated to the next dynode and knock out more secondary electrons. This process repeats inside the PMT multiple times, resulting in amplifying the electron signal at the anode at the end of the tube. A typical amplification from the combination of the scintillator and the photomultiplier tube is 10^8.

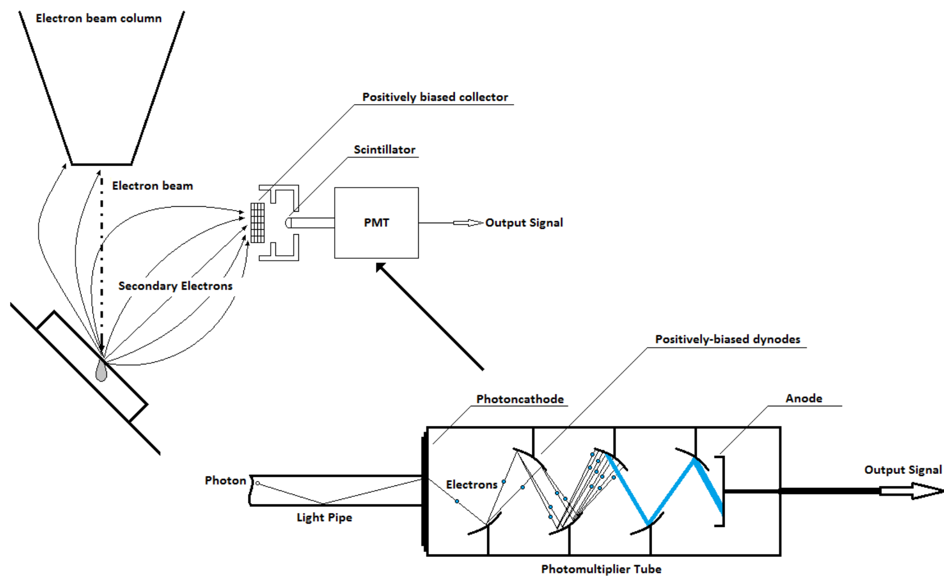

Figure 2-6 The secondary electron detector collects the SEs escaping from the interaction volume. The SE signal is amplified by the scintillator and the photomultiplier tube.

The secondary electron detector is usually placed beside the objective lens (out-of-lens detector), although in-lens detectors have better resolution. From a surface being tilted towards the detector, the escaping electrons are more likely to be collected and produce higher contrast in the image (brighter), and vice versa a surface tilted away from the detector has lower contrast (darker). This design helps the secondary electron imaging distinguish topography and atomic mass contrast as shown in figure 2-7. However, as a drawback, this off-axis position reduces the resolution. An electron beam size measurement has been done and will be discussed in chapter 3.

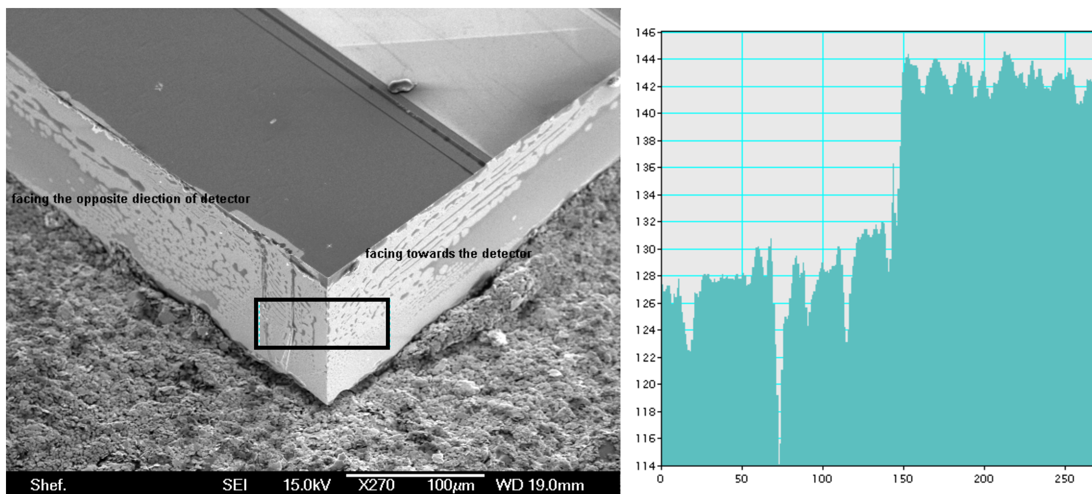

Figure 2-7 The surface facing towards the detector has higher intensity a the surface facing the opposite direction of the detector (left), as shown in the integrated line profile across the edge (right).

2.1.5. Beam alignment techniques

To optimize the performance of the FIB, an optic column alignment is needed, including centring each aperture, tuning the electromagnetic lens and fine tuning the beam using stigmators. There are two possible tuning techniques.

The first one is aligning the beam to the centre of the objective lens by adjusting the position of the aperture belt, in order to minimize the aberrations due to the lens, as shown in figure 2-8 below. To align the beam, the objective lens is alternatingly defocused and focused. The focal length change will move the focal plane up and down. If the beam is not at the optic centre of the lens, the image will have obvious lateral motion, as shown in the right part of figure 2-8. The position of the aperture is moved in order to eliminate image wobbling and centre the beam.

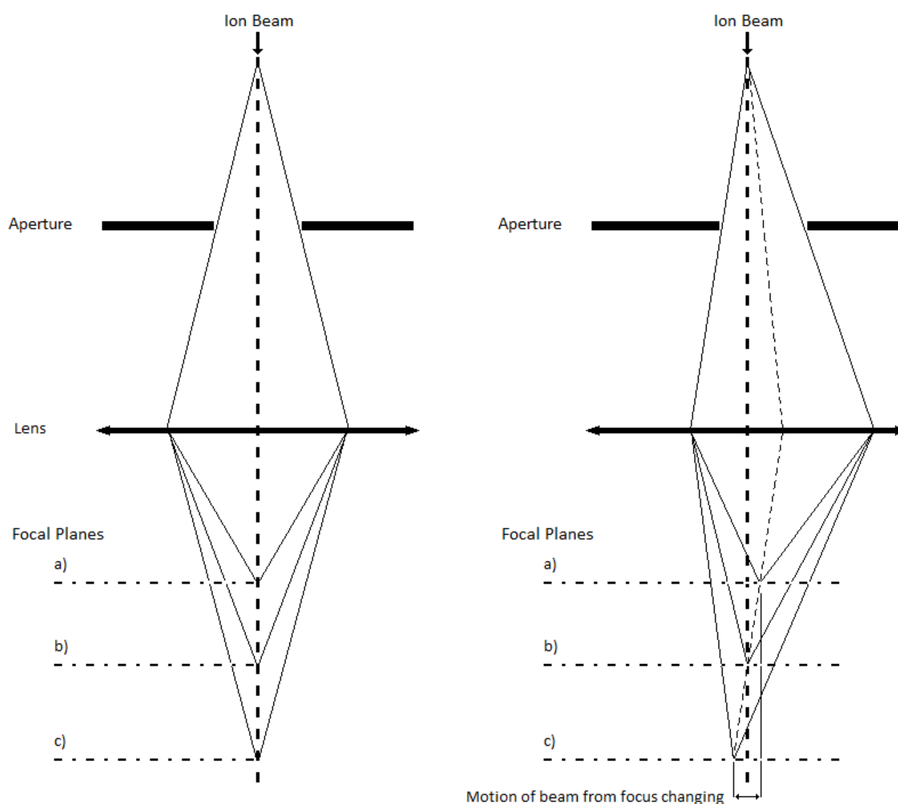

Figure 2-8 If the aperture is correctly aligned at centre position, changing the strength of the lens will only generate focal plane change but the image does not show lateral movement (left). If the aperture is off-axis, changing lens strength will generate both focal plane change and lateral image wobbling.

The second technique is aligning the beam to the centre of the stigmator and correcting the beam aberration by balancing the octupole. The octupole is separated into two four-plate-quadrupoles, controlled by stigmator knobs X and Y in the software interface. Each is modulated with a sine voltage. The sine wave has a dc voltage applied to them in a pair-wise manner as shown in figure 2-9.

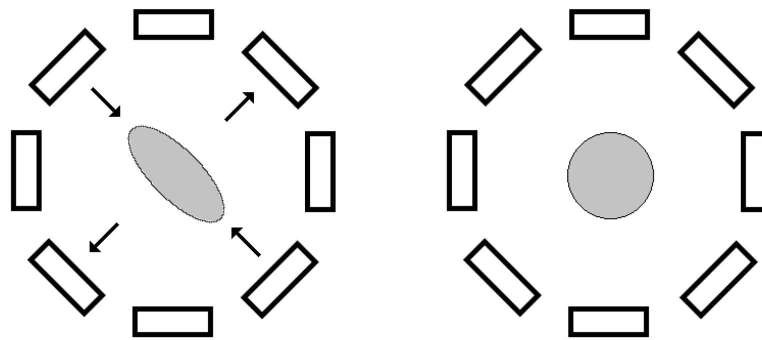

Figure 2-9 (Left) Misaligned beam, (right) a dc voltage is applied to one of the four-plate-quadrupoles in pair-wire manner to correct the aberration. This yields a well aligned beam, which is located at the centre of the stigmator without any two-fold astigmatism.

2.1.6. Micro manipulator

The micro manipulator is another essential tool for FIB instruments. In stand-by, the manipulator is parked close to the sample near the chamber wall, away from the central region. It will be inserted towards the cross-beam position when needed. There are stepper motors moving the manipulator in 3-dimensional space, at a precision of 10nm. When the manipulator is inserted, some FIB systems will lock the tilting and rotation functions to avoid any accidental collision between the sample/sample stage and the fragile tip. The probe tip is usually made of tungsten (Omniprobe system mounted on FEI Quanta3D), because tungsten has excellent hardness and tensile strength. Tungsten is also a good conductive material and therefore works well as an electrode in an electron microscope as it has no problems with respect to charging. Sometimes the tip may provide an electrical path between sample and ground. A brand new tip has a very sharp ending with a diameter less than 1µm. The tip will be milled and get blunt, which means it needs some sharpening by ion beam polishing. Typically, ion beam sharpening of a tip takes about 10 minutes with a relatively strong probe current (a few nA). A micro manipulator allows FIB systems to perform accurate mechanical operations at sub-micrometre scale.

The older JEOL/Orsay Physics dual beam system does not have a built-in micro manipulator, but a Kleindiek nanomanipulator has been retro-fitted subsequently, which was initially designed and built for nanowire electrical property measurement and nanowire micro-machining [17]. The manipulator is connected to an external micro-ammeter for electrical measurement [3, 18]. The manipulator controller has a digital display unit, which provides numerical information about the distance the probe has moved. Unfortunately, the relative direction of movement of the sample stage and probes and the probe movement range in the JEOL 6500F FIB-SEM are not very suitable for TEM sample lift-out.

2.2. Focused ion beam damage

After an introduction to the mechanism of FIB, in this part, more details about the interaction between the ion beam and the substrate are introduced (ion-solid interaction). The ion beam implantation simulator code SRIM (Stopping and Range of Ions in Matter) created by Ziegler et al. [19] has been frequently used to model and understand ion implantation. Ion beam damage can be separated into two categories. The first type is applicable to the standard FIB milling, focusing on how the sputtering yield is changing with several of parameters. The next part is focused on the damage induced by ion-solid interaction, which will be useful for nano-patterning experiments. The simulator TRIM is employed in both cases to set up models.

2.2.1. Ion beam milling and sputter yield

To explain FIB milling and sputtering, we need to understand the ion-solid interaction between the ions and the target. The incident ions are implanted into the target and can loose their kinetic energy in two major ways, nuclear energy losses and electronic energy losses. The nuclear energy losses are dominating the energy loss if the incident ions have energy higher than 5keV, as shown in figure 2-10, which is applicable to our case. The incident ions collide with the target atoms and cause atomic displacements. Because some energy is transferred to the target atoms, the initial collision can create a series of elastic collisions, a so-called collision cascade. The atoms located close to the surface are sputtered if they gain enough energy to overcome the surface bonding energy (SBE). The sputtering yield is the ratio of sputtered atoms to incident ions. This parameter is used to determine how fast the

target can be milled with a certain probe current, and it has a typical range of 1~20 for common Ga^+-semiconductor interactions at 30keV energy.

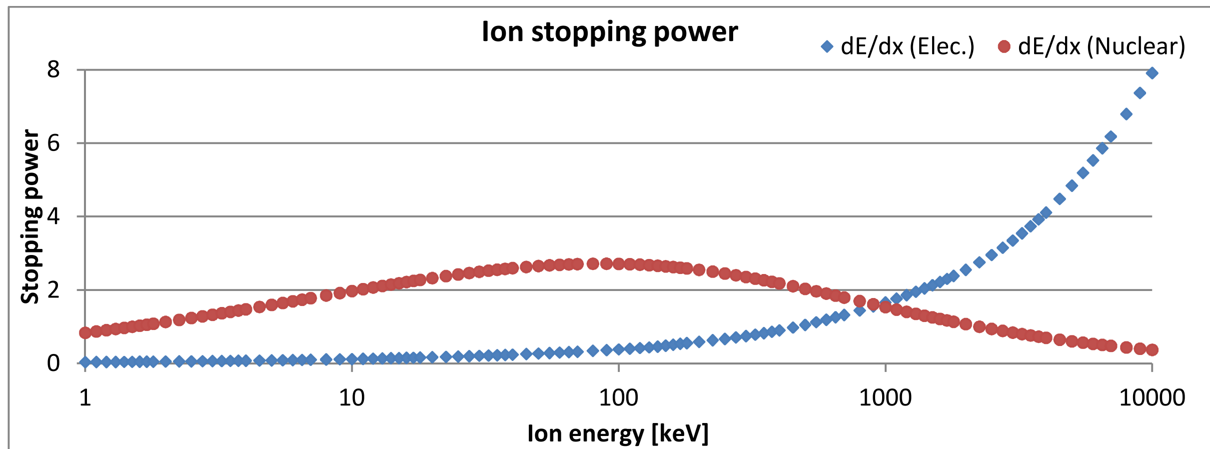

Figure 2-10 Plot of the Ga^+ stopping power vs. ion energy.

There are quite a few factors that can influence the ion-solid interaction and the sputtering yield, including the angle and the kinetic energy of incident ion (mass and velocity), the stopping power of the target material (the surface bonding energy and the atomic number), re-deposition etc. Obviously, it is a very complex phenomenon. To help with explaining the link between the sputtering yield and those correlated parameters, the simulator TRIM is used for Monte Carlo modelling of the ion-soild interaction. There are a few built-in assumptions in these calculations [19], such as

i) SRIM assumes all target materials are amorphous rather than crystallized, thus the simulation is based on estimating the average travel distance between each collision and the simulation ignores channelling and sample orientation;

ii) There is no atom sputtering from the target in the SRIM simulation, however, the sputtering yield is estimated;

iii) There is no re-deposition and no surface geometry changes involved in the simulation, which means the target surface stays always flat.

Figure 2-11 shows the SRIM software interface, consisting of result and simulation plot. It is a simulation for 500 Ga^+ ions implanted into a GaAs target with a 30kV accelerating voltage. The incident angle is 0°, perpendicular to the target surface. All above mentioned parameters (ion and target material, accelerating voltage and angle of incidence) are adjustable.

The collision plot at the centre is showing the recorded collisions and track of the each incident ion after modelling. The modelling is done in three dimensional spaces, which can even be presented in 3D. Some crucial numerical data about the interaction region are shown beside the central plot, including projected longitudinal range (R_p), the lateral range (R_t), straggling longitudinal range (ΔR_p) and straggling lateral range (ΔR_t). The straggling parameters contain the standard deviations of the former parameters. The SRIM simulation result includes the sputtering yield for each target atom, which is very useful for milling studies.

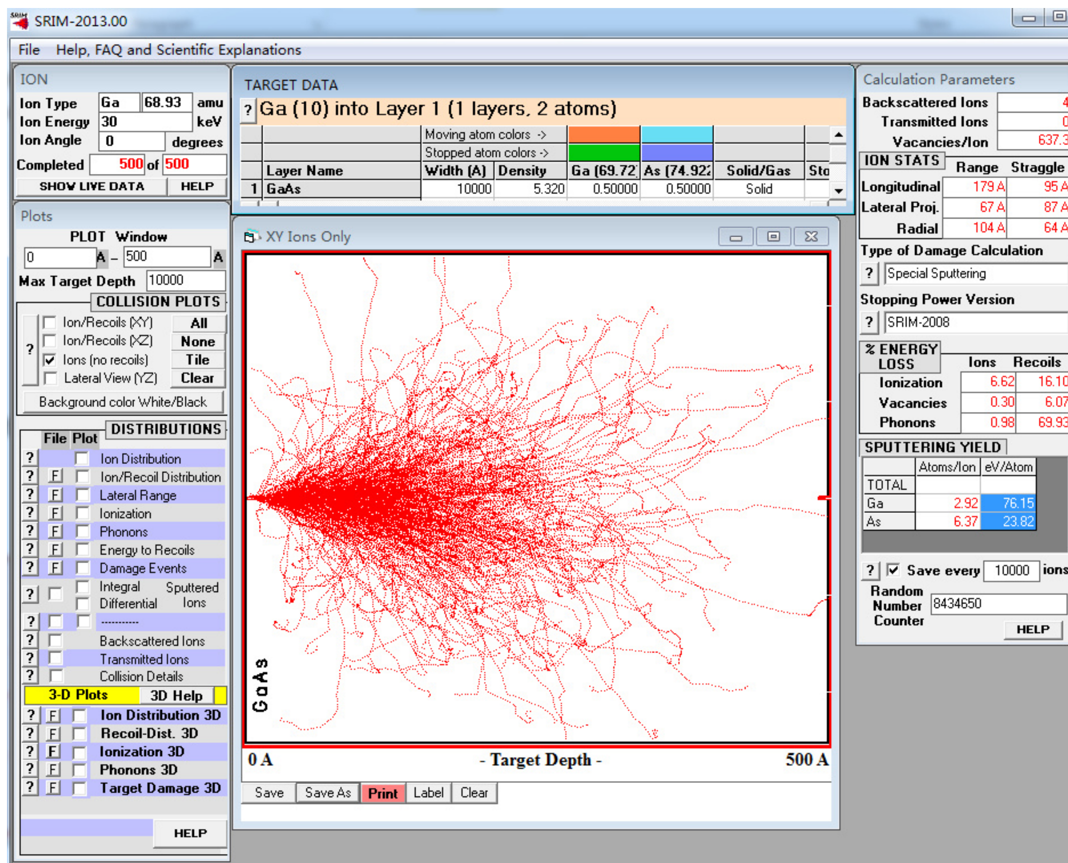

Figure 2-11 A screenshot of the SRIM simulation and result interface, which provides much useful information on simulation parameters and observables.

For general FIB machining and milling, we are interested in the sputtering yield and the size of the region of radiation damage. The sputtering yield is steadily increasing with the incident ion energy until ~5keV, and then it stays almost for increasing energy. In many situations, the ion beam is perpendicular to the target surface to minimize the radiation damage, even though changing the angle of incidence is the most effective way to increase the sputtering yield as shown in figure 2-12. We may ignore the influence from the mass difference between

the two colliding particles if the target consists of GaAs. Variation in the atomic number and the surface bonding energy produce significantly different sputtering yields as shown in figure 2-13. The melting temperature is a direct indicator of the bond strength, thus the sputtering yield has an approximately inverse correlation with the melting temperature as shown in figure 2-14. Those two materials properties have clear similar connection when comparing figure 2-13 and figure 2-14, which is due to the so-called stopping power of the material [20]. The period is correlated to the very well-known group periodicity in the periodic table of the chemical elements.

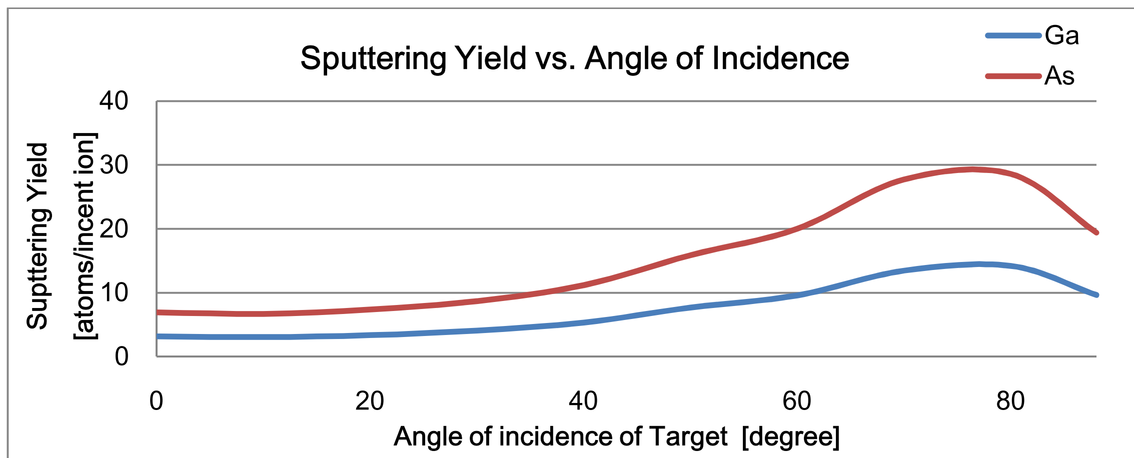

Figure 2-12 Plot of sputtering yield against angle of incidence. The sputtering yield has a maximum value in the range of 70° to 80°.

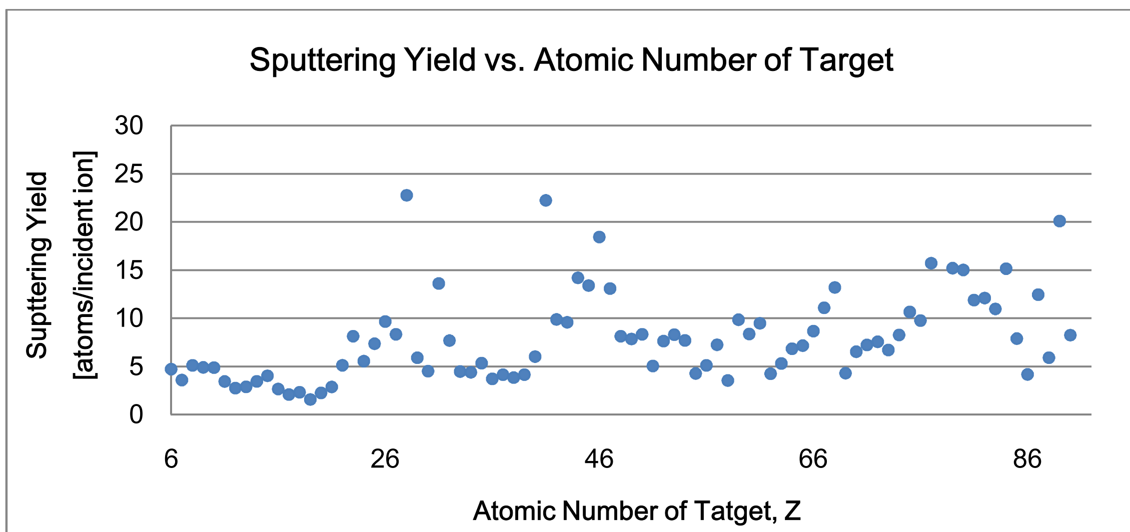

Figure 2-13 Plot of sputtering yield against atomic number. The simulation uses Ga^+ as incident ion at 30keV with an incident angle of 0°. [20]

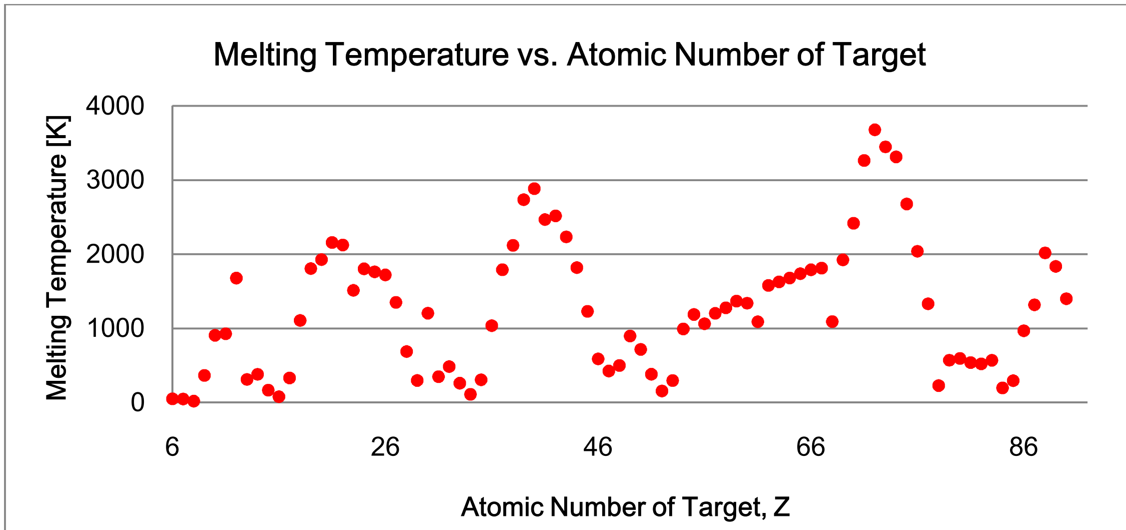

Figure 2-14 Plot of melting temperature against atomic number [21].

How the damage occurs inside the target will be covered in the next part. The radiation damage will be investigated with a focus on nano-patterning rather than standard FIB milling.

As mentioned in section 2.1.2, two types of gas ion sources, He^+ and Ne^+, are compared to Ga^+ implantation into a GaAs substrate at 30keV energy with an incident angle of 0°. The simulation results are shown in figure 2-15. The lighter ions have a deeper and wider range, as most of the collisions happen deep inside the target rather than near the surface, lighter ions will have a lower sputtering yield.

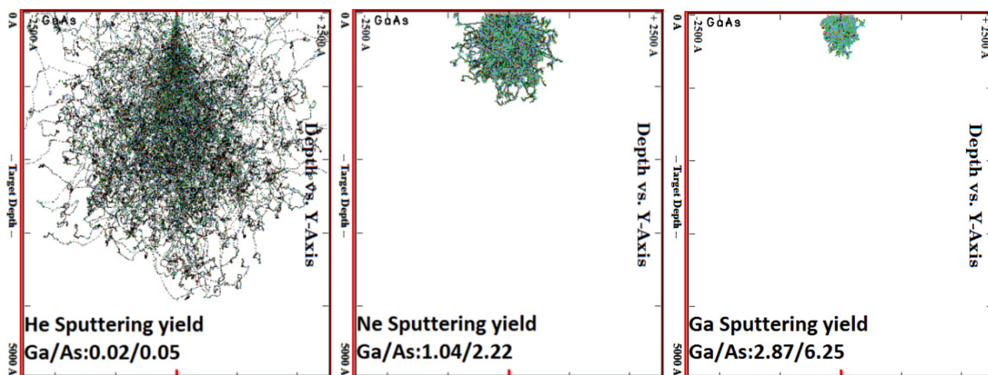

Figure 2-15 Simulations of He^+, Ne^+ and Ga^+ implanted into GaAs from left to right. The accelerating voltage is 30kV and 500 trajectories are simulated. The projected ranges of lighter ions are clearly larger. Lighter ions travel further, thus they have a lower sputtering yield.

2.2.2. Nano-patterning surfaces

When FIB is used as a patterning tool, it works differently from the standard FIB milling function [22]. For the ion beam patterning, we focus on producing ion beam damage at the surface of the target rather than sputtering out a large amount of material from the target. The primary ions can change the crystal structure and thereby also the surface bonding energy, making nucleation of islands in the Stranski-Krastanow growth mode more likely at the patterned sites than in non-patterned regions.

The damage from ion beam implantation depends upon acceleration voltage, ion beam probe current, ion dose and angle of incidence. The structure of the target itself also has some significant influence, which is not covered in this report, as we are focusing on (001) GaAs substrates only in this project. The simulator SRIM has again been used to simulate Ga^+ beam implantation into GaAs at different accelerating voltages (10kV, 20kV and 30kV), as shown in figure 2-16. The angle of incidence is 0°, which means the ion beam is perpendicular to the substrate surface. Each simulation involved 10,000 of trajectories. The coloured region represents the ions' travel and collision tracks inside the GaAs substrate and therefore defines the extent of the damage region. The simulation indicates a higher accelerating voltage will produce a larger damage region, with a larger projected lateral range (R_t) and deeper projected longitudinal range (R_p).

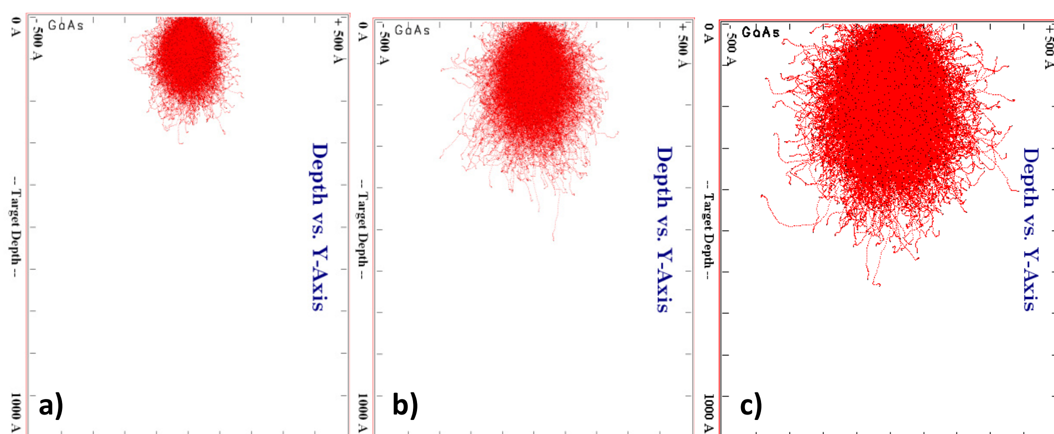

Figure 2-16 The SRIM simulation of Ga^+ implantation into GaAs substrate at different ion energies of 10keV (a), 20keV (b) and 30keV (c).

Another module of the SRIM simulator, ISRT (Ion Stopping and Range Tables) can simulate a simplified ion-solid interaction, but only provides data about the ion range, which is exactly what we need. The simulation result shows the relationship between the projected ion range and the ion energy from 10keV to 30keV, listed in table 2-2. These data are useful for annealing and overgrowth of the ion beam patterned substrate, because they allow us to estimate how much surface layer can be removed during the annealing while still retaining the regions patterned by the ion beam.

Ion Energy [keV]	Projected Range [nm]	Longitudinal Range [nm]	Lateral Range [nm]
10	8.0	5.1	3.6
11	8.5	5.3	3.9
12	9.0	5.6	4.1
13	9.5	5.9	4.2
14	10.0	6.2	4.4
15	10.5	6.4	4.6
16	11.0	6.7	4.8
17	11.5	6.9	5.0
18	12.0	7.2	5.2
20	12.9	7.6	5.5
22	14.0	8.2	5.9
25	15.2	8.8	6.4
27	16.3	9.4	6.8
30	17.4	9.9	7.2

Table 2-2 Ion energy vs. damaged area for vertical Ga^+ implantation into GaAs.

Because the simulator does not show any information about sputtering, the following work is based on practical experimental work. Depending on probe current and dwell time (two key factors the product of which is the ion dose), there are three types of damage that can occur at impact and influence the local structure by changing the crystal structure and surface bonding energy. We have used a Ga^+ beam with different parameters to pattern (001) GaAs substrates. For each scan (single pixel), the beam is stopped at regular positions to produce a regular array of features (holes), as shown in figure 2-17. From left to right, the ion dose increases. If the ion dose is low, the implanted ions sputter almost no atoms from the substrate, because the total number of atoms sputtered is proportional to ion dose (low) and sputtering yield (fixed). The implanted ions will create atom displacements and lower the local density of the target underneath the surface, creating a hillock at the damaged region, as shown in figure 2-17a. A later annealing procedure may flatten the surface completely, but the influence from

implanted Ga^+ still exists due to changes of the crystallography and/or the creation of dislocations by ion beam damage. After slightly increasing the ion dose, the ion beam will cause significant damage to the exposed region, creating a damaged amorphous region and a shallow hole. The damaged region will be partially repaired upon annealing, but cannot be completely eliminated. The rough surface influences later overgrowth significantly, as sketched in figure 2-17b. When the ion beam has high ion dose (>10^7ions/site), the impact will sputter out much more material and create a large and deep pit (diameter>30nm, depth>50nm) at the beam location. The pit remains almost the same after annealing and affects the overgrowth in different ways as the surface is not flat any more, as shown in figure 2-17c.

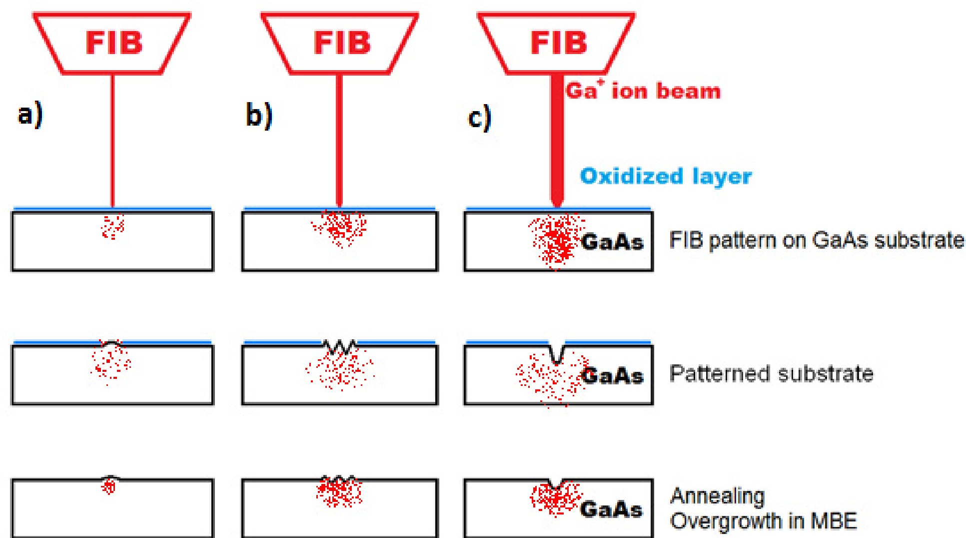

Figure 2-17 GaAs substrate patterned with Ga^+ ion beams with voltage and/or dose increasing from (a) to (c).

2.3. Molecular beam epitaxy

For the growth of InGaAs/GaAs quantum dots, molecular beam epitaxy (MBE) is used in this project. It can produce high quality epitaxial structures in an ultra-high vacuum (UHV) environment with very precise growth control. MBE has been the most widely used technique for producing epitaxial layers and has been well involved in both research and industrial production.

The principle of MBE growth is very straightforward. There are multiple cells generating atoms or clusters of atoms by heating up solid sources. The atoms or clusters of atoms diffuse into the high vacuum chamber and deposit onto the hot substrate surface, on which they can diffuse and incorporate into the growing material. The MBE growth has a low growth rate, small wafer size and low wafer capacity, compared with Liquid Phase Epitaxy (LPE) or Metalorganic Chemical Vapour Phase Deposition (MOCVD). But MBE growth is the best choice for this project, where a low growth rate and low temperature are required. The reacting atoms/molecules are injected from the solid source cells into the growth chamber as beams rather than completely filling the growth chamber, which provides better controllability of the growth. The UHV environment allows the use of electron diffraction to monitor the growth procedure by observing the reflection high-energy electron diffraction (RHEED) pattern. In addition, the UHV environment and high purity of semiconductor sources offer a very high material purity. Key parameters that need attention during growth include the temperature of the substrate and gas flux of the sources, which determines the growth speed.

To maintain a perfect high vacuum system, we need a stainless-steel chamber which can resist bake-out temperatures of 200°C for a long time. The pumping system must be able to consistently pump out the residual impurities to a minimum which is done by having a unity sticking coefficient. In practical operation, the base pressure is reduced to 10^{-11}~10^{-12} Torr. Effusion cell is a key component of an MBE system to provide a stable and uniform flux with very high purity. Multiple cells are placed on a source flange, all facing and focusing on the heated substrate, to provide a uniform flux, which is highly controllable but independent from other cells [23]. The temperature control system must be reproducible to the order of ±1°C. There should be no thermal transport between cells. The design of the cell must provide a uniform flux, regardless of the amount of material remaining in the tank. Each effusion cell has a shutter at the end of the cell, to ensure the molecular beam can be instantly switched on and off. At the centre of the growth chamber, the substrate is glued or clamped on a sample holder, which is mounted on a substrate manipulator. The manipulator can perform continuous azimuthal rotation (CAR) around its centre axis, in order to produce uniform growth condition at the centre region of the wafer. Another major function of the manipulator is heating, to provide a uniform temperature control across the whole wafer and a minimized impurity outgassing.

A very useful tool within a typical MBE system is RHEED [24], which plays a very important role in this project, as only a very thin layer of InGaAs is needed for the patterned wafers. An electron beam is shooting at the substrate surface at a very shallow angle (a few degrees) and a diffraction pattern is projected on a fluorescent screen on the side opposite of the electron beam gun. The electron beam will only penetrate the first few atomic layers of the substrate surface. The generated diffraction pattern provides live information about the top grown layers on the surface. If the surface is perfectly flat and has an ordered structure, the diffraction pattern on the fluorescent screen should be a series of streaks with modulated intensity. If the electron beam hits a rough surface with a lot of atomic steps, electrons scatter into different directions and the diffraction pattern constitutes of spotty features, rather than streaks. The RHEED diffraction pattern from an amorphous surface is a ring on a diffuse background. This diffuse background is used to evaluate if the surface oxide is completely removed during the annealing stage prior to over-growth. The diffraction pattern can dynamically provide information about the surface reconstruction.

2.4. Strained-layer epitaxy of InGaAs/GaAs (001)

Stranski-Krastanow (SK) growth is a quantum dot growth technique based on strained layer epitaxy, where the film grown has a larger lattice constant than the substrate (GaAs 0.565nm and InAs 0.606nm). The SK growth begins with a few monolayers of a planar wetting planner layer. Then islands start to form by cluster nucleation. The SK growth is driven by the strained surface energy from lattice mismatch (7%). In a strained surface layer, the formation of islands produce a greater surface area at the top of the island (reduce strain energy). But the stain is increases that the side of the island. However, as the top has more volume than the sides, the overall effect from the formation of islands is reducing strain energy, as shown in figure 2-18. At large enough deposition, the island configuration is always favoured if there is compressive lattice mismatch.

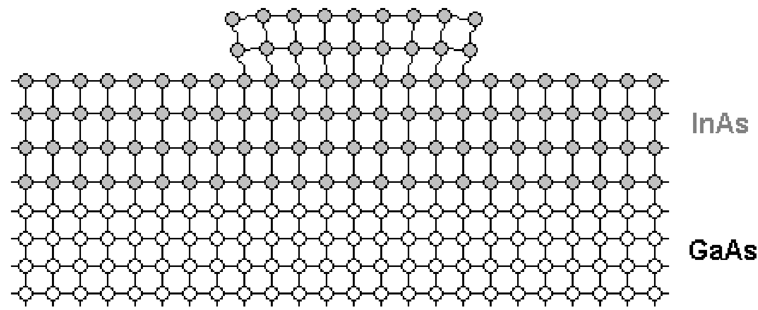

Figure 2-18 InAs and GaAs have a lattice mismatch of 7%. The formation of islands helps with releasing some of the strained surface energy.

InAs and GaAs have a lattice mismatch of 7% and the threshold wetting layer thickness is ~1.8ML [25], which means the two-dimensional growth is transferring to three-dimensional island growth if more than 1.8ML of InAs are grown. The islands will start to coalesce when the InAs thickness exceeds 2.3ML, thus the size of islands will increase and the island density will drop. A typical growth temperature of InAs is between 470°C and 650°C, with a growth rate of ~0.1ML/s. The temperature influences the diameter of the nucleated islands and the island density. As temperature increases from 470°C to 560°C, the diameter increases from 15nm to 45nm and the density decreases [26]. Further temperature increase will result in the size of QDs increasing. A typical InAs QD has a shape of a dome or pyramid with a base of 20nm and a height of a few nm. The growth conditions in this project have been varied from wafer to wafer.

Chapter 3. FIB characterisation and milling of lamellae samples

This FIB study involves a few sub-projects, covering a wide range of methodological studies and applications. They are an ion beam and electron beam probe size measurement (resolution), some standard TEM cross-section lamellae lift-out and the manufacturing of two special apertures for (S)TEM. The main project is the production of regular arrays of quantum dots grown on FIB patterned GaAs substrates, described in the next chapter.

3.1. Probe current measurement

In the Orsay FIB control panel, the probe current can be measured by blanking the ion beam into a Faraday cup, which has been mentioned in section (2.1.3). The measured result could be slightly lower than the actual value due to some backscattered electrons leaving the Faraday cup and the ion beam spreading. The probe current is controlled by the ion beam emission current and the size of the beam defining aperture. In most cases, the ion beam emission current is a constant value coming out from the ion source, which is stabilized and tuned by the suppressor voltage, as described in the 'source of ion' section (2.1.2). An unstable ion source can cause the ion beam being out of focus or misaligned [5]. The probe current is controlled by switching between the different beam defining apertures of different sizes. The range of the accessible probe current is from 1.5pA to 2900pA as shown in table 3-1. The increases of a factor ~2000 clearly points out how critical it is to wisely choose an appropriate probe current for specific applications. The most frequently used probe current is 40pA, which is provided by two apertures (#3 & #4); heavy usage will enlarge the diameter of the aperture with time by sputtering.

Aperture Number	Aperture Size (μm)	Probe current (pA)
#1	10	1.5
#2	20	4
#3	50	40
#4	50	40
#5	100	200
#6	200	800
#7	400	2900

Table 3-1 The aperture size and the resulting probe current with an ion energy of 30keV. Data are measured the FIB CANION 31Mplus column.

The stability of the probe current is an important parameter, because it significantly influences the ion dose and material sputtering speed. During the patterning stage, the ion dose is one of the most important parameters if we are trying to reproduce exactly the same patterns at different locations, especially with an identical ion dose. That is why the probe current is always checked before each step of nano-patterning. A stable probe current should not drift from day-to-day use, in most cases, the probe current is more likely to drop rather than increase and source heating can bring it back [5]. But the heating process will reduce the source stability for a few hours.

3.2. Ion beam size measurement

In order to gain a better understanding of the SEM/FIB instrument and determine the optical column performance, ion beam and electron beam probe size measurements have been done. The actual machine resolution of the ion beam is always larger than the value of 2nm that stated in manufacture's manual [27]. The actual value will be useful for the nano-pattering experiments. The probe sizes in SEM and FIB images have been measured using different methods. Discussion and comparison of those methods are provided in the following section.

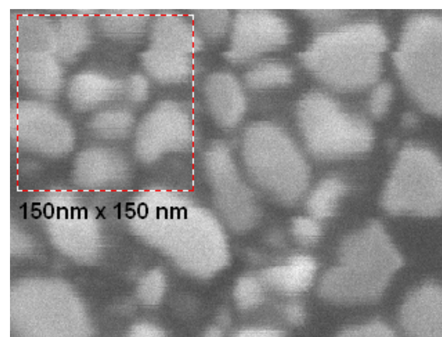

Figure 3-1 Secondary electron beam image captured with a magnification of ×300k with the SEM. The square box size is 150nm x 150nm

At first, a simple calibration specimen of gold particles on carbon from Agar (AGS168E) has been used. The gold particles have diameters from 5nm to 150nm and were randomly located on the carbon substrate, which provides high contrast images, as shown in figure 3-1. Usually, this specimen is used to calibrate the magnification of the scanning electron microscope by measuring the smallest dark space between two neighbouring features, which will be used and explained in more detail later.

Figure 3-2 is a high magnification secondary electron image captured using FIB illumination. The power spectrum of 512×512 pixels square region from figure 3-2 is shown in figure 3-3 (left).This modulus of FFT can be used for tuning and testing the optic column alignment. If the beam was well aligned and the specimen is completely amorphous or isotropic, the central bright spot would have a perfect round shape. The size of the bright spot is inversely proportional to the information transfer in the source image [28], which means a high resolution image would have a wide information transfer and a low resolution image would yield a well-defined spot. The right part of figure 3 is a line profile across the centre of the bright spot, which yields a 1D transfer function. The relationship between width of the peak and the resolution is shown in the equation (3.1) below. The resolution, d_{PS}, is the inverse of the width of the peak at 13% ($1/e^2$) of the maximum value. If the shape of the spot was not round, the line profile should be taken from the shorter radius, giving an underestimate of the actual resolution.

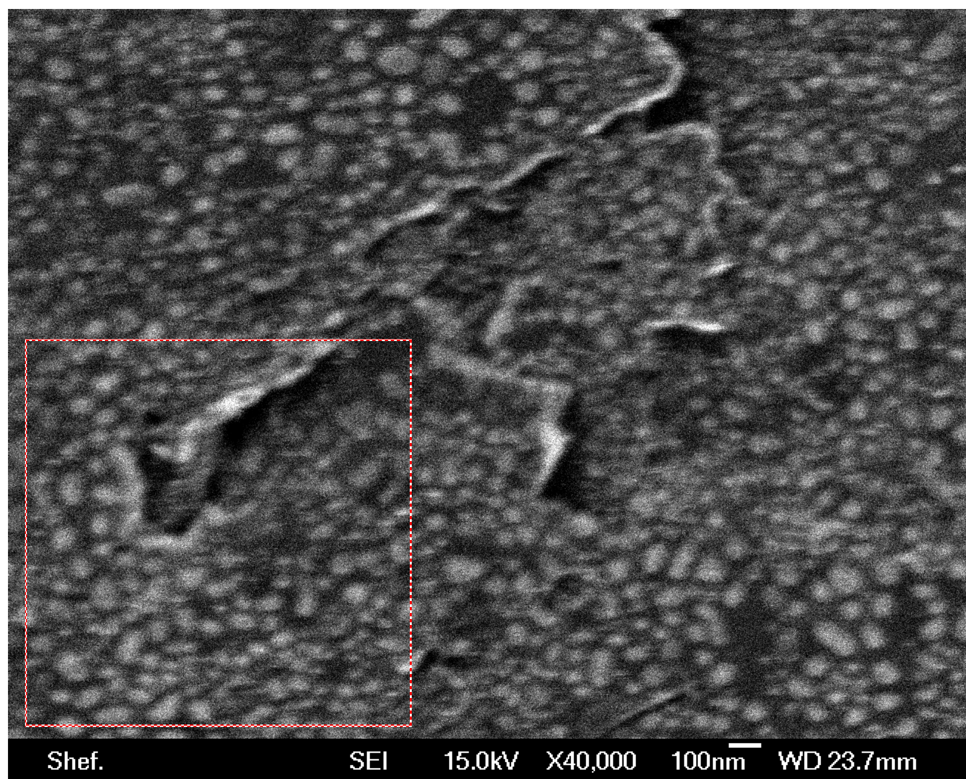

Figure 3-2 Secondary electron image FIB image captured of Au/C specimen with probe current 4.0pA and 30kV beam voltage.

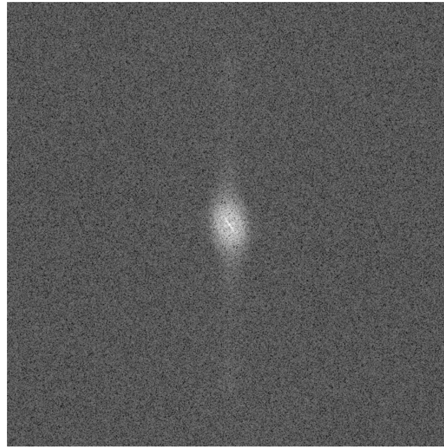

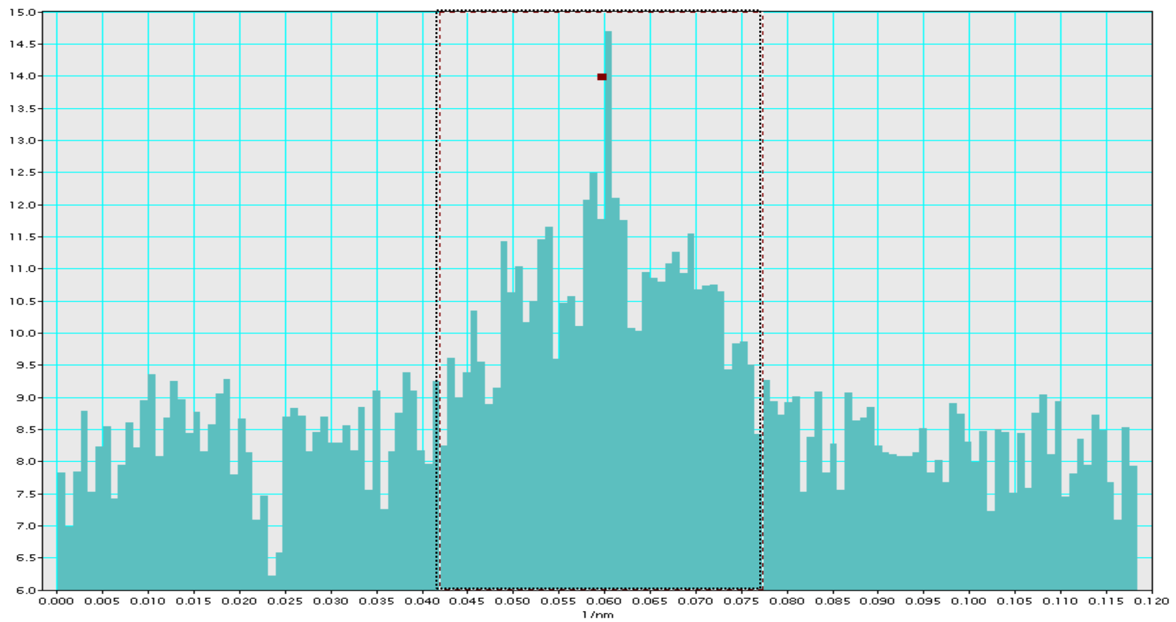

Figure 3-3 The power spectrum of the 512×512 pixel square region from the secondary electron FIB image in fig. 3-2 (top). The profile of 1D transfer function across the centre of the bright spot in vertical direction (bottom).

$$d_{PS} = {}^{1}/_{g_{13\%}} \tag{3.1}$$

An alternative way to measure the probe size by using this calibration specimen is measuring the width of the smallest dark region between two neighbouring islands (in real space). This is the so-called dark-space resolution, d_{dark}, as shown in equation (3.2), describing the full width of half maximum (FWHM) of the dip, as shown in figure 3-4. This measurement is a quicker and easier approach.

$$d_{dark} = full\ width\ at\ half\ max\ of\ the\ smallest\ contrast\ gap \tag{3.2}$$

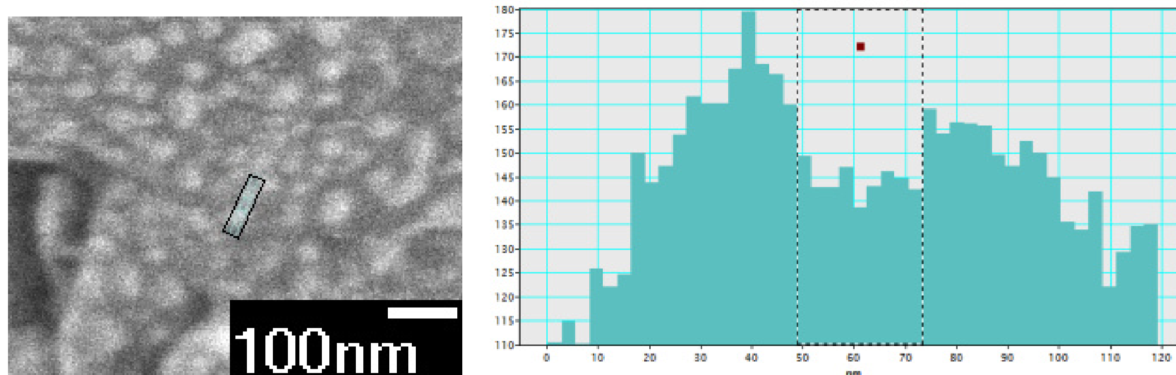

Figure 3-4 Line profile of contrast across two islands

Thirdly, a 200μm thickness GaAs wafer was cleaved, which produced an extremely sharp edge. The sharp edge was placed across a sample stub holder which had a 2mm diameter hole at the centre. An SE image of the atomically sharp GaAs edge is shown in figure 3-5. The left (dark) half, which has barely any secondary electrons, is empty space; the right (bright) half is the GaAs specimen. The image gives a strong contrast difference at the GaAs edge, as shown in figure 3-5a. The contrast change offers an alternative method to measure the probe size. We integrate the line profile of the edge over 512 pixels wide as shown in figure 3-5b.

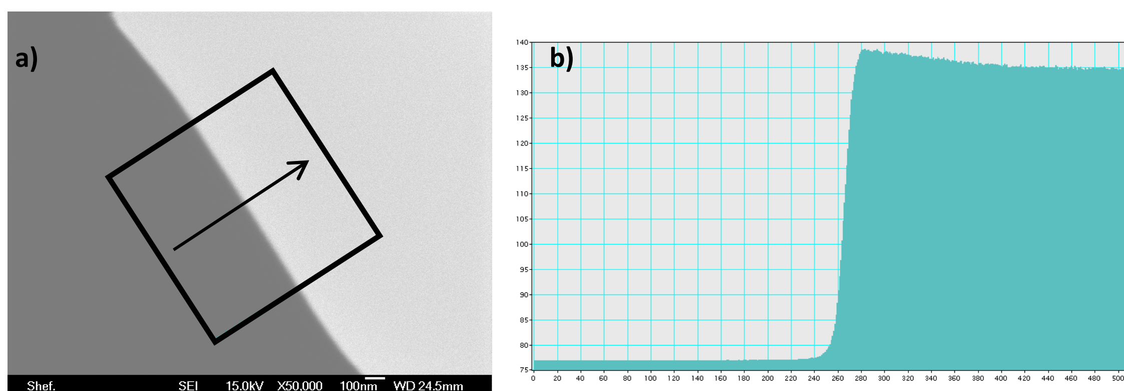

Figure 3-5 Secondary electron SEM image of a sharp GaAs edge (a). The contrast line profile of the boxed region (b) shows a clear and strong contrast difference at the edge.

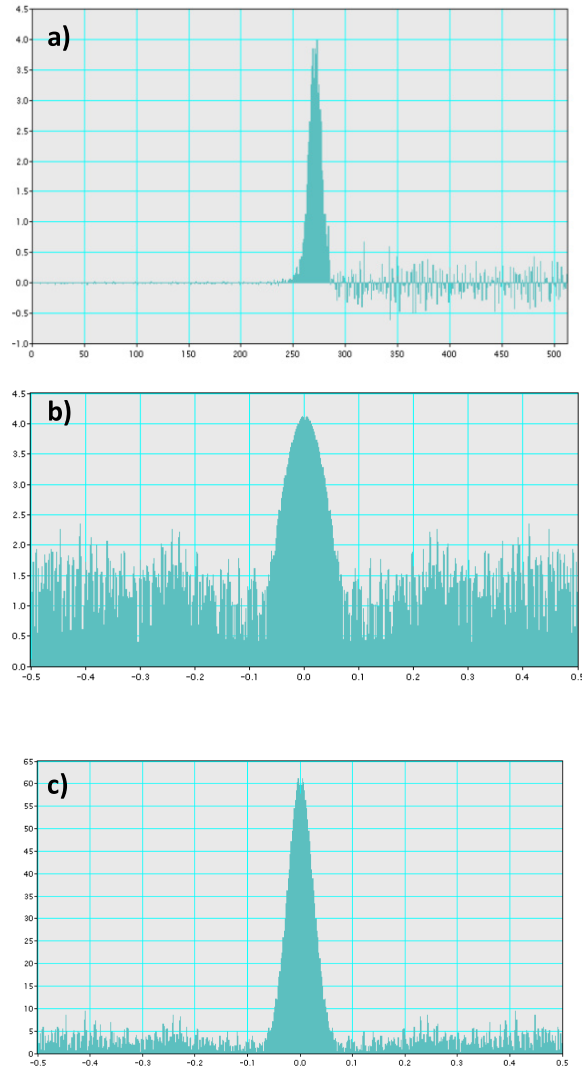

Figure 3-6 Differentiation of the line profile in figure 5 (a), the result of FFT from the line profile (b) and the 1D section of modulation transfer function (c). All images are using pixel scale on x-axis.

By differentiating the line profile, we obtain the line spread function, shown as figure 3-6a.When FFT (figure 3-6b) and modulus calculation are applied to this function, this results in a 1D section of the modulation transfer function, as shown figure 3-6b. The relationship between width of peak and resolution is shown in equation (3.3) below. Resolution, d_{LSF}, is the inverse of the width of the MTF at 13% of peak value, in order to avoid the background noise, similar to d_{PS} before.

$$d_{LSF} = {}^{1}/_{g_{MTF13\%}} \tag{3.3}$$

Due to our SEM not having an in-lens secondary electron detector, if the edge is facing the detector, more secondary electrons from the vertical side wall of the edge are captured. These

extra secondary electrons generate a blurred edge image, producing a wider peak in the differentiation of the line profile. By comparing two images in figure 3-7, the image in figure 3-7a, which was acquired facing the detector, has a blurred edge and a worse resolution measurement result compared to figure 3-7b, which shows the image facing in the opposite direction, away from the detector. A plot describing the relationship between the obtained resolution and edge direction is shown in figure 3-8. When the edge has an orientation about 330°, almost parallel to the direction facing the detector, the apparent resolution was worse.

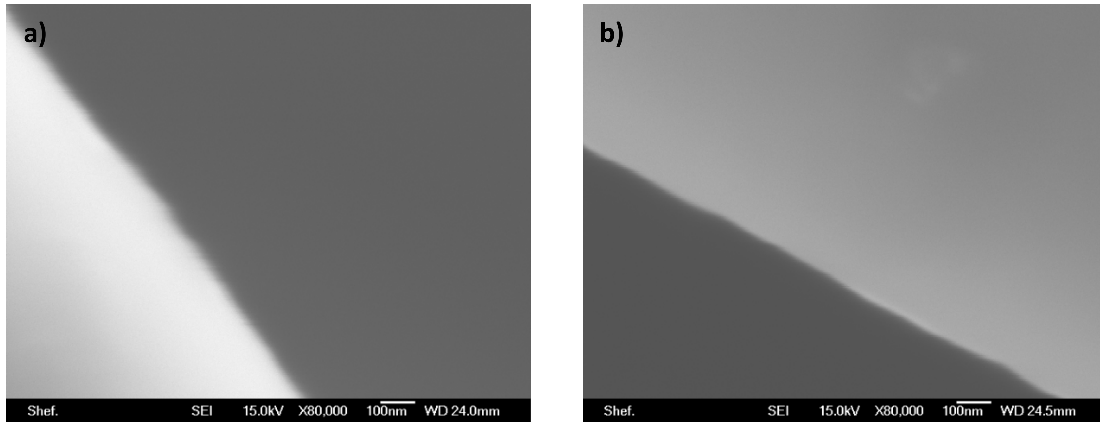

Figure 3-7 (a) Secondary electron image FIB image captured of the edge of a cleaved GAAs wafer with an orientation of 330 degree facing the detector and (b) the edge with an orientation of 150 degree facing away from the detector. Under an identical imaging environment and beam alignment, the former image has a blur in contrast to the latter image.

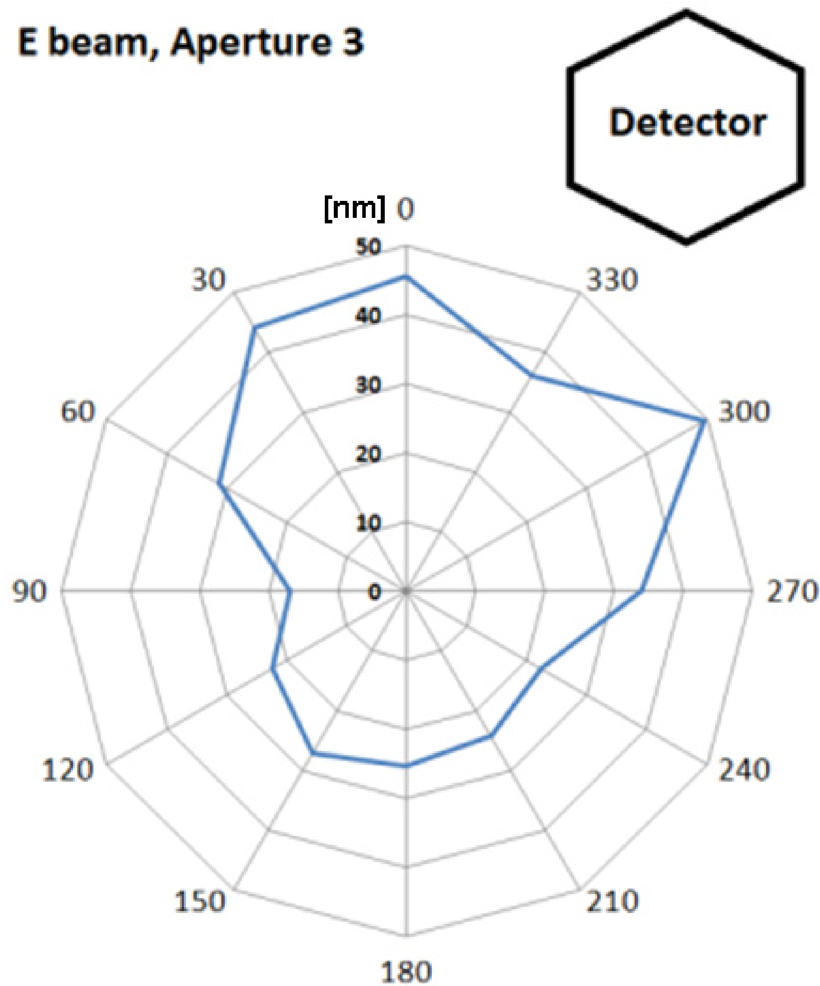

Figure 3-8 Resolution measured by edge method as function of edge orientation relative to the secondary electron detector. Measurement is made at 15keV energy with a probe current of 100pA.

In summary, all three methods produce rather different numerical values for resolution of SEM and FIB, as shown in the table below. Each method has its own problem.

- The power spectrum measurement does not yield highest possible resolution at 13% ($1/e^2$) level. Because the signal to noise ratio will be higher at high probe current, while noise will be worse at lower probe current, this problem is more obvious with SEM rather than FIB. Because the ion beam has a higher secondary electron yield.
- The dark space visibility measurement is subjective, as a result of manual operation and also noise sensitive. However, it often produces the best (lowest) result, which is also the reason it is the method favoured by the manufactures. This method works perfect with SEM but does not work well with FIB, due to the ion beam milling the surface micro-structures during the measurement, which significantly reduce the reproducibility.

- Determining the line spread function from a wafer edge does not yield an isotropic result, due to the off-centre SE detector position in our instrument. The secondary electrons escaping from the side wall of the edge will affect the result of the measurement.

Aperture	Aperture Size (µm)	Probe Current (pA)	d_{PS} (nm)	d_{dark} (nm)	d_{LSF} (nm)
FIB-#1	10	1.7	31	22	42
FIB-#3	50	40	51	27	49
FIB-#5	100	170	93	35	68
SEM-#1	110	n/a	20	7	43
SEM-#2	70	n/a	28	17	73
SEM-#3	50	n/a	14	5	30
SEM=15kV (JEOL 6500F)					
FIB=30kV (CANION 31 MPlus)					

Table 3-2 Resolution measurement results

In conclusion, these measurements obtain some useful information about ion beam size, which will be used later in the project. Under identical experimental conditions, we get

$$d_{LSF} > d_{PS} > d_{dark}$$

In e-beam resolution measurement, it is obvious that, d_{PS} is much larger than d_{dark}. The SEM result was close to the manufacturers value (2nm, measured at 5cm working distance with 5kV accelerating voltage). For ion beam, d_{PS} is still larger than d_{dark}, but they are closer. The FIB result was not as good as expected. The reason for that is that the ion beam scan was always damaging/milling the sample during imaging, especially when the magnification was high. This behaviour crucially affected the resolution measurement. Considering the gold-on-carbon calibration sample, scanning the ion beam milled some particles away and enlarged the dark space between neighbouring islands, which reduced the apparent resolution. Some small features could possibly completely be eliminated. The ion beam also smooths sharp edges, which means the slope of the contrast line profile across the edge is reduced, resulting

in an apparently worse resolution d_{LSF}. This inherent issue was getting worse when the ion beam current was increased, as shown in table 3-2. However, the measurements agree better for the ion beam than for the electron beam when probe current is low. Despite a weaker ion beam knocking out fewer secondary electrons, the ion beam still produces far more secondary electrons than the electron beam due to the ion mass. The ion beam imaging results in a better image quality with a higher signal-to-noise ratio.

3.2. TEM/STEM cross-sectional sample preparation by FIB

A site-specific TEM sample is an ultra-thin (10nm-200nm) micrometres-sized membrane from a specific location of a larger sample or substrate. Often, the region of interest (ROI) is buried a few hundred nanometres below the top surface. FIB's characteristic feature, sub-micrometre precision milling and powerful micro-machining functions make it an excellent tool for this application [29]. TEM cross-sectional sample preparation and lift-out has become one of the most mature FIB applications. In-situ lift-out has replaced ex-situ lift-out. There are a few advantages of in-situ lift-out. (i) The in-situ lift-out sample is attached to a special carrier rather than placed on carbon or formvar film which could obstruct the TEM investigation. (ii) The in-situ lift-out sample can be further Ar ion polished to remove the disordered surface layer due to Ga implantation. (iii) The in-situ lift-out sample has higher success rate thanks to digital control system and safer working environment, in contrast to ex-situ lift-out.

3.2.1. Standard experimental work procedure

A standard FIB lift-out technique includes the following steps; milling trenches, thinning the lamella partially separating the sample from substrate, lifting out the sample from substrate, attaching lift-out sample to special carrier grid and thinning/polishing the membrane.

The process starts from sample stage localization, to find the ROI with secondary electron imaging. The ROI should then be covered with a protection layer. This layer is made from W, Pt or C, deposited by FIB assisted deposition. A typical size of the protective layer is 2µm x

15μm and 1.5μm thick (fig. 3-9a). Then two deep trenches will be cut by high probe current FIB milling until a 'wall' is left standing inside the groove (fig. 3-9b). The 'wall' is thinned down to 1~2μm thickness. The ROI located under the protection layer should be revealed at this moment. The side and bottom connections are cut, leaving only a narrow bridge to hold the membrane standing still (fig. 3-9c). The micromanipulator is slowly approached and carefully bonded to the membrane by FIB assisted deposition. After that, the membrane is completely separated, cut free from the substrate and lifted out with the micromanipulator (fig. 3-9d). Finally, the membrane is mounted on a C-shaped copper support grid (fig. 3-9e). Gently polishing under a small ion incidence angle will be performed till the sample reaches the required thickness (fig 3-9f). During the final polishing, the membrane is slightly tilted, in order to get a parallel side wall on both side of the sample. The angle is between 0.5° and 3.0°, depending on the probe current and the thickness. Otherwise, the resulting membrane will have a broader wedge shape at the base [30]. This whole process can take a few hours, depending on material hardness, sample size and if there are any specific requirements. A series of images captured during the FIB TEM lift-out practical work is shown in figure 3-10. The only difference is that we made a few windows with different thicknesses rather than steps of different thicknesses [31, 32].

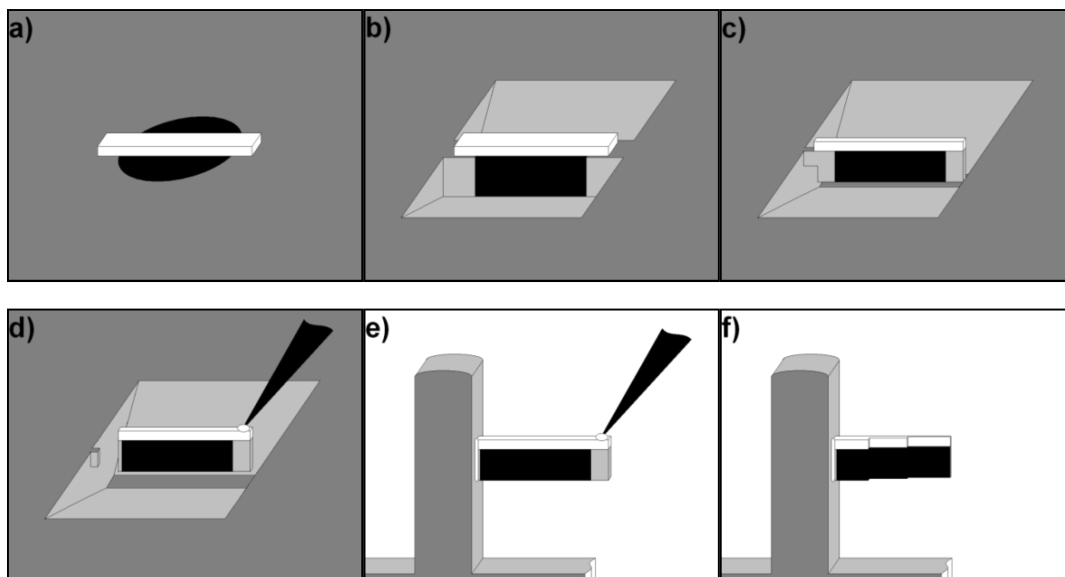

Figure 3-9 Series of schematic diagrams shows the procedure for the FIB TEM lift-out sample preparation.

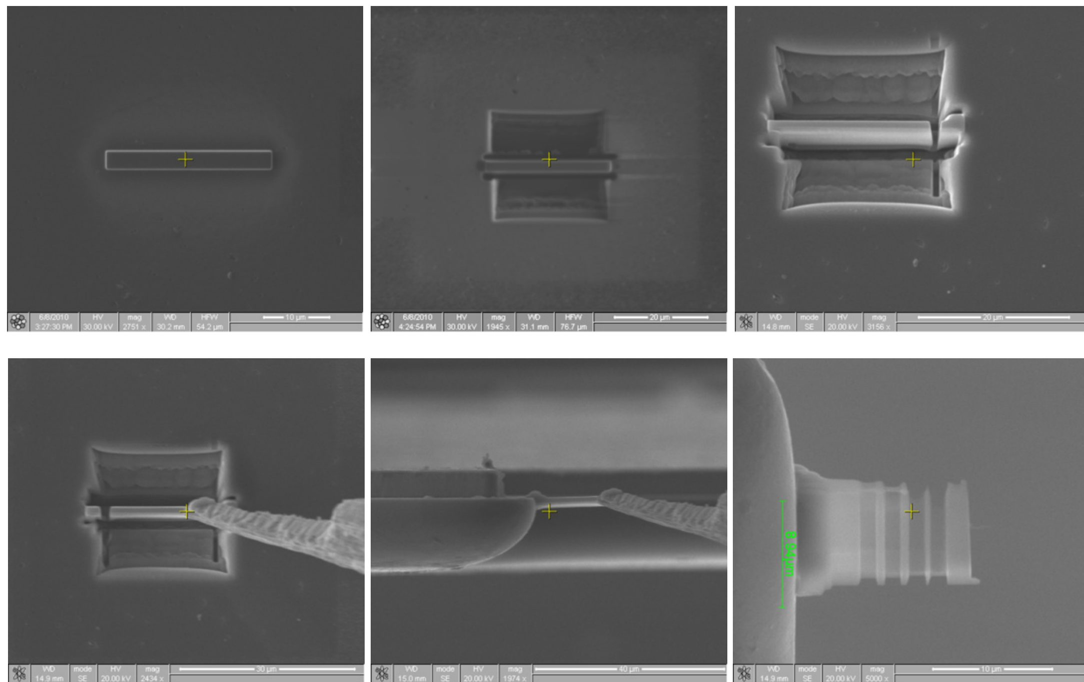

Figure 3-10 Series of images captured during the FIB TEM lift-out practical experimental work. The procedure is as the same as shown in figure 3-9. The size of the trench is 15μm long.

3.2.2. Possible problems and solutions

During TEM sample preparation, there are typical problems in practical experiments that could make the sample preparation very difficult or even destroy the sample. We will analyse the reason and the corresponding solutions to those problems.

➢ **'Waterfall' or curtaining effect**

This effect is due to the fact that the material sputter ratio varies with the angle of incidence, the hardness and the surface geometry of the target sample. This difference is most pronounced when the ion beam first contacts the sample. The milling speed difference may result in a 'waterfall' or 'theatre curtain'-like rough surface of a cross-sectioned sample. A non-uniform thickness of a TEM membrane sample makes precise calibration difficult and produces contrast where the sample is homogenous in chemical composition. This effect can be avoided by depositing a homogeneous coating, ensure the ion beam initial encounter with the target is uniform and the final sample lift-out comes from regions below the protective coating. Another option is to reduce the ion beam current and increase the movement speed.

- **Electrostatic charging**

The sample is subjected to a high energy ion bombardment under the FIB operation and there are several thousand coulombs of charge accumulated at the ROI or the entire specimen. The biggest problem from the built-up charge is ion beam image drifting. The ion beam can be micrometres offset from target location and destroy the features we want. The solution is to always build a path for discharge, which can be achieved by silver glue or coating the entire sample with good conducting material (C or Ag). However, we always try to avoid contamination, especially if the sample will be used for later X-ray or EELS analysis. Alternatively, scanning the electron beam simultaneously at the milling region can neutralize the positive ion charge and reduce the charging effect. This works only when the ion beam probe current is low (<40pA).

- **Ga contamination and amorphous layers**

It is impossible to cut a sample by Ga^+ FIB without Ga implantation, despite the near-grazing angle of incidence of the FIB ion beam [33]. Likewise, some ion milled material sputtered from one part of the specimen can contaminate another part of the specimen. The ion implantation also creates an amorphous layer at the scanned surface. Both re-deposited Ga and amorphous layers disorder the crystal structure, which contributes noise to the later TEM investigation. To remove or minimize those defects, a low energy, low probe current and low angle (88°-89.5°of ion incident angle) polishing is needed, gently scanning the membrane at the last stage. An ex-situ argon ion milling before putting the sample into the TEM will partially solve this problem, but it always sputters some Cu from the support grid.

- **Top surface sensitive samples**

During the first few seconds of depositing the protecting layer, before the ion beam and gas interact and form the protection layer, the top layer of the ROI is exposed to the ion beam. In most situations, the produced thin damaged layer is negligible, if the ROI cross-section is hundreds of nanometres below the surface. However, this can be a problem in surface-sensitive samples, such as free standing nanowires, very thin top coatings or MBE quantum dots without cap layer. These tiny features and ultra-thin layers are very sensitive to ion bombardment. Any exposure to the ion beam can lead to crucial damage to their structure or even completely wipe them off. One of the solutions is using e-beam assisted deposition

before the ion beam deposition. A thin e-beam deposition ensures the ion beam bombardment is not reaching the ROI at all. Although the speed and crystallographic structure of the electron beam deposition is not as good as the ion beam deposition, it still works well.

Chapter 4. Aperture micro-machining for TEM applications

We used the FIB to fabricate two aperture plates for our JEOL 2010F FEG-(S)TEM. The aperture plates have an outer diameter of 2mm and less than 100μm thickness. This size is fixed, because the finished aperture plate will be placed in the aperture stripe belt of the TEM. The aperture plate is made of an ultra-thin (8~10μm) metal foil glued to a 0.1mm thick brass support ring. We have two options for the metal foil, which are either gold or aluminium. Two types of apertures are fabricated. The first aperture has a ring shaped (annular) hole for (S)TEM annular bright-field (ABF) imaging which the microscope does not have originally. The ring shaped aperture will stop all electrons with a small enough scattering angle and those that travel near the optic axis, thus the aperture will produce ABF images. The diameter and position of aperture plate will define the diffraction angle. The other aperture has a more complicated coded pattern. The pattern programmed can, theoretically, boost TEM image quality. It is a much more complicated aperture in both the design and production stage compared to the ring aperture.

This project utilizes the excellent micro-machining capability and flexibility of the FIB. We have met and solved a few problems and challenges in this experimental work, which has been a very useful experience.

4.1. Ring shaped aperture fabrication

A 8~10μm thick metal foil was glued on a ~80μm thick brass ring with 2mm outside diameter and 1.5mm inside diameter. Two types of foils have been tested; gold foil and aluminium foil. The ring to be cut out was 5μm wide, with 40μm outer diameter and positioned at the centre of the foil, as shown in figure 4-1a and 4-1b. The FIB milling began with a high probe current (200pA) to first penetrate the foil, followed by a lower probe current polishing (40pA) to ensure the sidewalls were straight rather than inclined. We repeated this process on the aluminium foil later. The two materials had significant different milling ratios. The gold foil was milled about 3 times faster than the aluminium foil. The finished aperture was fixed into the selected area aperture drive belt mechanism of the TEM.

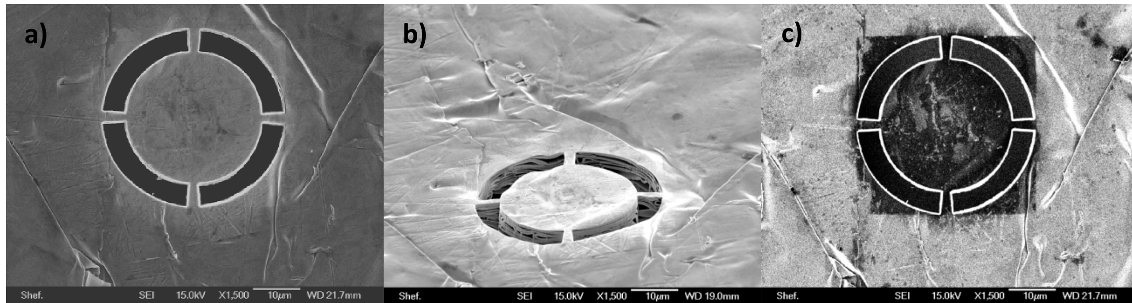

Figure 4-1 (a) A SEM secondary electron image of the ABF aperture fabricated from the gold foil. (b) A SEM secondary electron image of the fabricated aperture with a tilted angle to show the multi-layer structure of the gold foil. (c) FIB secondary image of the final aperture.

The aluminium ring shaped aperture was mounted on the aperture drive belt mechanism and produced annular bright-field images with a collection angle of 4~5mrad. A third-year undergraduate project student recorded ABF images, ADF images and BF images of a polymer sample of light elements. The sample consisted of groups of 20-40nm diameter particles on a carbon film. By comparing the contrast and the diameter of the particles, as expected, the ABF images had less noise than ADF images and more contrast than normal BF images due to the centre stop blocking some of the undeflected electrons.

As the result, the outcome of this ring shaped aperture has been acceptable. Ideally, the diameter of the ring should be bigger to produce images with a collection angle of 7-8mrad and another aperture twice as large was fabricated, to improve performance of the ABF imaging. This micro-machined TEM aperture has achieved the basic goal.

4.2. Coded aperture fabrication

I also fabricated a so-called coded aperture for diffractive imaging in a TEM. The idea is based on a modified uniformly redundant array (MURA). This is a special type of binary sequence defined by a two-valued binary periodic autocorrelation function. The aperture function can be represented as a 2-D binary matrix with values of 1 and 0 that describe whether it is transparent or opaque. It has a similar behaviour in imaging characteristics as uniformly redundant arrays (URA), which can be constructed from pseudo-noise sequences and can filter noise regardless of the original source structure [34, 35] after decoding the

formed image. The size of the pattern is flexible and the describing transmissivity of a MURA is approaching 50% when the number of total elements is increasing.

To physically construct such a coded aperture, we can use a fabrication technique similar as for the ring shaped aperture above: milling holes in the foil (1) yields areas of high transparency and leaving material intact to hold the structure defines areas that block transmission (0). Alternatively, depositing material on a nearly transparent thin foil could make it locally opaque (0) while the rest of the quasi-transparent foil would remain as transmissive (1). Gottesman and Fenimore [36] introduced how to make square configurations by using a concept developed by Calabro and Wolf [37]. The concept was initially developed to extend 1-D quadratic sequences to 2-D quadratic arrays. First, a binary aperture array is made according to a MURA sequence. The size of the pattern in real space is decided depending on the size of the apertures on a specific instrument, the number of elements (pixels) and the practical fabrication limitation. Then arrays are brought into symmetrical form by a cyclic permutation of the rows and columns that bring the top row and left column to the central position.

A MURA can be of any length $\underline{L}$, where $\underline{L}$ is a prime and of the form

$$L = 4m + 1, \qquad m = 1,2,3, \ldots$$

For example, the length $\underline{L}$ can be 5, 13 and 17, but not 9.

The binary sequence of length $\underline{L}$ is defined by

$$A = \{A_i\}_{i=0}^{L-1}$$

$$A_i = \begin{cases} 0, & \text{if } \underline{i} = 0, \\ 1, & \text{if } \underline{i} \text{ is a quadratic residue modulo } \underline{L}, \underline{i} \neq 0 \\ 0, & otherwise \end{cases}$$

An example in 1D would be given by:

$$m = 1, L = 5, A = \{01001\}$$

Transformation of a binary sequence $\underline{A}$ of length $\underline{L}$ to a binary array $\underline{A}$ of size $\underline{L}$x$\underline{L}$ is achieved by

$$A = \{A_{ij}\}_{ij=0}^{L-1}$$

$$A_{ij} = \begin{cases} 0, & \text{if } \underline{i} = 0, \\ 1, & if\ \underline{j} = 0, \underline{i} \neq 0, \\ 1, & if\ \mathrm{C_i C_j} = +1, \\ 0, & \text{otherwise} \end{cases}$$

where

$$C_i = \begin{cases} +1, & \text{if } \underline{i} \text{ is a quadratic residue modulo } \underline{L}, \\ -1, & \text{otherwise} \end{cases}$$

Continuing with the above example,

$$A = \{01001\} \rightarrow A = \begin{vmatrix} 0 & 0 & 0 & 0 & 0 \\ 1 & 1 & 0 & 0 & 1 \\ 1 & 0 & 1 & 1 & 0 \\ 1 & 0 & 1 & 1 & 0 \\ 1 & 1 & 0 & 0 & 1 \end{vmatrix}$$

Then transform the above matrix into a coded pattern array and combine multiple arrays into one aperture pattern, as show in figure 4-2a. By bringing the top row and left column to the central position, we obtain a coded pattern as shown in figure 4-2b.

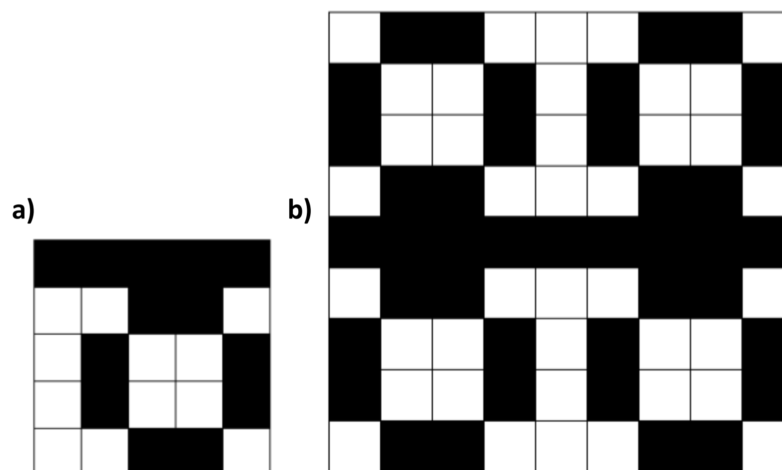

Figure 4-2 Transformation of a coded array (a) into an aperture pattern (b) by bringing the top row and left column to the central position.

The pattern fabricated in this study is a 21x21 pixel pattern, as shown in figure 4-3. The size of each pixel is 5µm x 5µm and the size of the whole pattern is 105µm x 105µm. This size fits the maximum field of the Raith pattering software and can be fabricated within a reasonable time. The white parts are empty (transparent) and black parts are remaining foil (opaque). In practical fabrication, the corners between pixels are reinforced as shown in figure 4-3b. The connections between pixels are modified into a bridge by reducing the size of each single pixel from 5µm x 5µm to 4.5µm x 4.5µm, which leaves 600~800nm wide bridges at the corner. The width must be as small as possible but also provide enough strength to avoid loss of material.

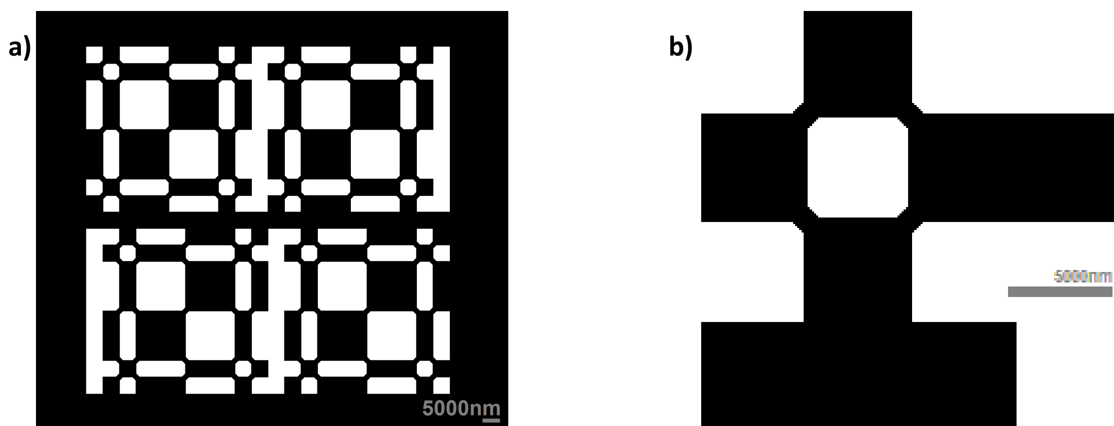

Figure 4-3 (a) The 21x21 pixel coded aperture. The white parts are empty (transparent) and the black parts are remaining foil (opaque). (b) The corners between pixels are modified for practical fabrication.

The size of the coded aperture is much larger than that of the previous ring aperture; therefore much more material needed to be removed, which mades fabrication very time-consuming. The initial plan was to produce this coded aperture from a gold foil because gold has a higher sputtering yield (17.36 Au atoms/ion from the SRIM simulation for 30kV Ga^+ ions), thus a faster milling speed. But the multi-layer foil structure started to collapse as shown in figure 4-4a. Then we switched to an aluminium foil. However, the hard and rough surface oxide (alumina) gave us some problems as shown in figure 4-4b. This image shows that the quality of milling was bad; also, the sputtering yield was low (1.91 Al atoms/ion and 3.97 O atoms/ion from the SRIM simulation).

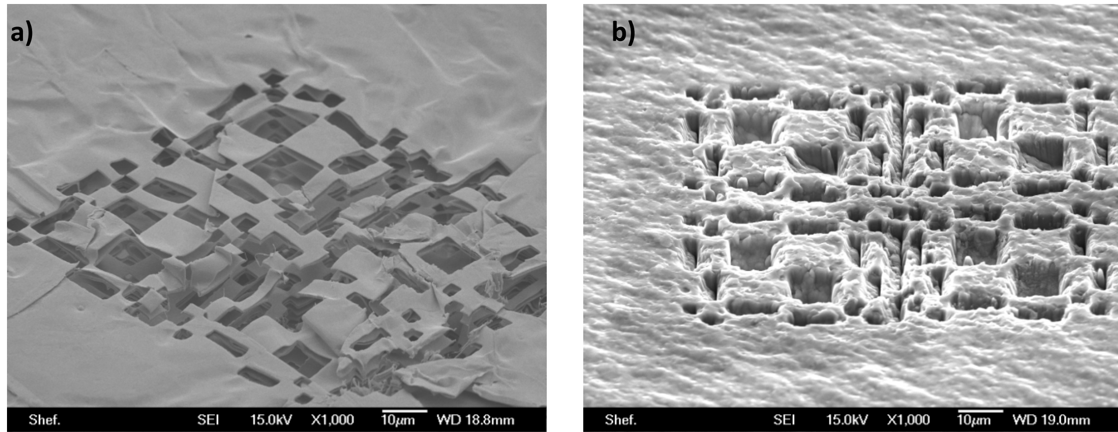

Figure 4-4 (a) The coded aperture fabricated from the gold foil collapsed. (b) Attempt to creat a coded pattern from a partially oxidized aluminum foil failed due to the high surface roughness and the high toughness of surface alumina. The image was captured after 12 hours of milling.

The solution was to gently polish off the top alumina by placing the foil on a standard TEM mechanical polishing stub. This treatment also reduced the thickness of the foil. It was difficult to measure the thickness of the foil precisely, so the foil was polished until only shallow scratches were visible under the optical microscope. However, the milling process still took ~35 hours with a probe current of 3nA, which is shown in figure 4-5 by secondary electron images captured every few hours. Comparing figure 4-4b and figure 4-5, the milling quality has been significantly improved, thanks to the polishing treatment. From figure 4-5d, the thickness of this foil is measured as 5.24μm. A few more SEM images were captured with a sticky carbon pad placed underneath the coded aperture to produce fewer secondary electrons at the transparent regions compared to figure 4-5. In addition, an image with high contrast was captured to show the other side of the fabricated aperture, to check if the aperture was really completely milled through. The structure has a few defects, but the result is acceptable as shown in figure 4-6. Because the pattern is centro-symmetric, the encircled image defects can help us recognise the orientation of the pattern. However, the defects may affect the result of the filter. The aperture should be placed in the TEM aperture belt mechanism. By decoding the captured images, the result should show a BF image with a reduced noise from source with respect to standard BF imaging. Unfortunately, due to the time limit, we have not had a chance to test this coded aperture. However, this fabrication project has provided a good opportunity to gain some valuable experience in FIB micro machining.

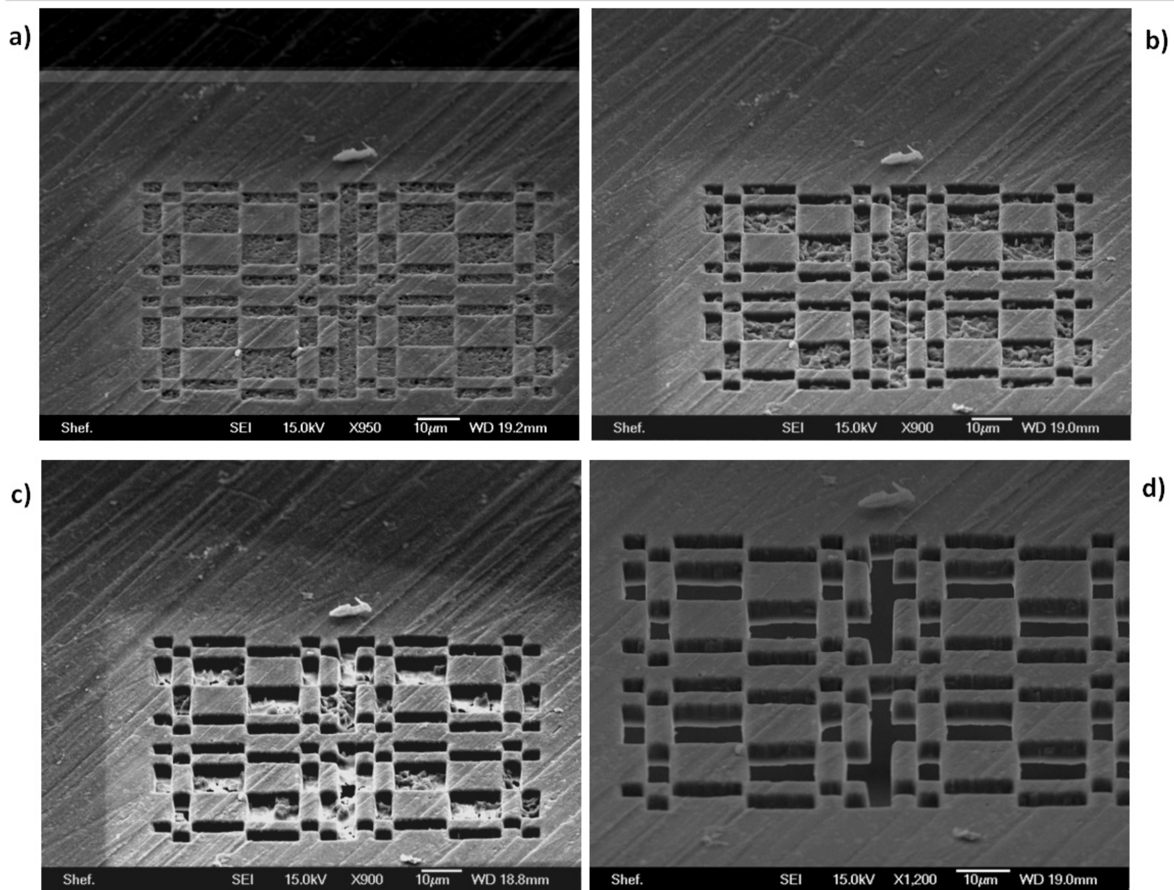

Figure 4-5 Four SEM secondary electron images captured during milling, after 4 hours (a), 7 hours (b), 21 hours (c) and 31 hours (d), respectively. The images are captured with a 55 degree tilted stage. The result clearly demonstrates that a flat surface results in a better milling quality and a higher sputtering yield compared to a rough surface, as shown in the previous figures.

We can estimate the probe shape of the focused ion beam by estimating the difference of the average size of the eight big open spaces at the surface and the bottom. Ideally, each open space should have a size of 13.5μm x 13.5μm (3 pixels at 4.5μm each) and the measured average size is 13.88μm in figure 4-6a and 13.16μm in figure 4-6b, which indicating <3% ion beam spread. By combining the difference from two ends and the thickness of the foil, we worked out the angle of the side wall is 4.3° from vertical axis. This information is very useful for the final polishing of TEM sample, which can be used as a guideline to determine how much the membrane should be tilted in order to produce two parallel walls on both side.

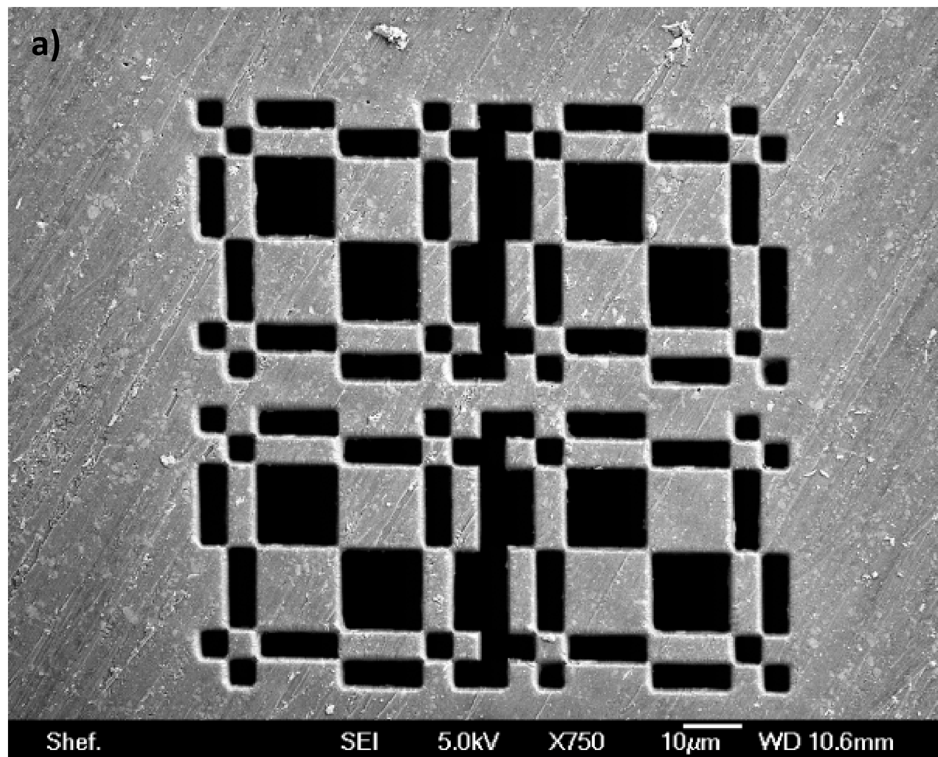

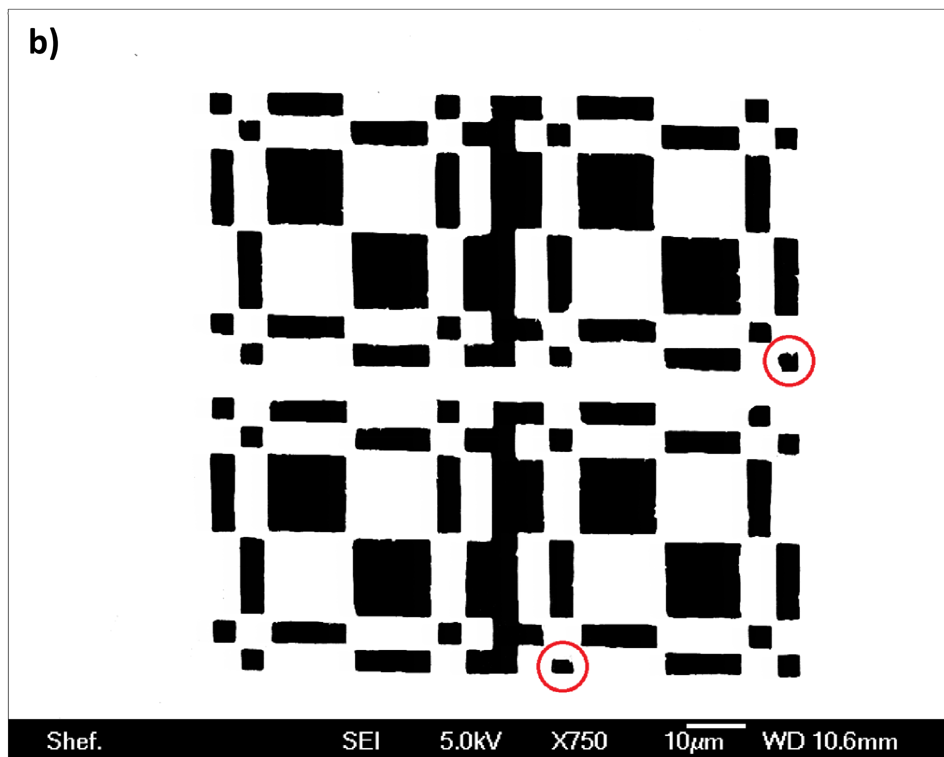

Figure 4-6 (a) SEM secondary electron images captured with a carbon sticky pad placed underneath the final aperture. The fabricated coded aperture has bridge connections between the pixels with a width of ~800nm. Image (b) shows the back side of the foil which is captured by increasing the brightness and contrast to a very high level. It shows the opening is slightly narrower than on the front side. It means the milled structures have a slope and the walls are not as straight as expected for vertical beam incidence. There are a few clear defects that can be used as indicators for the orientation of the pattern. They are marked by circles in image (b). Their extension is less than 500nm.

Chapter 5. Controlled quantum dot formation on FIB patterned (001) GaAs substrates

In this chapter, the study of InGaAs quantum dot growth over FIB patterned GaAs is presented. This is the main project during this PhD course. This chapter will begin with the motivation for fabricating QD arrays on patterned substrates. The advantage of regular QD arrays compared to self-assembled QD will be given. The following content is focused on the principle behind self-assembly of QD growth on patterned surfaces.

5.1. Motivation of fabricating QD arrays

In the last few decades, fabrication of quantum dots (QDs) has experienced rapid progress. Quantum dots are small artificially engineered crystal structures which have electronic properties that are characteristic of atomic dimensions [38]. The smaller the quantum dots are the larger their band-gap is. Quantum dots have been widely studied and are used in opto-electronic engineering for lasers, light-emitting diodes (LEDs) and solar cells. One of the dominating fabrication techniques is Stranski-Krastanov growth by molecular beam epitaxy (MBE). It is a top-down approach and a quick way to grow quantum dots on large areas of a wafer or substrate.

However, these self-assembled quantum dots have a certain spread in their size and hence of their emission energies [39]. Photoluminescence spectra of grown QD arrays can exhibit significant inhomogeneous broadening if their shapes, sizes or chemical composition differ laterally [40-42]. The inherently random position of nucleation in self-assembly puts limits on down-sizing devices further. If only a few quantum dots are included in a device, the location and uniformity of quantum dots will have a strong influence on the reproducibility of the electronic and opto-electronic performance across multiple devices. The bottom-up growth by patterning the substrate before overgrowth is an alternative approach which can produce regular QD arrays on patterned substrates with better position control and homogeneity [43]. Island-shaped quantum dots are expected to nucleate at specific locations where the ion beam has formerly patterned the surface. In order to reduce the strain energy of the wetting layer in the patterned holes, the deposited material has a larger thickness at the

patterned hole than on the terrace. The concave patterned hole therefore has a lower surface chemical potential and the deposited atoms always travel from the region with the high chemical potential to region with the low chemical potential [44]. This phenomena cause the wetting layer in the patterned sites being thicker, thus reaching the threshold thickness of SK transition earlier than the flat surface. By reducing the amount of deposited material to less than standard threshold thickness, QDs will only nucleate at the patterned region but nowhere else.

5.2. Localized QD growth on patterned substrates

It is a challenge to produce highly ordered QD arrays. Much research has been done in this area. There are quite a few techniques to make patterns on substrates. We combined FIB patterning and self-assembly of epitaxial quantum dots to grow InGaAs quantum dot arrays on (100) GaAs substrate in this project. Previous studies on this topic have confirmed this approach works well and regular QD arrays have improved optical properties [45, 46]. As mentioned before, different ion beam patterning parameters make different patterns, which has significant influence on QDs grown over them. We investigated how the patterning parameters influence nucleation and overgrowth, including the diameter, height and distribution of different forms of structures formed. We also tried to estimate the chemical composition by EDX and AFM image analyses.

Bottom-up QD growth can be achieved by using optical, electron-beam or ion beam based lithography [40, 46, 47], nano-imprint techniques [48] or growth on cleaved edges or misoriented surfaces [49]. Focused ion beam (FIB) technology can be used to assist in the fabrication of regular QD arrays by patterning the substrate before overgrowth. The principle is similar to other forms of lithographic or chemical etching induced quantum dot array fabrication. Molecular beam epitaxial quantum dots are expected to nucleate preferentially at specified locations previously scanned by the ion beam, avoiding undisturbed regions of the surface where uniform quantum dot nucleation, typical of self-assembly processes, will continue to be observed. As this technology has no chemical etching of a resist or mechanical imprint by a template involved, there are hardly any restrictions on the sample material [50] which is considered an advantage compared with other fabrication methods. A disadvantage

of FIB patterning is that the process is serial and thus it is slower. Only a limited field of view can be patterned in reasonable time, if the field of view becomes very large distortions of the patterns due to optical aberrations of the beam forming optics may become relevant. Regular QD arrays have been shown to have better photoelectric properties (Purcell effect [51]) and sharper spectral peaks compared with self-assembled quantum dots [52, 53].

The fabrication of regular quantum dot arrays by FIB can be separated into two main stages: the FIB patterning stage and the MBE overgrowth stage. The patterns were designed and generated with the Raith lithography software. This software can control both electron beam and ion beam to pattern. The substrate is a 2 inch (001) GaAs wafer, with a few nanometres native surface oxide (Ga_2O_3) at top. The ion beam that scans the surface of the substrate disturbs both the surface oxidized layer and the underlying crystalline GaAs, leading to regular arrays of protrusions, rings or holes, depending on the ion beam parameters, which has been discussed in section 2.2, 'focused ion beam damage'. This will change the surface morphology, and hence the surface energy near to the features. This surface energy is expected to influence the quantum dot nucleation, which itself depends on the ion setup. The varying ion beam parameter includes probe current, dwell time and accelerating voltage. A series of patterns have been milled with systematically varied ion beam parameters. In addition, the pitch size of the arrays was varied in design, too. The parameters are selected based on the previous studies and the variable parameters of our FIB instrument with some limitations.

To evaluate if the QD overgrowth is successful and has high quality, there are some statistical analysis was performed and a few indictors checked. The statistical analysis includes the number density of missed nucleation and of extra nucleation sites compared to the islands formed at each patterned site. Concerning the quality, height-to-width ratio, size uniformity, opto-electronic performance and chemical composition are important indicators. Those data are collected from SEM, AFM, micro PL and TEM cross-sectional analysis, which will contribute to later results chapter.

In the second (overgrowth) stage, the patterned substrate is moved into the MBE chamber. We can adjust the temperature and the thickness of the InAs, for the purpose of optimizing the overgrowth, but the general process and theory are the same. Prior to the overgrowth, the top native oxide layer is removed, during which the surface is monitored using reflection high-energy electron diffraction (RHEED). A clear (2×4) reconstruction is indicative of a smooth and relative oxide-free surface. Higher temperature annealing should be avoided, in order to maintain the underlying FIB pattern [54]. The first deposited layer is a 20nm GaAs buffer layer. The buffer layer helps the damaged surface to repair its crystallographic structure, so that overgrowth over patterned region could work. But the thickness of buffer layer cannot be too thick as it would otherwise fill in the FIB fabricated patterns and invalidate their influence. This is followed by an InAs layer grown. The thickness of InAs is very important. The amount of material deposited ensures InGaAs quantum dots will nucleate based on the Stranski-Krastanov growth transition, which for InAs/GaAs is known to occur at 1.8ML InAs thickness [54, 55] and trigger the formation of indium-rich islands connected by an indium-depleted wetting layer [56].

Chapter 6. Patterning and growth in practice

In practice, we have overgrown three patterned substrates. We met and solved some problems during this progress. The FIB pattern layouts and parameters were adjusted and improved with each wafer. In this chapter, the three wafers are discussed individually with their corresponding results, also some problems and challenges we have faced are addressed.

Apart from the secondary electron image, an atomic force microscopy (AFM) is involved in this project at investigation stage. AFM is very sensitive to surface roughness changes, which allows us to understand the links between the FIB nano-pattern and the formed islands and gather accurate height and length data of the islands. AFM images are captured by a VeecoNanoscopeV instrument operating in tapping (non-contact) mode. SEM secondary electron imaging (SEI) has the advantage to examine the patterned region over a large field of view with sufficient lateral resolution. AFM and SEM images are frequently shown in this chapter. A TEM cross-section lift-out sample was made to estimate the elemental composition of the islands formed by EDX analysis. To test the optical property of the island, micro-photoluminescence (PL) has been done in the Department of Physics.

6.1. Overgrowth of the 1st wafer

6.1.1. Pattern design and fabrication

Before actually putting a wafer into the FIB for patterning, we had to design the layout of the pattern and think about how to study these parameters systematically. There were a few problems and restrictions we had to concern during the pattern design.

We tried to make the arrays as large as possible, to guarantee consistency. But if the ion beam scans too far away from the optic axis over a very large field, beam aberrations occur. The maximum size of each array was limited by the working field of the FIB optic column. We decided to limit the array size to no more than 26μm x 26μm (2500 magnification). This was

big enough to place five arrays with five different pitch values into it, while each of the five arrays had at least 100 patterned sites (>10x10 site in 2-dimensions), as shown in figure 6-1. I included a code (VV AA TIME-NUM) at the very top of each pattern, which was recording the ion beam parameters, including voltage (VV), probe current (AA), dwell time (TIME) at each dot and a unique code to distinguish the patterns from each other. For example, code '30 02 100-043' means this patterned was made with the following ion beam parameters; accelerating voltage of 30kV, aperture size number 2 and dwell time of 100ms per site, with a unique code '043'.

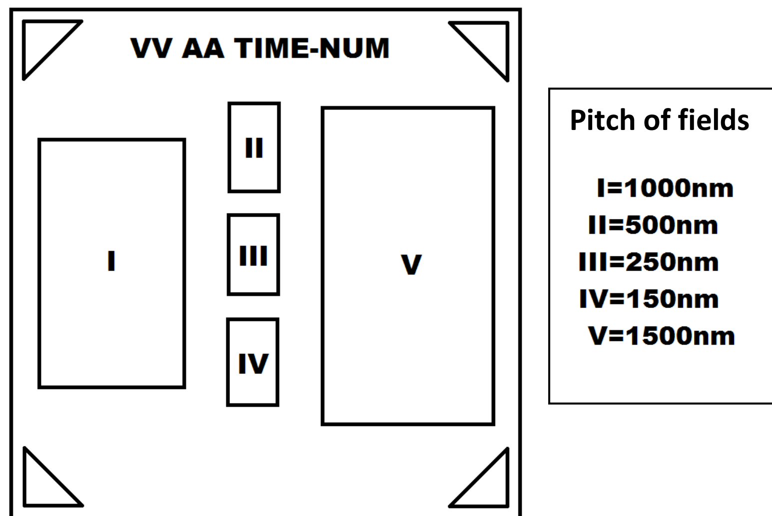

Figure 6-1 A 26µm x 26µm pattern design includes multiple array structures and a unique code at the top of the patterned region to record crucial patterning information.

We expected to have nothing but a uniform wetting layer outside the patterned region. The patterned features were very shallow and hardly visibly under an optical microscope. That made locating the patterned regions difficult. So, 100µm x 100µm big crosses were milled on the wafer surface to help localize the patterned regions, as shown in figure 6-2. A coordinate system was used by taking the advantage of the stepper motor driven stage, which helped moving from one pattern to the next pattern easier.

Each box in figure 6-2 presents a 26µm x 26µm patterned region as shown in figure 6-1. Three groups of 3x5 boxes between the six crosses were produced by using different ion beam voltages (30kV and 20kV from left to right). Each group had three columns of regions

patterned with three different sizes of apertures (#1, #2 and #3 from left to right), equivalent to different probe currents. During the practical experiment, a few patterns fabricated with aperture #5 were added, which produced deeper (>50nm) and larger holes (>200nm). Further down, in each individual column, there were five patterned regions, where the ion dose was increasing from 10^3 ions/site to 10^8 ions/site, controlled by varying the dwell time. For example, to fabricate four patterns with an ion dose 10^5~10^8 ions/site the aperture #3 (probe current = 40pA), the chosen dwell times are 0.4ms, 3.9ms, 39.4ms and 394ms respectively. However, the patterning software limits the dwell time in the range from 0.1ms to 200ms, which leads to some of the patterns were emitted. This design thus involves four parameters consisting of aperture size (probe current), accelerating voltage, pitch size and dwell time, as shown in table 6-1. With this design, we should be able to systematically and efficiently compare all interesting parameters.

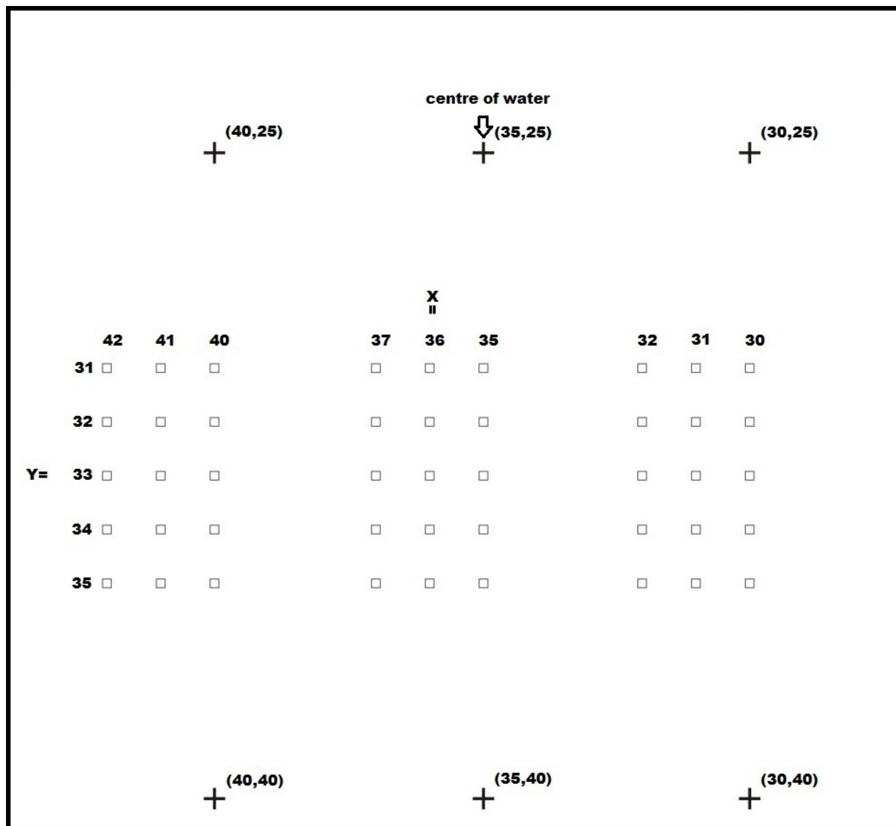

Figure 6-2 Patterned regions of wafer 1. There are six crosses to help localize the patterned arrays, which are represented as square boxes.

Accelerating voltage [keV]	Probe current [pA]	Ion dose [ions/site]	Pitch [nm]
20	1.5	103	150
30	4	104	200
10	40	105	500
		106	1000
		107	1500
		108	

Table 6-1 The ion beam parameters explored.

To place a whole 2 inch wafer into the FIB sample chamber, a special aluminium sample holder was made by the department workshop. There are three copper clips to hold the wafer, which also proved a very good conduction path between the wafer and ground.

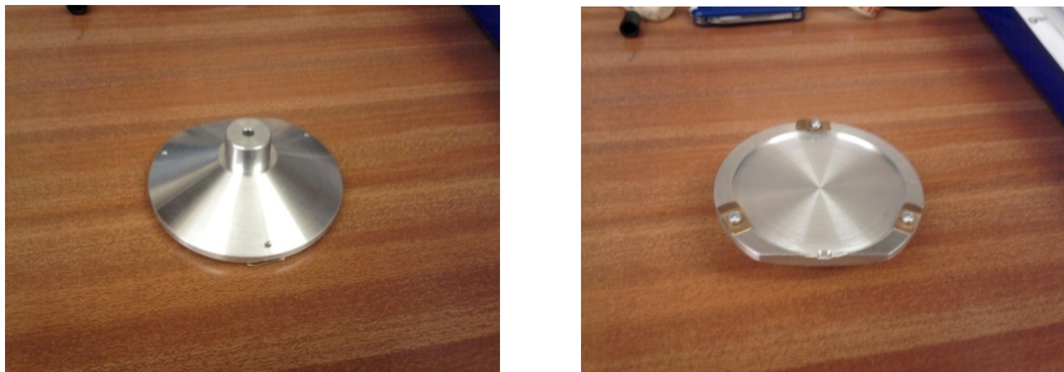

Figure 6-3 Two inch diameter aluminum sample holder

After the patterning was finished, the wafer was moved into the MBE (V80 MBE from Oxford instruments) for overgrowth. The patterned wafer was placed in the preparation chamber and degassed at 150°C for 10 hours (over night). Then, the sample was annealed at 580°C for 10min under Ga overpressure. This process removed all oxide on the surface and partially repaired the ion implantation damage. The growth stage was operated at 510°C. 2ML of InGaAs was deposited as monitored by the RHEED. This process should produce a layer of QDs at the surface.

6.1.2. Difficulties during fabrication

In practice, there were a few limitations induced due to hardware or software and some modifications from the original planning were made.

- The FIB pattern design and exposure software by Raith company limits the dwell time to between 0.01ms and 200ms. During the design stage, a few patterns requires a dwell time far more than 200ms on the plan. These parts of the patterns were cancelled.
- The alignment of the 10kV ion beam proved difficult. Because the extraction voltage was so low, the suppression voltage was reversed to pull more ions from the source rather than to focus the beam as mentioned in chapter 2. This low voltage function was hardly used before. Due to a lack of experience, the use of 10kV ion beam patterns was not perused further, despite low voltage patterns being desirable.
- An additional column of patterns was attempted. This was patterned with an accelerating voltage of 30keV and a probe current of 200pA. This attempt was made in order to see if a high probe current works for this application. But the resulting holes a diameter larger than 200nm, which was considered too big and too deep for this approach.

6.1.3. Result and further improvement

The overgrown structures were analysed by AFM and SEM. A non-contact probe tip (model RTESP10 from Veeco) was used for this project. Two images as shown in figure 6-4 were captured under non-contact mode. The complete images had 1024x1024 pixels over a 7μm x 7μm (figure 6-4a) or 5μm x 5μm (figure 6-4b) field of view, so that each pixel was 6.8nm or 4.8nm in size. This sampling was high enough to display surface features and islands clearly, which had an average diameter of typically 30nm. Figure 6-4(a) displays a part of patterned area (30 1 106-004). As mentioned before, the code means that the pattern was produced with 30keV ions using aperture #1 and a dwell time of 106ms. The scale bar indicates a distance of 500nm between the holes. Figure 6-4(b) displays a part of patterned area with code (20 2 5.3-028), which means pattern was done with 20keV ions using aperture #2, a dwell time of 5.3ms and the distance between holes was 1000nm.

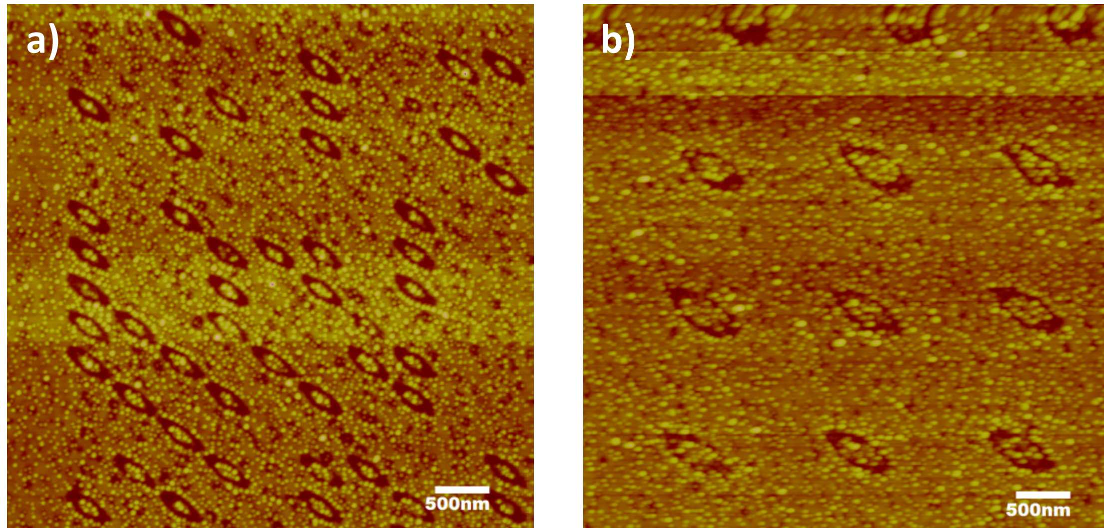

Figure 6-4 Image number 027, Code (30 1 106-004) (a) and image number 048, code (20 2 5.3-028) (b). The image size was 1024x1024 pixels over a 7µm x 7µm region. Two images are showing patterns with different pitches.

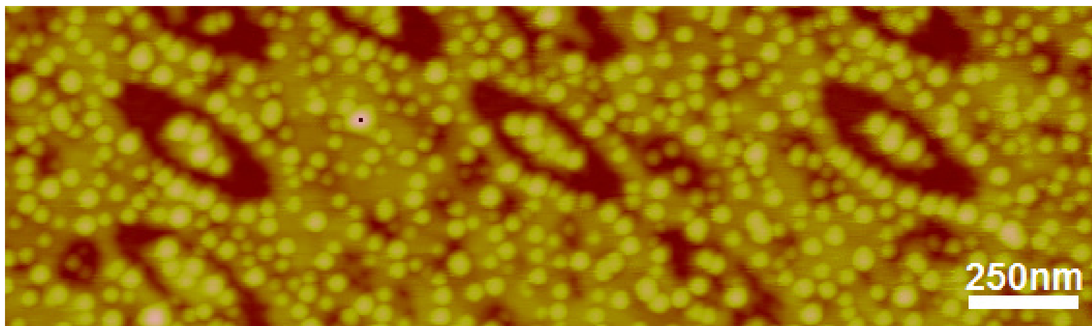

Figure 6-5 The magnified image shows that quantum dots do form preferentially near the edges of the patterned holes.

From the AFM images, it is clear to see that quantum dots do form preferentially near the edges of the holes, as shown in figure 6-5. This behaviour proves the nucleation of self-assembled quantum dots was influenced by the FIB pattern. There are also unwanted quantum dots that nucleated between the patterned holes and outside the arrays. It points out that either the influence from the patterns was too weak to force enough nearby material to form QDs at the patterned sites only or 2ML deposit of InAs is enough to form quantum dots everywhere regardless of the influence of the FIB pattern. The dark region of the sidewalls of the holes could mean the depth of the hole was out of the probe's dynamic range (too deep) or that those areas were dot free. The elongated shape is caused by astigmation in a misaligned ion column. Another interesting result is that some QDs were missing after the anneal and overgrowth. The reason for their vanishing is probably related to the annealing

process, which roughened the surface too much. Parts of the holes are not flat, while other parts completely vanish. No SEM or AFM images were captured between patterning in the FIB and the sample being put into MBE for annealing and overgrowth, hence no data concerning the dimension of the produced nano-patterns were available, which was improved in future experiments.

The first try was not as good as expected, but some information could be gathered from it, which proved useful for the patterning and overgrowth at subsequent wafers. Based on the first wafer, developments and corrections could be made.

- The wafer layout and pattern design was successful. Different FIB patterning parameters are systematically combined together. Big cross marks made searching the patterned areas convenient under optical microscopy and SEM, and the coordinate system made moving from pattern to pattern easy and quick. We did not maximize the use of the 26μm x 26μm patterned regions and five arrays were located too far away from each other, which made AFM image capture difficult. Multiple scans had to be done, which was very time consuming. The location of the five arrays can be organized better to produce more holes in each array and ensure a single AFM scan can gather more information. The patterns with similar ion parameters can be placed closer to each other. Spacing each 26μm x 26μm patterned region 3mm from each other in has been proved unnecessary; and a compressed layout will save a lot of time when locating different regions for investigation.
- The results show how important the alignment of the ion optical column is. With an elongated beam shape, the ion beam hardly generates effective patterns and produces unreliable data. Improving the beam alignment will be the most important task in the next experiment.
- The quantum dots formed outside patterned regions and between the patterned holes prove 2ML of InAs is too much to produce controlled quantum dots only at patterned sites. Missing QDs and the deep holes mean that annealing (repairing) does not fully achieve the goal we want. The annealing must be improved.

6.2. Overgrowth of the 2nd Wafer

6.2.1. Improved wafer layout, pattern design and overgrowth

A whole new wafer design was made to make the ion beam patterning procedure easier and faster, as shown in figure 6-6(left). There were a few horizontal rows of 100µm x 100µm crosses for location reference, similar to the previous design. The distance between two adjacent crosses is reduced from 5mm to 3mm in X direction and 5mm in Y direction. The shrinking saved significant time in accurately moving and adjusting the beam during both patterning stage and investigation stage. This design included two ion beam voltages of 20keV and 30keV; 10keV patterns were removed due to beam alignment problem. The probe currents were 2pA (only 30keV), 4pA, 40pA and 170pA. There were seven combinations of different accelerating voltages and probe currents, thus there were seven columns of crosses in the wafer design and each columns represented a combination of the probe current and accelerating voltage, as shown in figure 6-6.

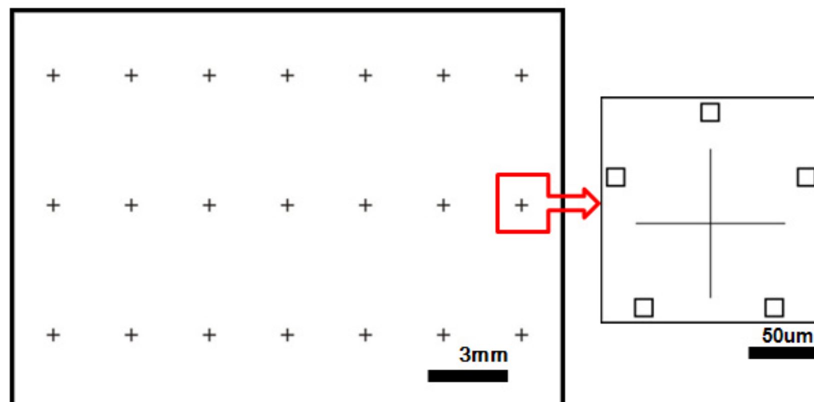

Figure 6-6 Wafer 2 design.

Taking a closer look at each cross, there were five 26µm x 26µm square patterned regions surrounding each cross, as shown in figure 6-6. The five patterns were made with five different dwell times of 1ms, 5ms, 20ms, 100ms and 200ms. The chosen dwell times were completely different from the first wafer. For the previous wafer, the dwell time was taken based on ion dose, to implant 10^3, 10^4, 10^5 etc ions per site. But in consecutive FIB experiments, the ion beam current was not as stable as expected, as described in previous

chapter and decreased by about 15% from initial values during the patterning. We decided to adjust the dwell time itself and work out the ion dose later.

The pattern design was improved to serve the later investigation stage better by using the experience from the first wafer. The 26µm x 26µm patterned region was also modified as shown in figure 6-7. This layout had five arrays that were positioned very close to each other as before. A single scan covering the grey box (about 10µm x 10µm) included parts of each patterned arrays, so this was a more convenient design. The new design saved a lot of time compared with scanning multiple locations over the 26µm x 26µm patterned region to gather all required information concerning different pitches. The most crucial part is the ion beam alignment. The ion beam was carefully aligned and tested before each patterning by milling holes on a flat GaAs surface and examining the shape of the resulting holes.

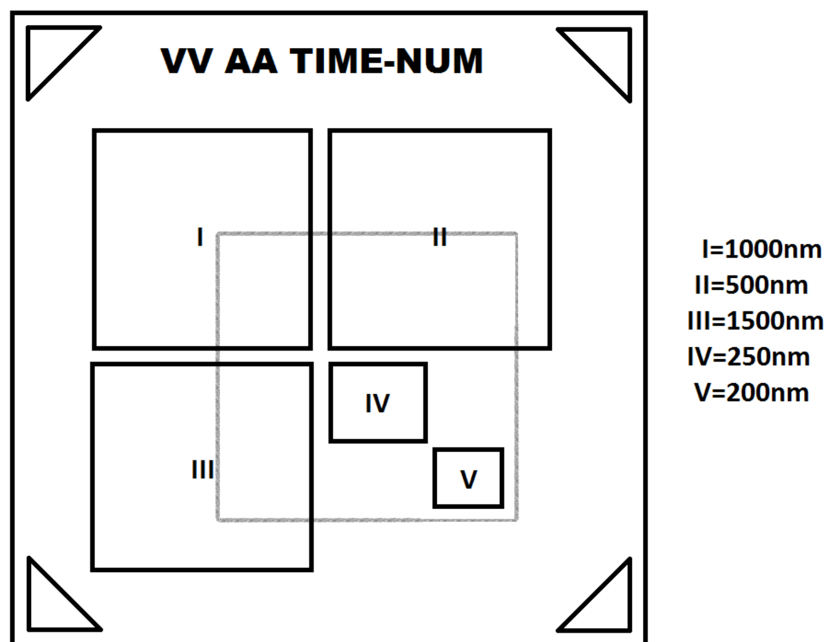

Figure 6-7 Re-design of the patterned region of wafer 2.

More work was done between patterning the substrate and transferring it into the MBE chamber. Before MBE growth, the sample had been investigated with atomic force microscopy and scanning electronic microscopy. The images are presented in figure 6-8 and figure 6-9 and will be discussed later. These pairs of images document the influence of nano-patterning on the quantum dot overgrowth.

After AFM and SEM imaging, the substrate was transported into the MBE growth chamber. First, the sample is degassed at 400℃ for 1 hour to remove carbon surface contamination. Prior to the overgrowth, the top native oxide layer is removed under an arsenic flux at 580℃ for 30 minutes, during which the surface is monitored using RHEED. A clear (2×4) reconstruction is indicative of a smooth and relative oxide-free surface. Higher temperature annealing should be avoided, in order to maintain the underlying FIB pattern [54]. The first deposited layer is a 20nm GaAs buffer layer at 580℃, followed by a 1.5ML InAs layer at 520℃, i.e. for wafer 2 less InAs was deposited. The growth rates of GaAs and InAs are 0.5ML/s and 0.02ML/s, respectively. The buffer layer thickness is well controlled so that it reduces the effect of surface ion damage and flattens the surface but yet does not fill in the FIB fabricated patterns. During growth, the thickness of InAs is very important. The amount of material deposited ensures InGaAs quantum dots will nucleate based on the Stranski-Krastanov growth transition, which for InAs/GaAs is known to occur at 1.7-1.8ML InAs thickness [6, 54] and trigger the formation of indium-rich islands connected by an indium-depleted wetting layer [57].

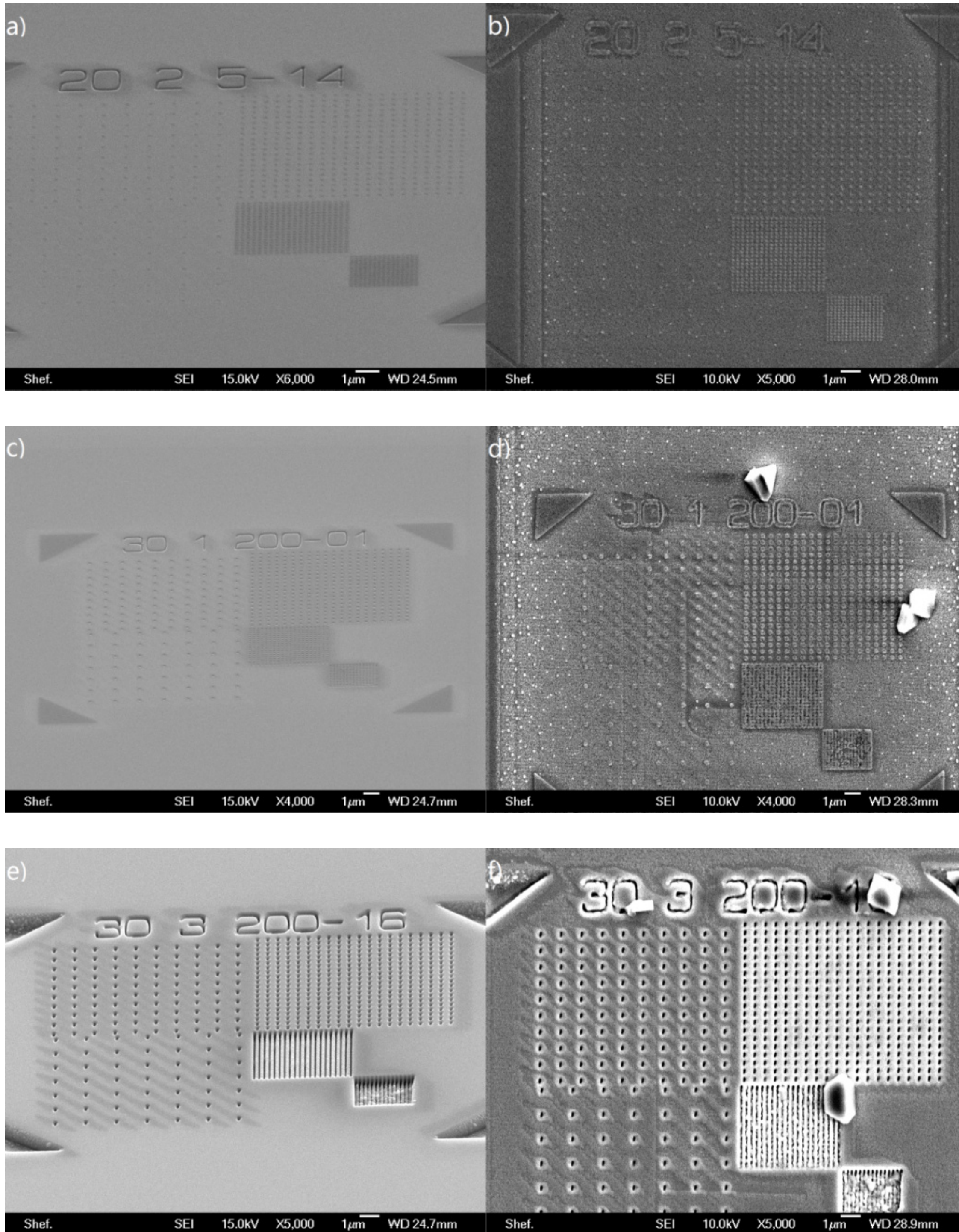

Figure 6-8 SEM secondary electron images captured before (a, c, e) and after (b, d, f) overgrowth. When comparing secondary electron images directly after patterning but before overgrowth with those after *overgrowth,* the 55° sample tilt for FIB milling gives an apparent foreshortening of the vertical due to the projection, which has not been corrected here. The ion dose increases from top to bottom. Patterning parameters are:
a),b):20keV, 5pA, 5ms dwell time;
c),d): 30keV, 2pA, 200ms dwell time;
e),f): 30keV, 40pA, 200ms dwell time.

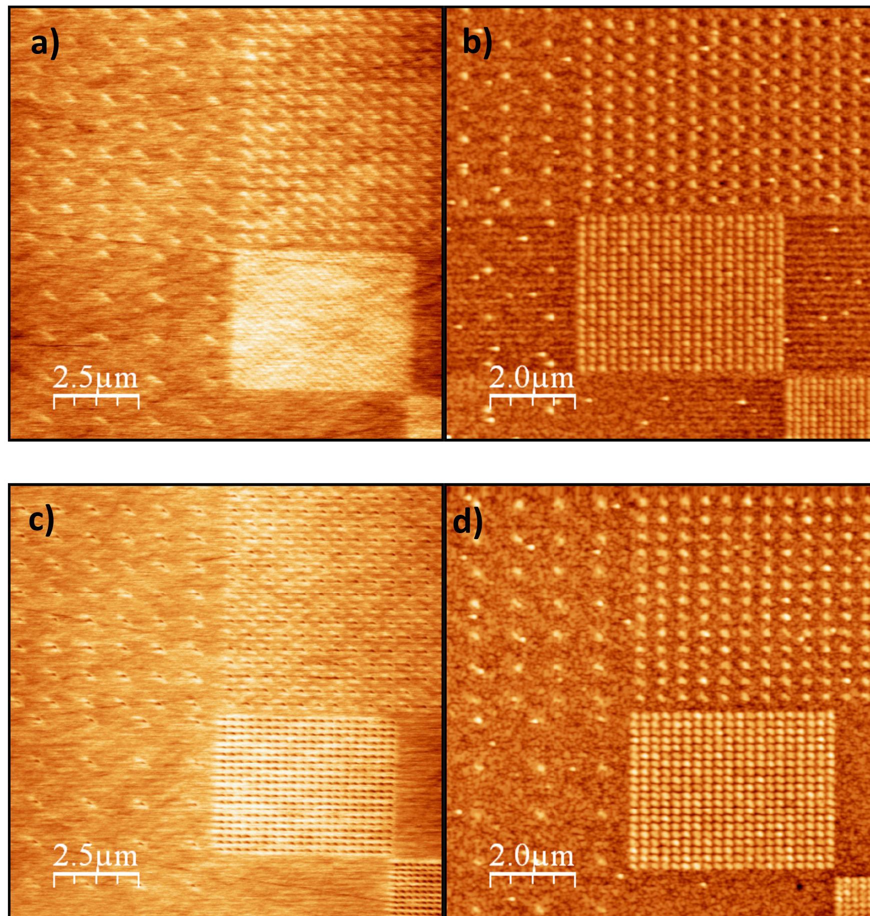

Figure 6-9 AFM images captured in tapping mode before (a,c) and after (b,d) overgrowth. The field of view is 10µm and the sampling is 10nm/pixel. a) shows the Ga^+ implantation created hillock features while in c) it created tiny holes. Both patterns successfully triggered nucleation of QDs, as b) and d) demonstrate. The patterning parameters are:
a), b): 20keV ion energy, 5pA ion probe current, 5ms dwell time
c), d): 30keV ion energy, 20pA ion probe current, 5ms dwell time

6.2.2. Results for wafer 2

Corresponding to different combinations of accelerating voltage and ion dose, there are three types of damage at impact which we have discussed in chapter 2, as sketched in figure 6-10. From left to right, the focused ion beam induced damage is increasing. After annealing repair, depending on the ion beam damage, we have hillock, amorphous layer or hole at the patterned region. It should be noted here that once a hemispherical hole has been sputtered out, ions will hit its sides with a higher sputter yield but also higher redeposition rate, as a result of which the sputtering rate at the side walls is much lower than at the bottom of the holes, and the holes will thus extend preferentially in depth, creating holes of very high aspect ratios and almost vertical side walls [58]. Such holes remain almost the same after

annealing and will affect the overgrowth in ways different from the other two before mentioned mechanisms, as the surface is strongly corrugated and the sidewalls of the holes can form various facets with respect to the [001] surface normal.

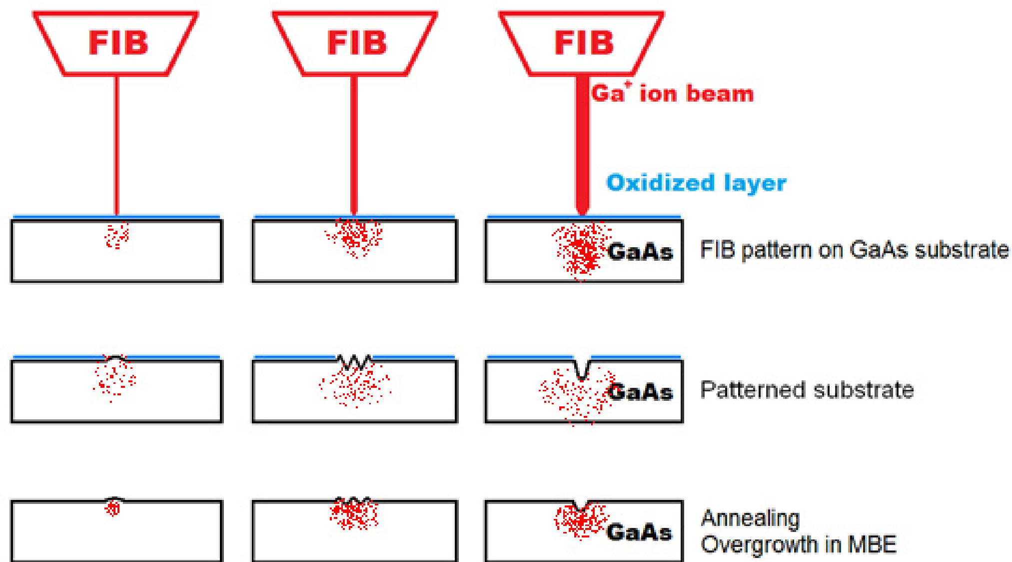

Figure 6-10 Patterning a GaAs substrate by FIB under different conditions, with ion beam energy and/or dose increasing from left to right, leading to lattice swelling by ion implantation (left), amorphisation (centre) and finally sputtering (right).

Different types of damage result in different nucleation geometries of structures, as captured by both AFM and SEM and shown in figure 6-11. The fabricated patterns have distinctly different forms. After growth, from the images captured, we clearly found InGaAs was more likely to nucleate within the ion beam patterned area. Structures formed at the patterned locations fell qualitatively into three classes: islands, rings or deep holes as shown in figure 6-10. Islands were mainly found in the regions previously scanned by FIB with short dwell times and low probe currents [59, 60], where the ion beam implantation produced only very shallow holes or even hillocks rather than holes. When the dwell times and probe currents were increased, the ion beam produced deeper holes during patterning and the material deposited during overgrowth nucleated preferentially in the form of rings surrounding the edges of patterned rather the shallow depressions. When dwell times and probe currents increased further, the drilled holes became too deep to be repaired by annealing and remained after overgrowth, surrounded by mounds that could form rings only if clearly separated laterally, as shown below in figure 6-11c. In regions not patterned by FIB, QD nucleation was random and generally less likely.

By analysis of table 6-2 and figure 6-12, the ion dose range which is more likely to produce islands, is clear. The patterns produced with a low accelerating voltage are more efficient to attract islands nucleating above them, due the ion projected range is shallow and the radiate damage region is closer to the substrate surface, thus the influence is stronger.

20keV					
	Aperture Ion current	#1 (1.5pA)	#2 (4.0pA)	#3 (40pA)	#5 (200pA)
Dwell time [ms]	200	N/A	dots	holes/rings	holes
	100	N/A	dots	holes/rings	holes/rings
	20	N/A	dots	dots/holes	dots/rings
	5	N/A	dots	dots/holes	dots
	1	N/A	dots	dots/holes	dots
30keV					
Dwell time (ms)	200	dots/rings	holes/rings	holes/rings	holes
	100	dots/holes	holes/rings	holes/rings	holes
	20	dots/holes	dots/holes	holes/rings	holes/rings
	5	dots/holes	dots/holes	dots/holes	dots/holes
	1	dots	dots	dots	dots

Table 6-2 Parameters for producing InGaAs quantum dots. The 20keV FIB with probe current 1.5pA produced a signal-to-noise ratio too low for evaluation, and this column is marked as N/A in the table.

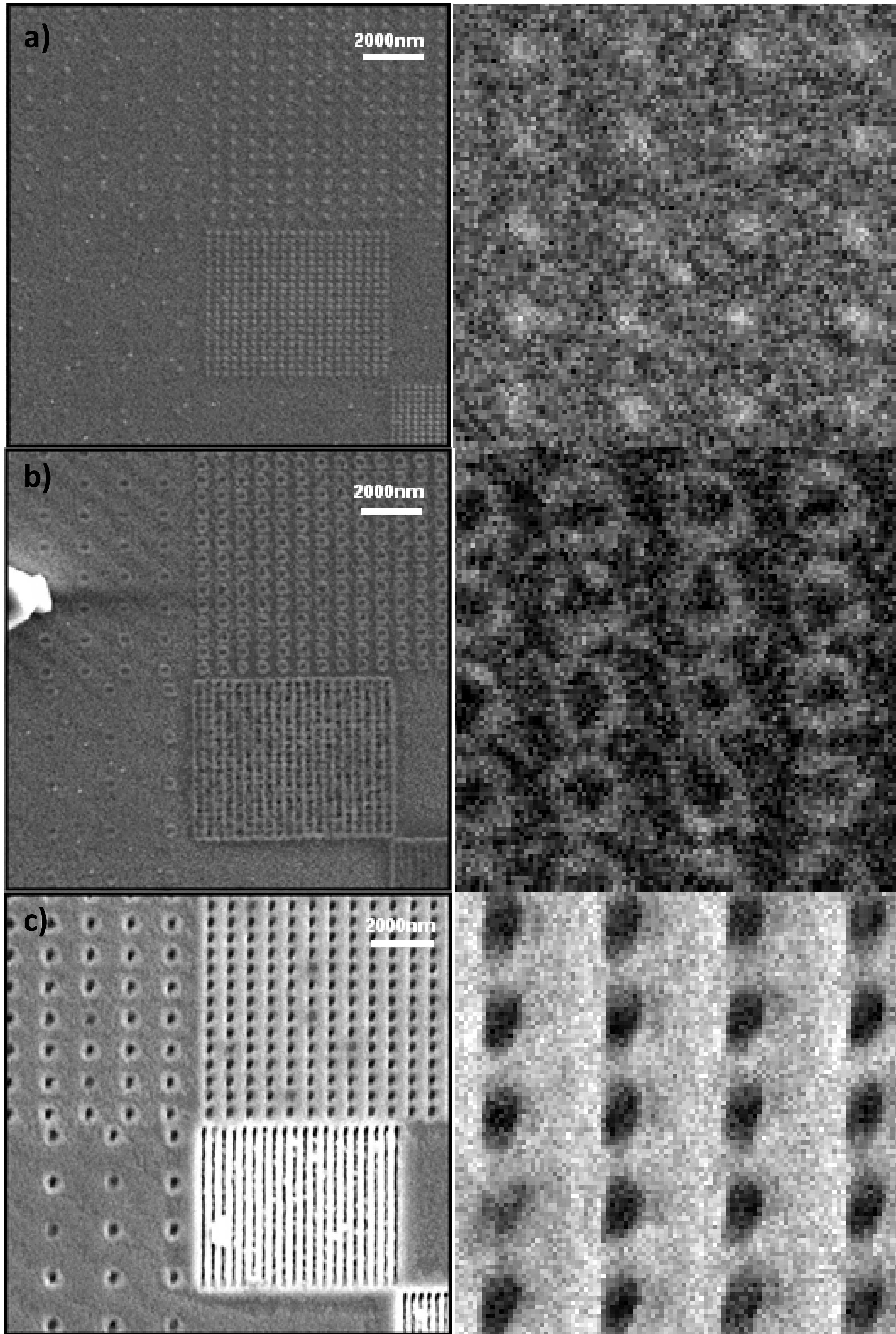

Figure 6-11 Three distinct types of In(Ga)As nucleation geometries with increasing ion dose from top to bottom with magnified detail images: islands (a), rings (b) and deep holes (c)

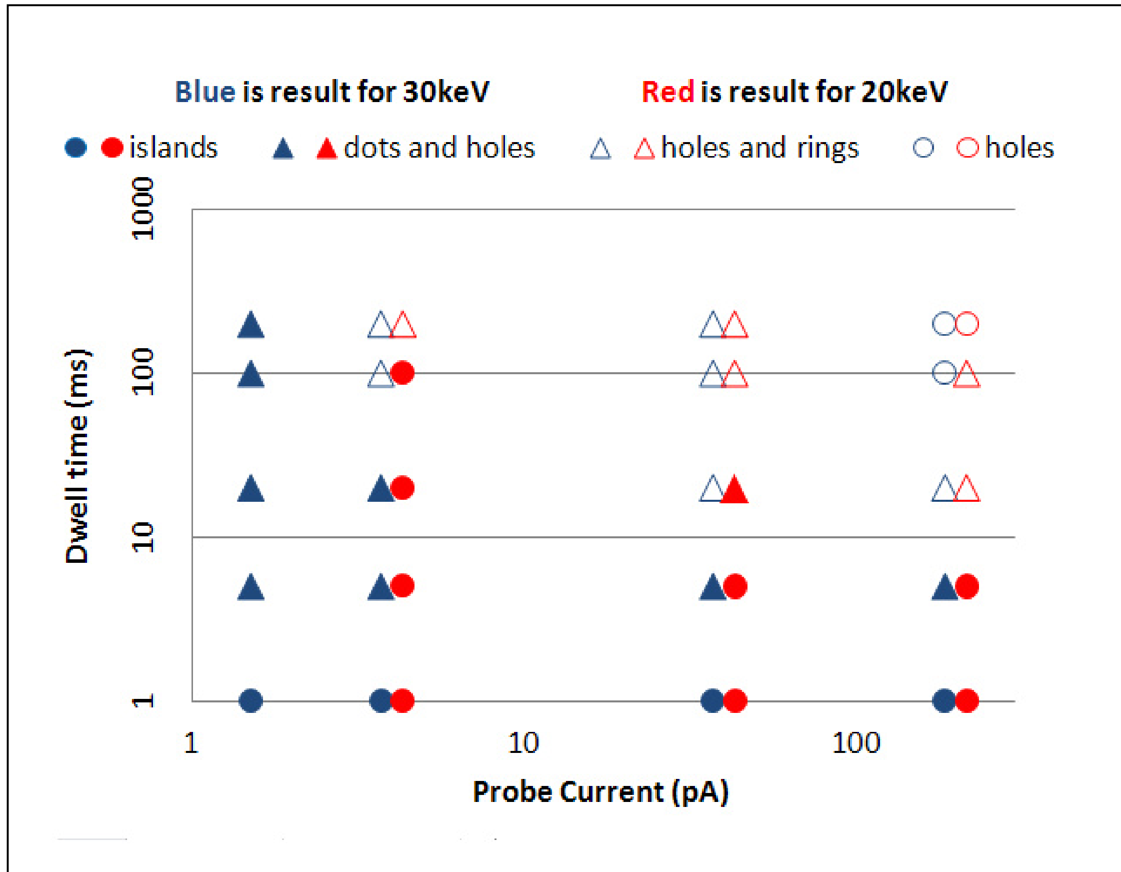

Figure 6-12 FIB patterns milled with short dwell times and small aperture sizes (low ion dose) produced islands. On the other hand, long dwell times and big aperture sizes (high ion dose) produced In(Ga)As rings or left only holes with some InGaAs nucleating preferentially at their edges. Most of the information has been collected from SEM.

The following investigation is focused only on islands, fabricated by MBE overgrowth of low ion dose FIB patterning. We have determined the relationship between the dimensions of islands and the FIB parameters. The data include the heights and diameters of the InGaAs islands, the pitch size of the arrays and the distribution homogeneity of the structures formed. The height and diameter of islands are measured by analysing AFM images as shown schematically in figure 6-13. The measurements were collected from four patterns and comprise data from three arrays formed at 20keV ion energy and 4pA probe current with three different dwell times (1ms, 5ms and 20ms), as well as from one array formed at 20keV ion energy but with the probe current increased to 40pA at a dwell time of 1ms. From figure 6-14a can be seen that the island heights are almost constant, covering a narrow range from 12nm to 25nm, with values slightly increasing with pitch. The diameter scales with the square root of the pitch, as can be seen from figure 6-14b, and is also increasing with the dwell time and probe current, which is not so obvious from the diagram. The result confirms the

possibility of controlling the nucleated quantum dot size. However, it is clearly difficult to create islands under 100nm in diameter and below 10nm in height, which will be a prerequisite for strong quantum confinement effects in optical spectra. As the amount of deposited material per unit area is fixed (1.5ML InAs) and the volume of each island can be estimated as shown in figure 6-13c, the total volume of material being converted into dots per unit area ($T=V_{QD}/pitch^2$) can be used to determine the fraction of InAs located in QDs rather than in the wetting layer. More material being converted into dots means the FIB pattern has a stronger influence on the nucleation of the islands.

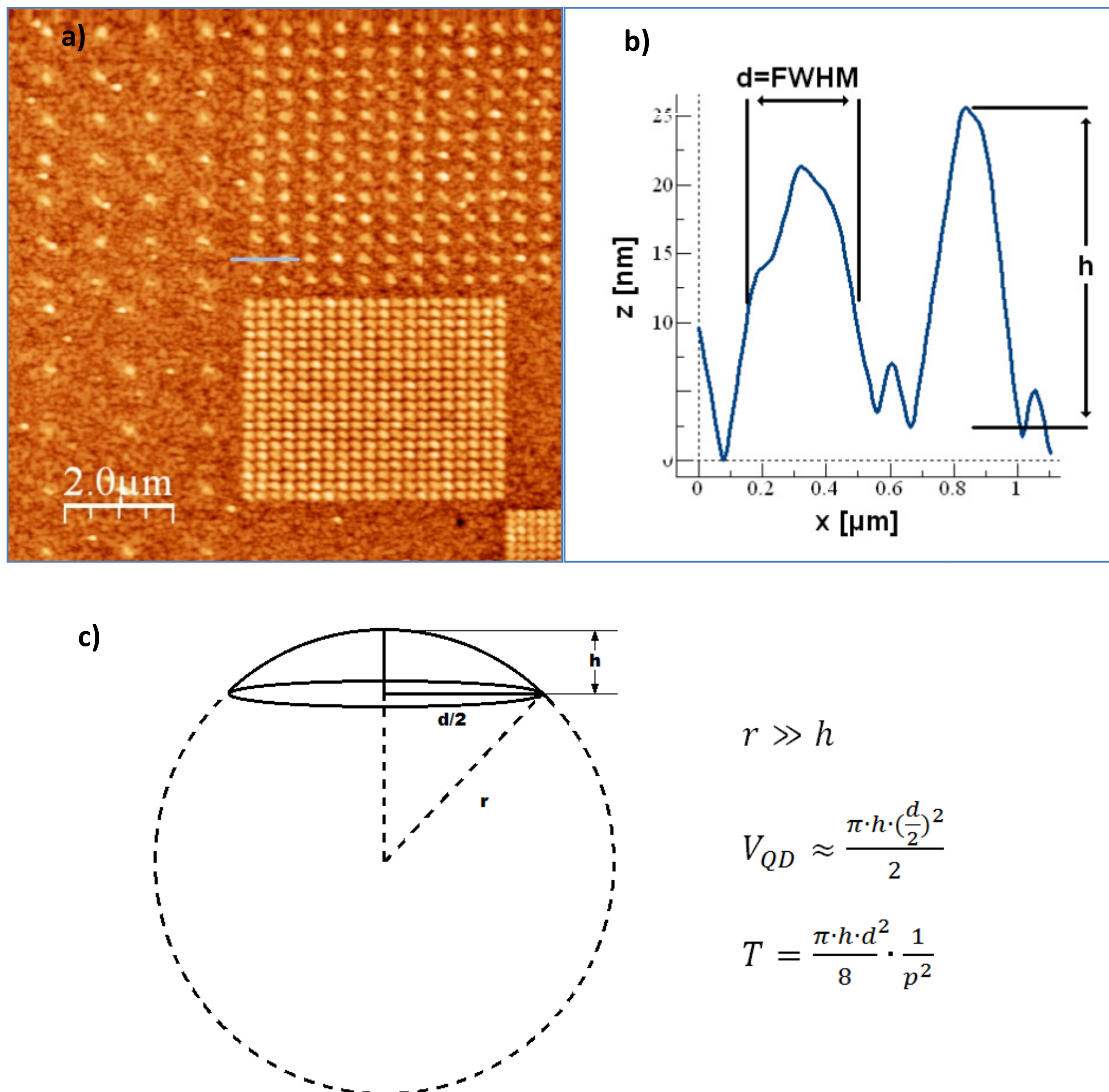

Figure 6-13 The size of quantum dots is measured by analysing AFM images. The heights are measured as peak heights above background and the diameters are measured as the full widths at half maximum (FWHM). The volume, V_{QD}, of quantum dots is then calculated assuming the geometry of a spherical cap as sketched in c).

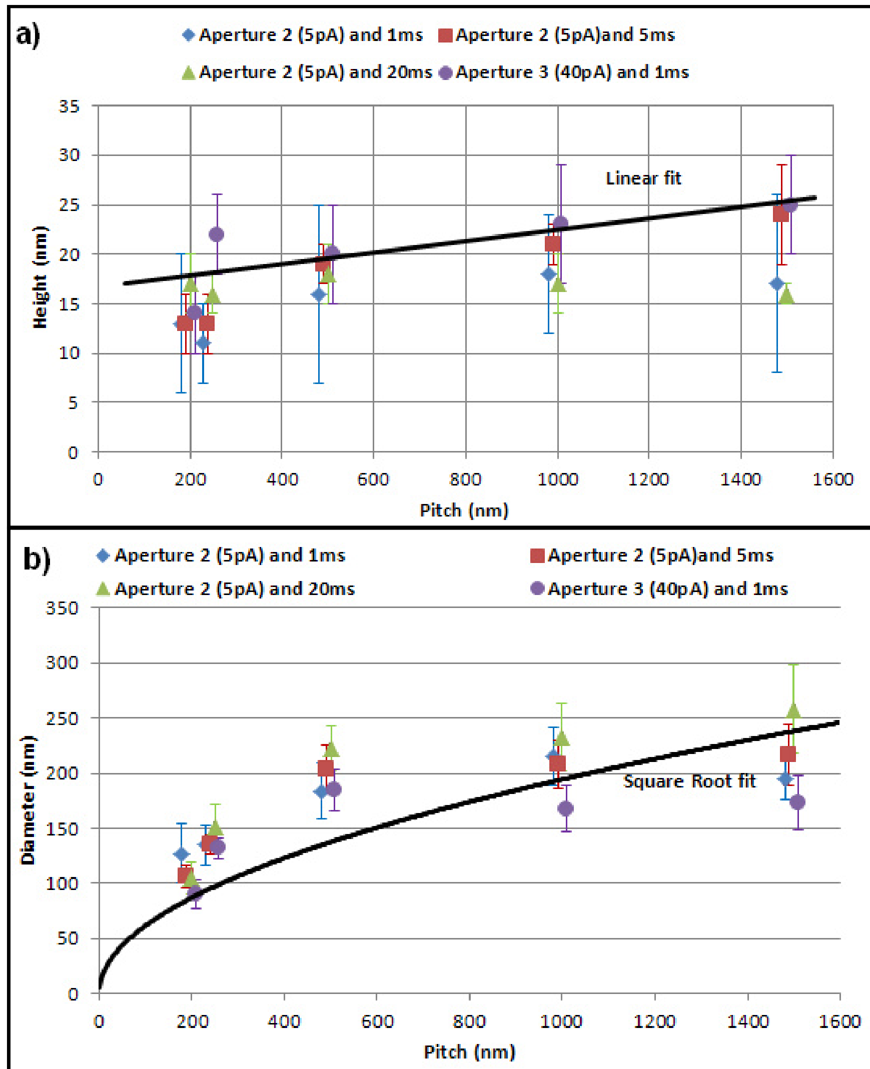

Figure 6-14 Plots of height (a) and diameter (b) of islands nucleated from four different FIB patterns at 20keV.

For each test pattern, the ion beam parameters and gun alignment were kept fixed. As mentioned before, each pattern contained 5 sub-arrays with different pitch sizes of 200nm, 250nm, 500nm, 1000nm and 1500nm. This design helped us to analyse the relationship between the pitch sizes of the arrays and the distribution homogeneity of the structures formed, as shown in table 6-3. We evaluated each pattern of sufficient signal-to-noise ratio with respect to two characteristics: the probability, P^+, of islands forming in unwanted positions ('false positives': islands formed outside the patterned sites) and the probability, P^-, of islands not having formed at patterned sites ('false negatives': islands missing at patterned sites). The results show that only patterns with a pitch of ≤500nm create acceptable QD arrays with less than 3% nucleation of islands outside the pattern and less than 3% of islands missing at the patterned sites. This result agrees with Hull's study on the distribution control

of SiGe QDs grown on patterned silicon [61]. In general, the failure rates P^+ and P^- increase with ion dose, as shown in figure 6-15, which again confirms that low ion dose patterns create more perfect arrays of smaller islands, which are more appropriate for opto-electronic applications. Generally, $P^+ > P^-$, i.e. it is more likely additional islands form off patterned sites than islands are missing at patterned sites. There is also the possibility of nucleating multiple QDs on the same specific site. The number of QDs formed per site depends on the geometry of the patterned feature and the overgrowth temperature [52, 62].

20keV ion energy, 4pA probe current and 5ms dwell time					
pitch [nm]	1500	1000	500	250	200
P^- [%]	6	7	3	<0.1	<0.1
P^+ [%]	67	18	2	0.3	0.4

Table 6-3 Statistical distribution of islands in patterned areas for one set of parameters. This pattern was created with fixed ion beam and column alignment and it contained five arrays with different pitches.

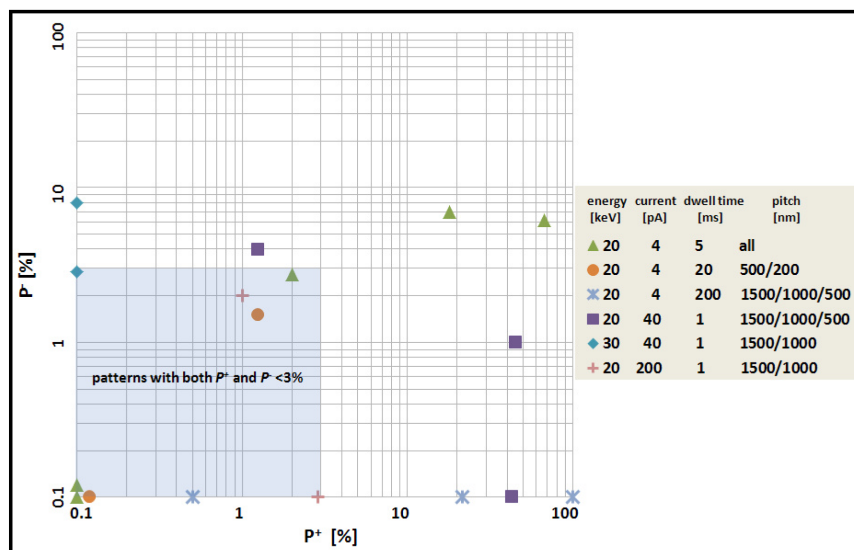

Figure 6-15 Comparison of two types of island nucleation defects. P^+ describes the fraction of islands nucleated off patterned sites, P^- the fraction of islands having failed to nucleate at patterned sites.

6.2.3. Micro-photoluminescence investigation

Micro photoluminescence (μ-PL) studies were performed at room temperature after overgrowth and SEM and AFM imaging. The exciting laser (green) had a diameter of ~5μm, a wavelength of 532nm and 1-2mW power. Micro-PL measurements were performed scanning the laser beam along a straight line from positions outside the patterns, where QDs had randomly nucleated on the surface, across the entire patterned area with a step size of

5μm, as shown in figure 6-16a. The spectra are not as sharp as expected [63]. There are two rather broad peaks in the spectra at ~878nm (1.41eV) and ~1152nm (1.08eV). They are related to the underlying GaAs substrate and the InGaAs QD signal. From the latter peak wavelength we can estimate the compositional ratio of Ga:In atoms as 74:26 (i.e. $In_{0.26}Ga_{0.74}As$), assuming Vegard's law for bulk materials can be applied here as well [56]. The FIB patterned area shows higher signals for both peaks, where the signal from the GaAs substrate increases more rapidly. The enhanced optical contributions from both the pure GaAs and the InGaAs islands may be explained by indium atoms from the wetting layer formed upon epitaxy having been more efficiently integrated into the islands when the surface has previously been FIB patterned, confirming the formation of QDs.

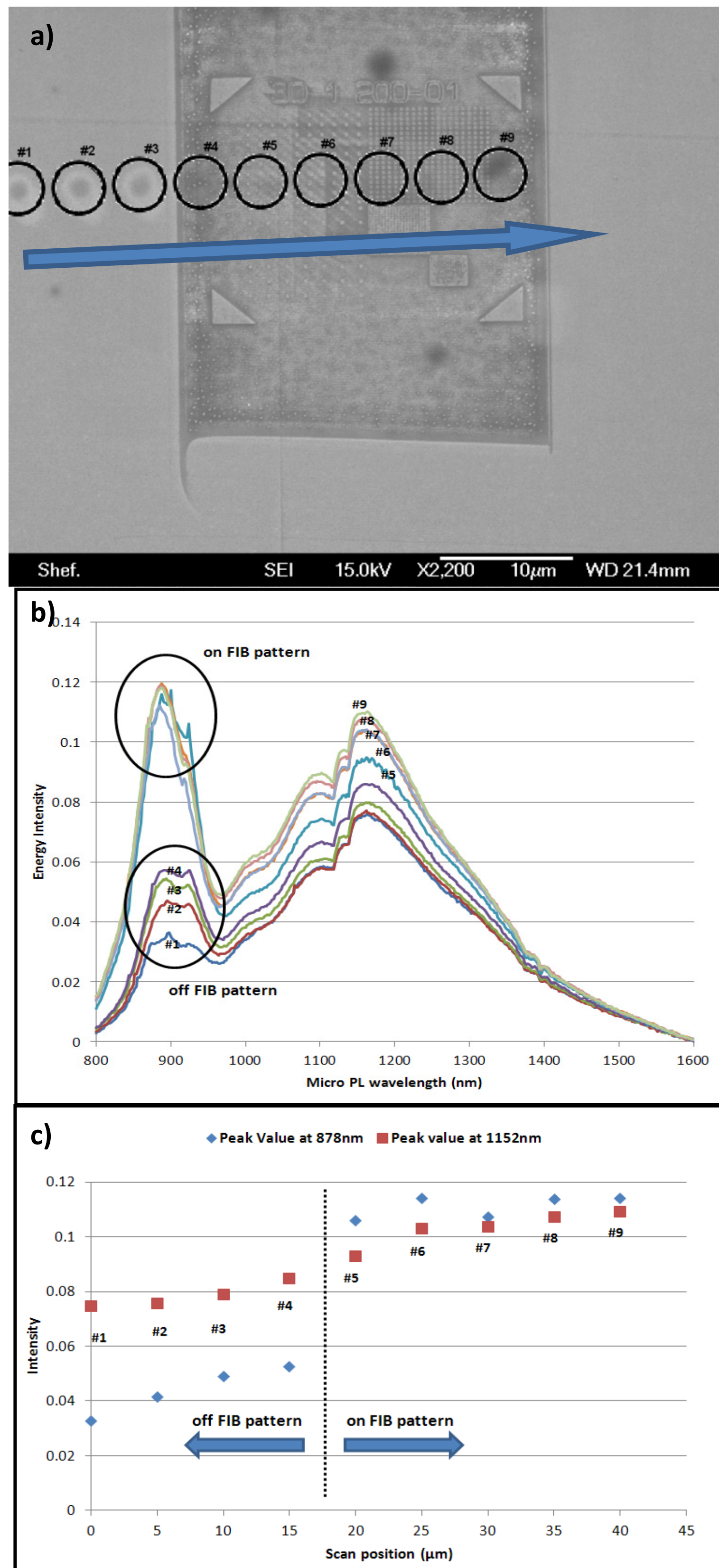

Figure 6-16 SEM image of array investigated by μ-PL. Scan started ~15μm away from patterned regions and moved 40μmacross the patterned area (a). Set of experimental μ-PL spectra (b). The intensities at two wavelengths, 878nm (GaAs) and 1152nm (InGaAs), were extract at each scan position (c).

6.2.4. TEM cross-sectional study of InGaAs QDs grown

To confirm the result from the μ-PL study and to have elemental analysis of the formed QD structures, TEM cross-sectional study of InGaAs QD was done. The TEM study was done on the JEOL J2010F (S)TEM using energy-dispersive X-ray spectroscopy (EDS) analysis. Because uncoated QDs are very sensitive to ion beam damage, the TEM sample preparation was different from a standard one. As discussed before, we used electron beam assisted deposition first before using ion beam assisted deposition, to avoid ion beam damage to the sensitive surface features. The region of interest was carefully chosen to produce a TEM lamella containing multiple QDs in a row. The sample is crossing the patterned area of a very small angle (2~3 degrees) to ensure the lift-out membrane consisted of a row of QDs which at least one QD being cut through the geometry centre and providing maximum diameter as shown in figure 6-17. From the STEM bright field image, figure 6-18, the QDs have ~150nm diameter. The chosen patterned area was an array with a pitch of 200nm, from the pattern '30 1 20-03', which means this area was fabricated with 30kV accelerating voltage, 1.5pA probe current and 20ms dwelling time.

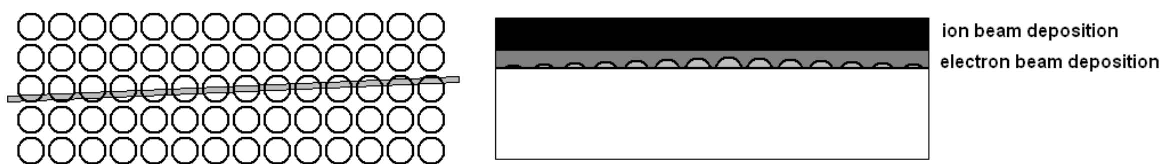

Figure 6-17 The region of interested crossed a few rows of QDs under a very small angle to ensure at least one dot would be cut through the geometry centre and providing maximum diameter in the finished lamella.

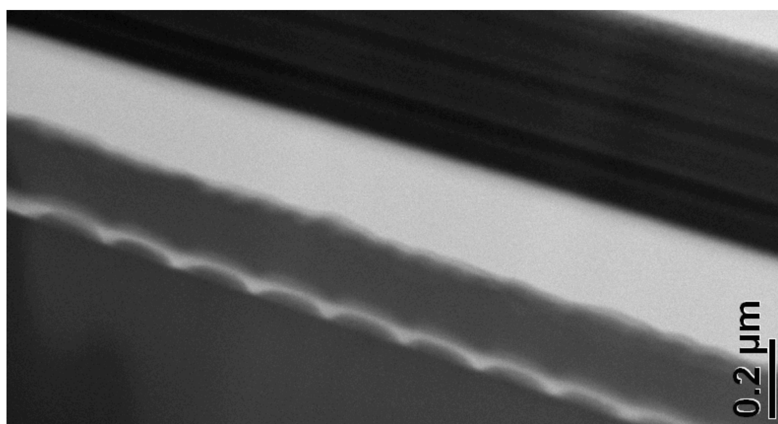

Figure 6-18 Part of a 2048x2048 pixels bright-field STEM image of the cross-sectional sample, with a magnification of 30K and a medium spot size of 0.5nm.

The selected elements in the EDS analysis are shown in table 6-4 with the corresponding counts. Figure 6-19 shows the EDX spectrum from a scan near the top of the islands. It is very challenging to evaluate the In composition from a very weak In signal. Despite the ED mapping analysis taking a few hours, the counts of In were still low and the signal was hardly distinguishable from the background noise. All of the image analysis and processing were done by Digital Micrograph (DM). The recorded elemental maps are in tiff format and were transformed back to original image to present the as-recorded intensity distribution by multiplying the maps by the maximum count numbers and then dividing by 255, as the grey level of the image has been stretched to 8bits when it was converted to tiff format.

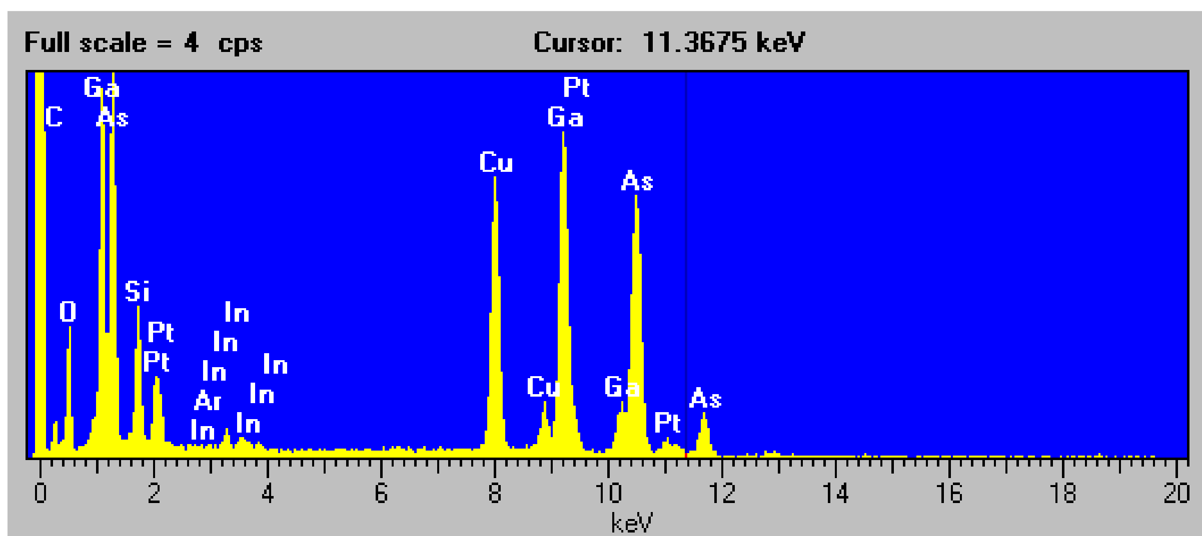

Figure 6-19 The X-ray spectrum from a scan near the top of the island. The x-ray lines are marked at their peaks.

Selected elements from X-ray maps with corresponding maximum counts				
C(Kα) 17	Ga(Lα1) 57	As(Lα1) 54	Pt(Mα1) 68	In(Li) 8
O(Kα) 23	Ga(Kβ) 35	As(Kα) 57	Pt(Mβ) 9	In(Ln) 6
Si(Kα) 34	Ga(Kα) 73	As(Kβ) 18	Pt(Lα1) 19	In(La1) 9
			Pt(Lβ1) 28	In(Lβ1) 8
				In(Lβ2)7
				In(Ly1) 8
				In(Ly2) 7

Table 6-4 The selected elements in the ED map with corresponding maximum counts.

First, we will estimate the In composition from the L line, due to the major In signals coming from the L line group. All involved elements are shown in equation below. The low signal-to-

noise ratio of In is still be biggest issue here. To solve that, the technique of extracting information from a noisy image is described.

$$X_i = \frac{(I_i - B_i) * k_i * abs_i \div A_i}{\sum_{j=1}^{n} (I_j - B_j) * k_j * abs_j \div A_j} \tag{6.1}$$

The above equation describes how to extract a concentration x of an element i at percentage if the k-factor are referring to weight percentage. As x in $In_xGa_{1-x}As$ refres only to the group III sub-lattice, we get:

$$\frac{x_{In}^{L}}{2} = \frac{In\ L \times const_{InL}.}{In\ L \times const._{InL} + Ga\ L \times const._{GaL} + As\ L \times const._{AsL} + O\ K\ \times const._{O} + Pt\ M \times const._{Pt} + Si\ K \times const._{Si}} \tag{6.2}$$

$$const_i = k_i \times abs_i \div A_i$$

Where

I: X-ray map intensity (original image file, after correction for tiff-conversion);

B: background intensity;

k: k-factor with respect to *Si K* line;

A: Atomic weight;

abs: absorption (assuming abs_{SiK} =1).

In order to extract the In signal from the background noise, we add all 7 maps of the partial in L-line (the generated original images from the images in tiff format). The produced In map has an intensity of 14.35 at the top of the island, an average intensity of 9 at the bottom the GaAs substrate and an average intensity of 11 at the top coating platinum layer, as shown below in figure 6-20(a). There is a belt shaped SiO_2 layer between the islands and the top coating layer, which produces a weak X-ray signal. In fact, In should not be detected at either the top coating layer or in the substrate, which means the signals outside the island are all background noise. The In map has a low and varying signal-to-noise ratio at different regions, therefore, we cannot substract a constant value from the In map to remove the background noise. The map of stray Cu x-rays is used to solve this problem, as Cu is not existing in this sample at all. Cu_K map is used to model the background noise, as Cu_K has a signal distribution similar to the In background noise as shown in figure 6-20(b). We aim to remove

the background noise as much as possible and avoid generating negative counts. First, we apply a median filter with window size of 3 to the Cu_K map to smooth it. Then the smoothed map is multiplied by a factor of 0.215. This value is chosen to transfer the Cu_K map into a noise-free estimator of the background In map, which has an intensity of 9.9 at the coating layer and an intensity of 7.9 at the bottom substrate. After substracting the modifed Cu_K map from the In L map, we successfully produce a background-corrected In map, which has less impact from the background and a higher signal-to-noise ratio.

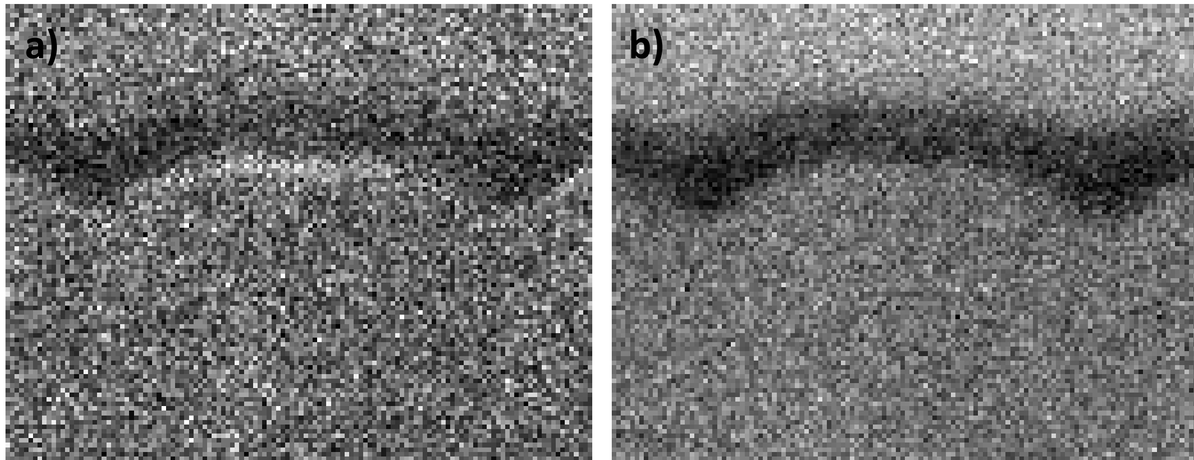

Figure 6-20 (a) All InL maps added up together, which shows a strong In signal at the top of the island but a low signal-to-noise ratio. (b) Cu_K map has a similar signal distribution. It could be used to estimate the background in In mapping.

For the other elements, the signal-to-noise ratio (SNR) varied over a large range as shown in the X-ray spectrum in figure 6-19. For example, AsKa has a strong peak in spectrum with a high SNR ratio of 50, but PtLa has a weaker spectrum intensity with a rather low SNR of 5. For each element, the intensity of the backgound noise is directly measured from the X-ray map by integrating the line profile function across the map in vertical direction. For instance, we subtract an intensity of 2.08 from GaLα map before modifying the map with k-factor, absorption and atomic weight (three values are converted into in one constant to make the further calculation easier, as shown in table 6-6). Then we obtain the GaLα map with repect to L line, without background noise. It is saved in .dm3 format, which can be used straight away by Digital Micrograph in later calculations.

In L with respect to Si K line			
Element	k factor	Atomic Weight	Constant $_i$
C K	1.934	12.011	0.161
O K	1.853	15.999	0.116
Si K	1	28.086	0.036
Ga Lα	1.654	69.723	0.024
As Lα	1.822	74.922	0.024
In L	1.822	114.82	0.016
Pt Mα	2.652	195.08	0.014
Pt Mβ	2.652	195.08	0.014

Table 6-5 k-factors with respect to SiK line and atomic weight from ISiS calibration.

All lines (In_L, Ga_L, As_L, Pt_L, Si_K, C_K and O_K) are aprocessed as described above and the resulting maps are substituted into the equation for the of In composition. The resulting In_L concentration map is shown in figure 6-21. There is a clear In rich region in the top of islands. A line profile across the map shows the highest concentration is about 8.5%. Due to this being mainly InGaAs, by assuming Pt, Si and O have a composition close zero, as shown in following equation, the actual In concentration from all elements is $In_{0.26}Ga_{0.74}As$, which is twice as high as from the plot 6-21(b).

$$\frac{I_{In}^{*}}{I_{In}^{*}+(1-x_{In})I_{Ga}^{*}+I_{As}^{*}+0_{Pt}+0_{Si}+0_{C}+0_{O}} = \frac{x_{In}}{2} \qquad \text{when} \qquad I^{*} = I * const_i$$

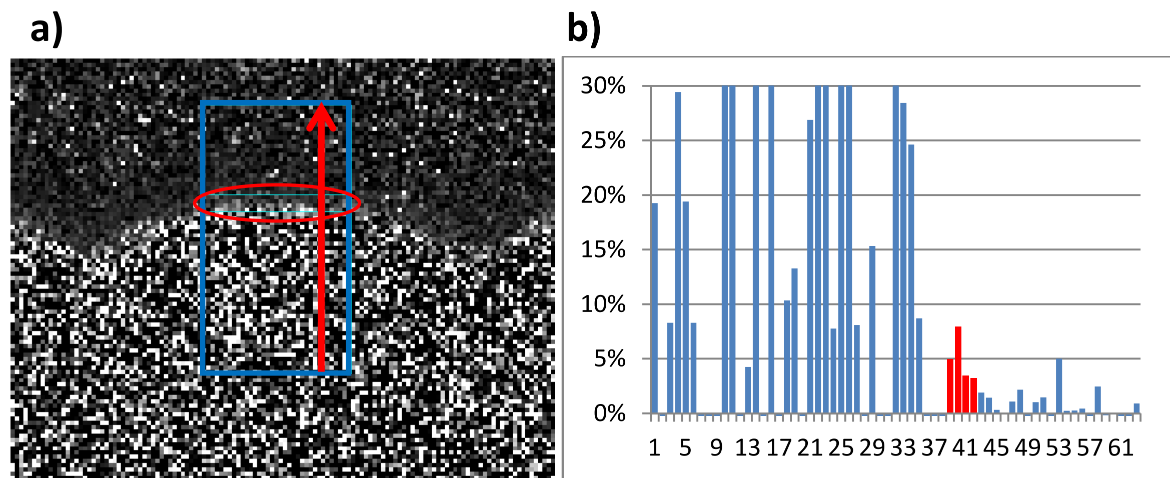

Figure 6-21 TEM cross-sectional analysis of a single island with a sampling size of ~2nm. (a) In concentration map from L line of all elements. (b) the circled In concentration line profile at the top of the island is ~8.5%, which means the chemical composition is $In_{0.17}Ga_{0.83}As$.

To verify this result, we repeated the analysis proceduce by estimating the In composition using the K lines of Ga and As as reference, which is supposed to have a similar outcom. The chosen elements are changed to In_L, Ga_K, As_K, Pt_L, Si_K, C_K and O_K as shown in equation (6.3).

$$\frac{x_{In}^{K}}{2} = \frac{In\ L \times const._{In}}{In\ K \times const._{In} + Ga\ K \times const._{GaK} + As\ K \times const._{AsK} + O\ K\ \times const._{O} + Pt\ L \times const._{Pt} + Si\ K \times const._{Si}} \quad (6.3)$$

The resulting In composition line profile yields a peak of 11% from all elements which means the apparent In concentration is $In_{0.22}Ga_{0.78}As$. Another way to estimate the result is to estimate the In composition by assuming all elements other than In, Ga and As can be ignored in equation (6.2) and (6.3).

The substituted EDX maps all have background removed. The calculations yield data close to each other, which means the result is reliable. There are eight ways from different combinations of k and L lines to calculate the In composition, as shown below. Also, the In composition measured from EDX analysis, 0.155±0.031, is close to previous micro-photoluminescence result. The small difference may be explained by the inhomogeneous In distribution inside the formed island, which has a higher In concentration at the centre of the island.

The resulting In	As	Ga	$In_xGa_{1-x}As$
L	L	L	0.18
L	L	K	0.16
L	L		0.20
L		L	0.16
L	K	L	0.16
L	K		0.16
L		K	0.11
L	K	K	0.11

Table 6-6 Eight combinations to estimate the In composition from only Ga, As and In by ignoring Si, C, O and Pt. The calculations show data close to each other, which means this result is reliable. The mean from above data is 0.155±0.031.

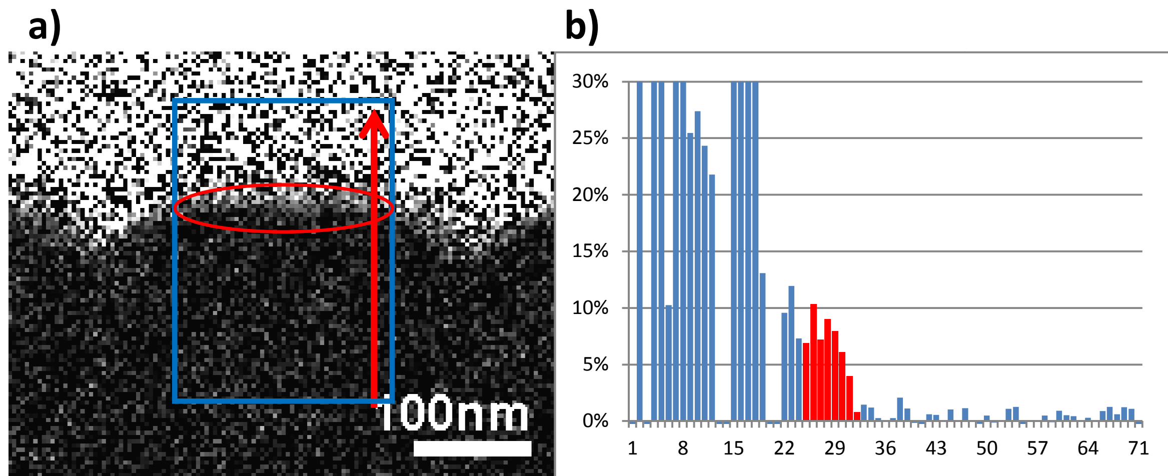

Figure 6-22 TEM cross-sectional analyses of single island with a sampling size of ~2nm. (a) In concentration map with respect to L lines (InL over GaL+AsL+InL). (b) the circled In concentration line profile at the top of the island is ~9%, which means the chemical composition is $In_{0.18}Ga_{0.82}As$, which is close to the PL result $In_{0.26}Ga_{0.74}As$.

6.3. Overgrowth of 3rd wafer

The 3rd wafer has been planned to calibrate and support the data and result from the 2nd wafer. Data includes the relationship between the dimension of the islands and patterning parameter and the chemical composition. For this wafer, we have different wetting layer thicknesses across the wafer to study its influence on quantum dots overgrowth on the patterned substrate. A thinner wetting layer is expecting to produce smaller islands with better opto-electronic properties [64]. Also, the overgrowth on patterned substrate is improved by using In-assisted desorption of the native surface oxide, which results in a clear and smooth surface [65]. The analysis procedure is similar to that of the 2nd wafer. SEM and AFM images are the major examining tools.

6.3.1. Improved wafer layout and pattern design and overgrowth

To deposit different thicknesses of InAs across one substrate, the best way is to switch off the wafer rotation during overgrowth stage and position a series of patterns in a row pointing away from the gas source, as shown in figure 6-23. This design will produce an InAs

thickness gradient along the direction of the In flux. The region far away from the cell will have a thinner InAs thickness than the region close to the gas source.

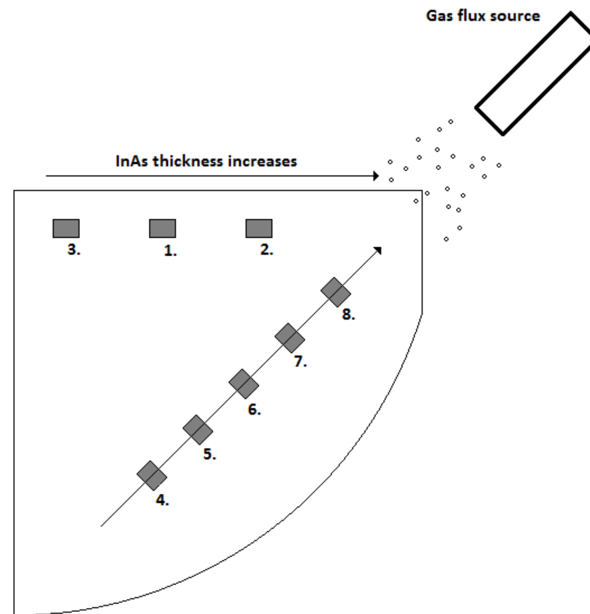

Figure 6-23 The layout of the 3rd wafer. The top right corner has the shortest distance to the gas source and the left bottom corner has the longest distance. The InAs thickness deposited has a gradient as shown. Each dark box is a patterned region with size of 250µmx200µm.

To make later investigation easier in the FIB, we used a quarter of a 2-inch wafer instead of a whole 2-inch wafer, as shown in figure 6-23. Eight patterned regions have been marked with numbers. The patterns are placed away from the edges where the heater has contact with the wafer, to avoid area of possibly non-uniform heating. To save space, the patterned regions have to be close together. However, we have a new high density pattern design, which will make the investigation process quicker and more convenient. The distance between the patterns in groups 4-8 is 2.5mm and between the patterns in groups 1-3 is 5mm.

The ion beam parameters involved cover a narrower range compared with previous experiments. Based on the data collected from the last wafer, we will only focus on the parameters that will consistently produce island structures. The patterns made by the high ion dose that produced rings and holes but not islands are omitted. Also, the patterns with pitch sizes larger than 500nm have been removed, because their false positive and false negative deposition results are undesirable. The ion beam parameters selected for patterning are listed in table 6-7.

accelerating voltage [keV]	probe current [pA]	dwell time [ms]	pitch [nm]
20	1.5	1	200
30	4	5	250
``	40	25	500
``	``	125	``

Table 6-7 Ion beam patterning parameters for 3rd wafer. The range of ion beam patterning parameters has been narrowed, in order to focus on parameters which can consistently produce island structures.

Even though the 2nd wafer produced a significant amount of useful data, there were quite a lot of patterns which, due to the elongated beam shape, did not produce a useful result. We spent a lot of time to investigate the problem, tune and test the ion optics column alignment before moving to the next patterning and growth. The final conclusion has been that the attenuation box on the FIB has some problem. The attenuation box is a device connecting the Orsay Physics system and the Raith patterning system. Noises are introduced when the deflection signal is transferred from the Raith software to the octupole. The noise wobbles the ion beam over a short distance, which results in an elongated dot. The wobbling distance is linearly increasing with increasing scan field. There is nothing we can do, unless we are willing to disassemble the box or look into the software code. However, we decided to reduce the effect from this problem as much as possible by patterning smaller fields (6.5µm x 6.5µm). All the parameters were redesigned so they could all be varied within one patterned region. Each patterned region is marked as a dark box in figure 6-23. The size of the double-cross structure shown at the top of figure 6-24 was 110µm x 50µm, which makes finding the patterned regions under an optical microscope much easier. There are 6 patterned areas surrounding the crosses. Each patterned area has a dimension of 40µm x 40µm, and is consisting of a code at the top and twelve 10µm x 10µm boxes, as shown in the lower part of figure 6-24. There is a 6.5µm x 6.5µm patterned array in each box. The code at the top records the accelerating voltage and aperture used to make each pattern. The dwelling time was increased in a row from left to right and the pitch from top to bottom. The exact values of dwell time and pitch are shown in table 6-7.

When the pattern was fabricated in practice, unfortunately, the ion beam alignment showed some elongation after a few patterns had been milled. We have also included an e-beam

patterned region next to region 6 which is not shown in figure 6-23. From wafer 2, it had become clear that areas having been e-beam scanned had interesting overgrowth result, with larger islands and less wetting layer. We thus tested if e-beam nano-patterning could affect the Stranski-Krastanow growth.

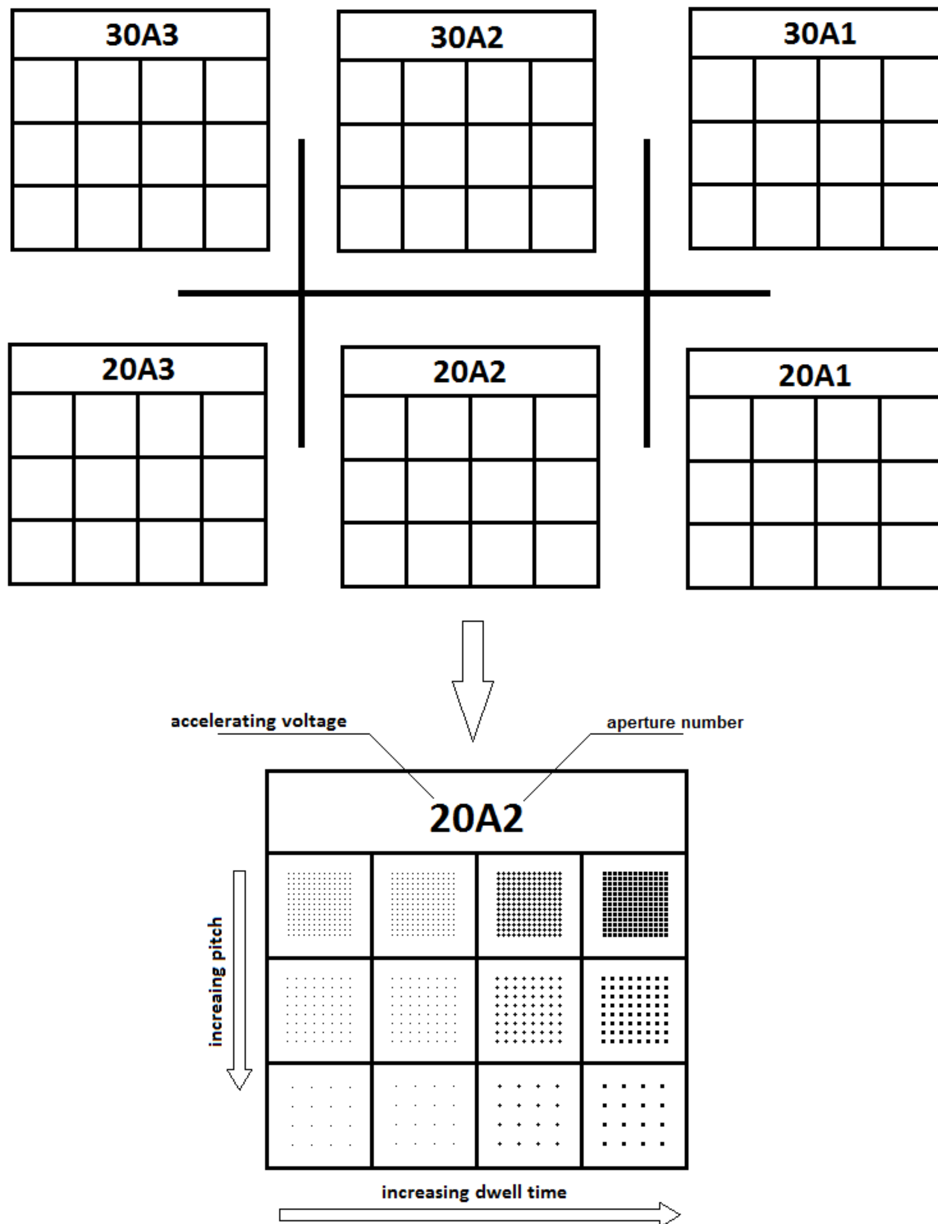

Figure 6-24 The schematic diagram of the patterned regions and each individual pattern.

The overgrowth started with degasing the wafer in the preparation chamber of the MBE system overnight. The degas process took 8 hours to remove contamination, such as water, carbon by monitoring the pressure of the preparation chamber. The degas temperature was about 150°C. Then the wafer was transferred into the MBE growth chamber and annealed

under In flux instead of standard As overpressure. This new technique can desorb the surface oxides at low substrate temperature [65]. This alternative technique reduces the surface roughness compared with the standard annealing in As overpressure, which should in turn increase the difference between the patterned area and the un-patterned area. The annealing environment was about 520°C with an In flux of 0.02ML/s. The annealing lasted for 8 minutes at 1.26×10^{-8} mbar pressure inside the growth chamber. Then the grown indium layer was removed by increasing the sample temperature to 560°C and annealing for another 5 minutes. Regarding to the RHEED pattern during the whole grown process, the RHEED started with dim dots, because of the existing surface oxide. After the oxide was removed, we had brighter dots in the RHEED pattern. When the temperature was increased to remove the In layer formed, where the streaks in the RHEED patterns started to appear. The annealing was stopped when some brighter streaks were visible, which means the substrate probably had an In free, reconstructed (2x4) and flat surface. The temperature was then reduced back to 520°C, before moving to overgrowth. A 20nm GaAs buffer layer was grown with a speed of 0.313Å/s, which took twice 5 minutes separately with a 3 minutes break applied to smooth the surface, then another 5 minutes growth proceeded. We stopped the wafer rotation here, in order to get a slope of InAs thickness across the wafer, although we noticed the size of the wafer might be too small to have a significant slope at all. Finally, normally 1.6ML of InAs was grown at 0.02ML/s for 80 seconds at 520°C. This is very close to the SK transition, probably just below, so that no QDs should form on the unpatterned surfaces not treated previously by FIB patterning.

6.3.2. Results

We first tried to verify if the ion beam patterning parameter in the chosen range had produced only islands, without producing any rings or holes. Overview images of the patterned regions from 4-8 are captured by SEM secondary electron imaging, as shown in figure 6-28. Part of the patterns suffers from ion beam misalignment, which is not included as valid data points in figures 6-25 and 6-26.

The success rate of each array is estimated as the total number of islands formed at the patterned sites over the total number of the patterned sites. The ion dose is equal to probe current multiplied by dwell time. Only data collected from the patterns with a pitch of 500nm are included in figure 6-25 and figure 6-26, as the islands formed on the patterns with pitches of 250nm and 200nm were too close to each other, which made the counting and statistical analysis difficult and unreliable. Most of the arrays have a success rate in range between 90% and 100%, and there is some overlap of the data points in this range. The data are presented in two groups for the different accelerating voltages of 20kV and 30kV.

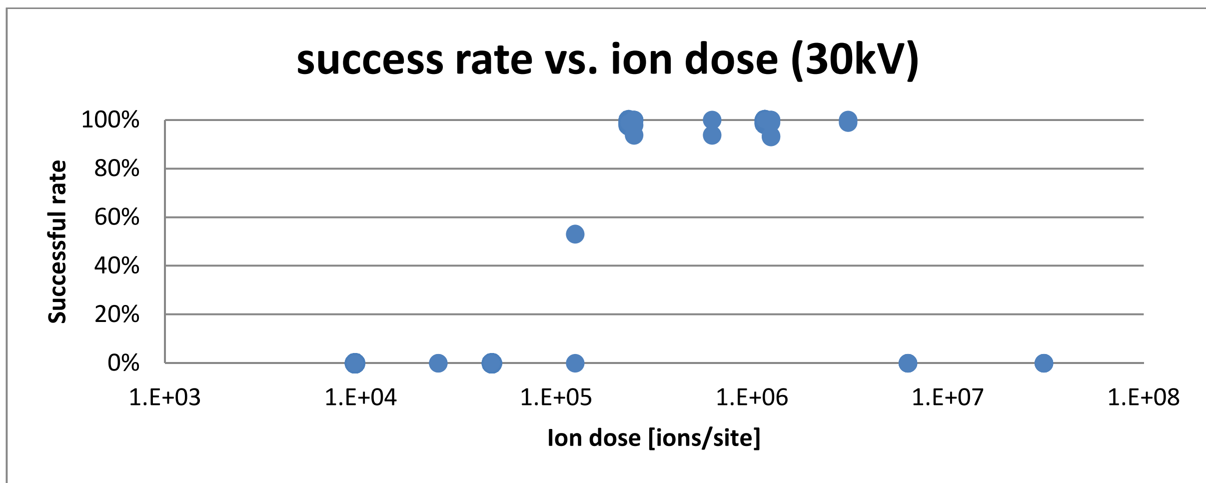

Figure 6-25 Success rate of QD nucleation at pre-patterned sites vs. ion dose (accelerating voltage of 30V).

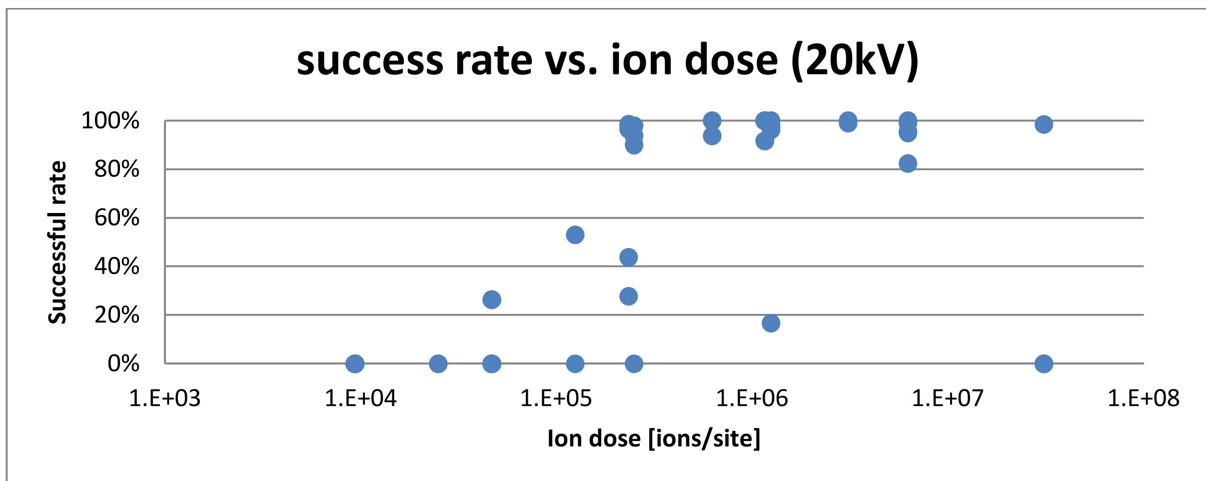

Figure 6-26 Success rate of QD nucleation of pre-patterned sites vs. ion dose (accelerating voltage of 20kV).

Figure 6-25 and figure 6-26 show that the islands are more likely to form when the patterned site has an ion dose in the range of $1x10^5$~$6x10^6$ ions/site. The patterns fabricated with a 20kV accelerating voltage have a slightly wider range of ion dose for effective QD nucleation,

which is extended up to 1x10^7 ions/site. Combining this data with the result from 2nd wafer as shown in figure 6-12, we have the ideal range of the ion dose and dwell time. The ideal ranges in both experiments agree with each other and there is barely any island nucleation over the patterns with ion dose <10^{7}ions/site.

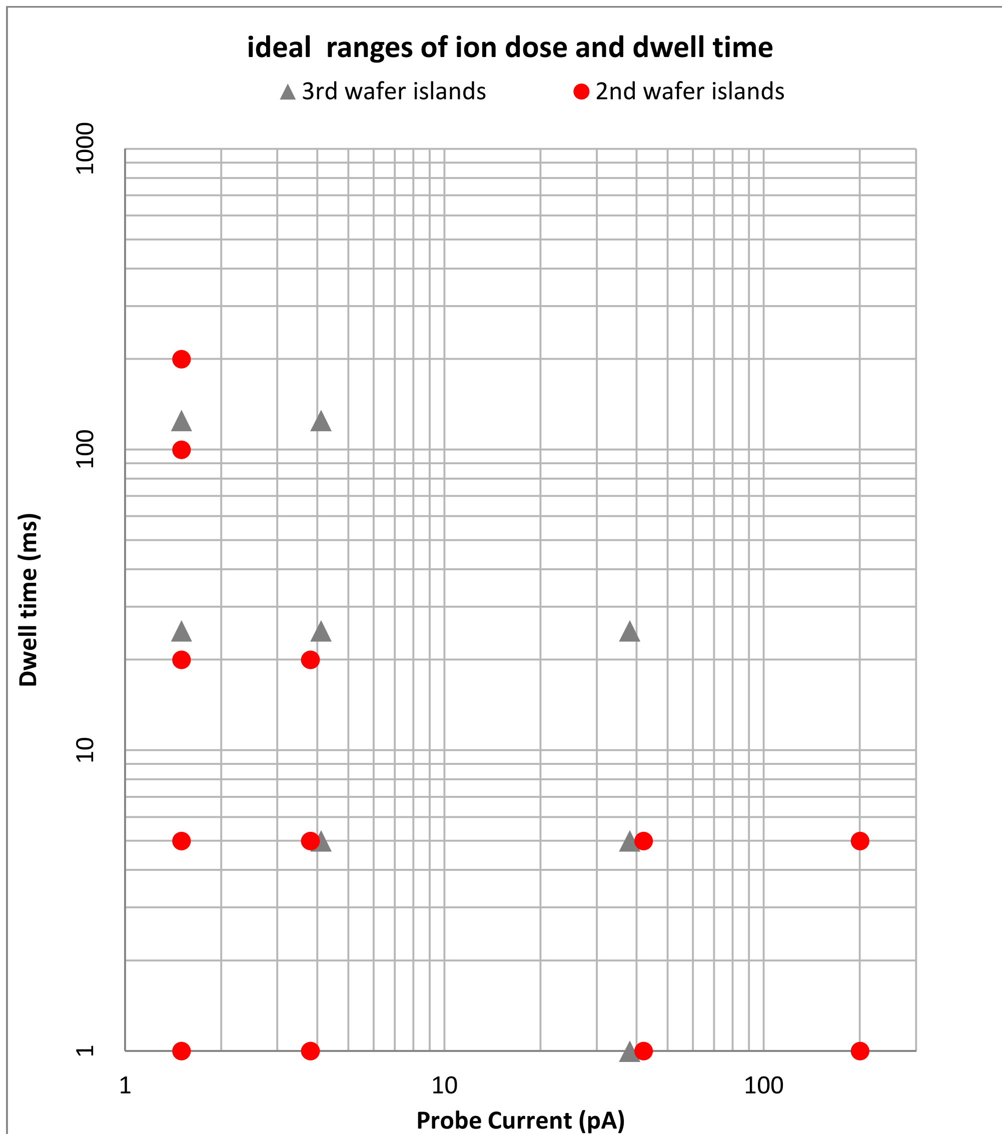

Figure 6-27 Comparing the influence of ion dose from 2nd wafer (dot) and 3rd wafer (triangle). The ideal ranges for the two wafers roughly agree with each other. However, as the range of the ion patterning parameter has been narrowed, there are data points in the bottom left corner from the 3rd wafer.

We are interested in finding out whether there is any influence from the InAs thickness. Some SEM secondary electron images have been captured to gain an overview of the grown structures and help finding interesting areas for which, similar to the 2nd wafer, the diameter and the height data could be collected by AFM in tapping mode.

Figure 6-28 shows two groups of secondary electron images. Each column contains patterns made by the same ion beam parameters but located at different regions, as shown in figure 6-23. The left group has been generated with 20kV accelerating voltage, 40pA probe current and 25ms dwell time at a pitch of 250nm; the right group with ion beam of 30kV accelerating voltage, 40pA probe current and 5ms dwell time at a pitch of 500nm. The figure shows that the patterns located at region 4, which was the longest distance from the gas source, do not show much growth. Also, regions 7 and 8 show more obvious island nucleation than regions 5 and 6. However, island size data from SEM images do not show clear evidence that the islands located at region 7 and 8 have larger diameters than the islands located at regions 5 and 6.

Regarding the change of InAs thickness across the wafer, we cannot estimate exactly the gradient, but can only confirm the tendency to form islands is increasing from region 4 to region 8. However, the relationship between the InAs thickness and the geometry of the islands is not established yet. It will be very difficult to reveal the connection between the InAs thickness and the size of the islands, because the average nominal thickness is only 1.6ML, which means the difference of the thickness is <0.1ML over the distance of 10mm. The SE images show that the deposited InAs close to the patterned sites forms islands inside pits. The secondary electron image has a strong contrast from the InAs islands and InAs wetting layer, compared to the substrate near the islands which may indicate pure some GaAs exposure under the InAs wetting layer coverage. The higher secondary electron intensity at the islands confirms the islands have a higher In composition.

Another interesting result is the shape of the islands. The left group of islands has a faceted shape, with elongation along $[\bar{1}10]$ direction. This elongation can only partly be the result of a stigmatic ion beam, similar to what was observed for the previous two wafers. However, there is another possible explanation by M. Rosini and C. Righi [66], who found that In diffusion on 2x4 GaAs reconstructed surface (alpha2 and beta2) is highly anisotropic. The diffusivity is higher in the $[\bar{1}10]$ direction than [110] direction. This phenomenon would be more obvious when the growth temperature is low, because then it is harder for the In adatoms to overcome the energy barrier for diffusion. Also, it is more likely to happen if the islands are In rich and have a large diameter, which is exactly what we see on this wafer.

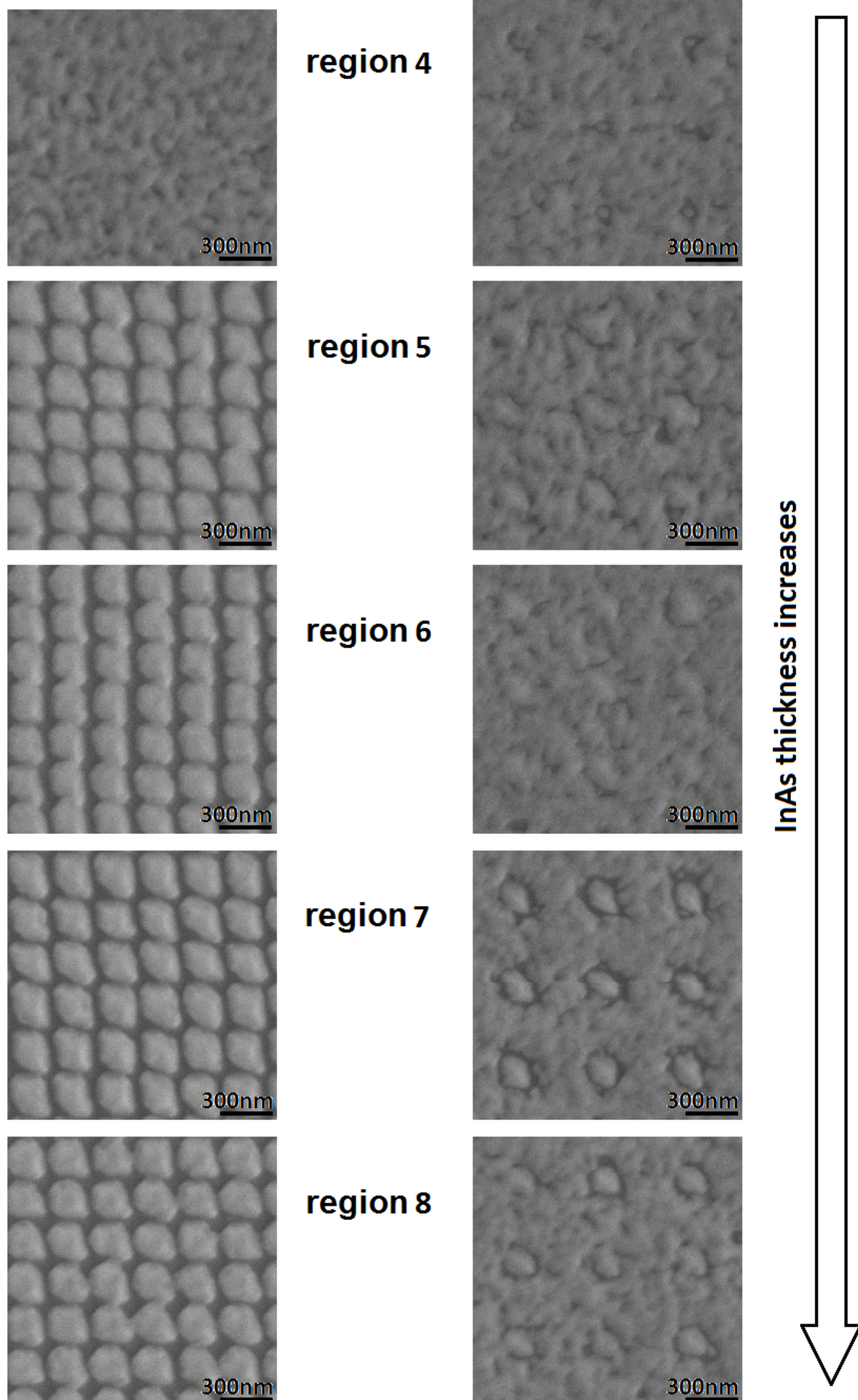

Figure 6-28 Islands formed in different regions, which have different distances from the gas source. From bottom to top, region 8 is the region closest to the gas source and region 4 is the one further away. The distance decreases from top to bottom, thus the InAs thickness increases.

AFM images have been captured to gather more accurate data about the heights and diameters of these islands and to investigate the relationship between the geometry of the islands and the InAs thickness. The AFM images have a size of 4µm x 4µm with 512x512 pixels (sampling of 7.8nm/pixel), which is good enough to resolve the ~100nm diameter islands. Such an AFM image is shown in figure 6-29. This is an area patterned with 20kV accelerating voltage, 1.5pA probe current and 125ms dwell time, at a pitch of 500nm. This image demonstrates how height and diameter are measured. We try to predict the dimension of the islands formed for known ion beam parameter. Based on figure 6-14, the predicted height should be ~20nm and the diameter should be 150-175nm. We have not used exactly the same patterning parameters as for wafer 2, but there are estimated values.

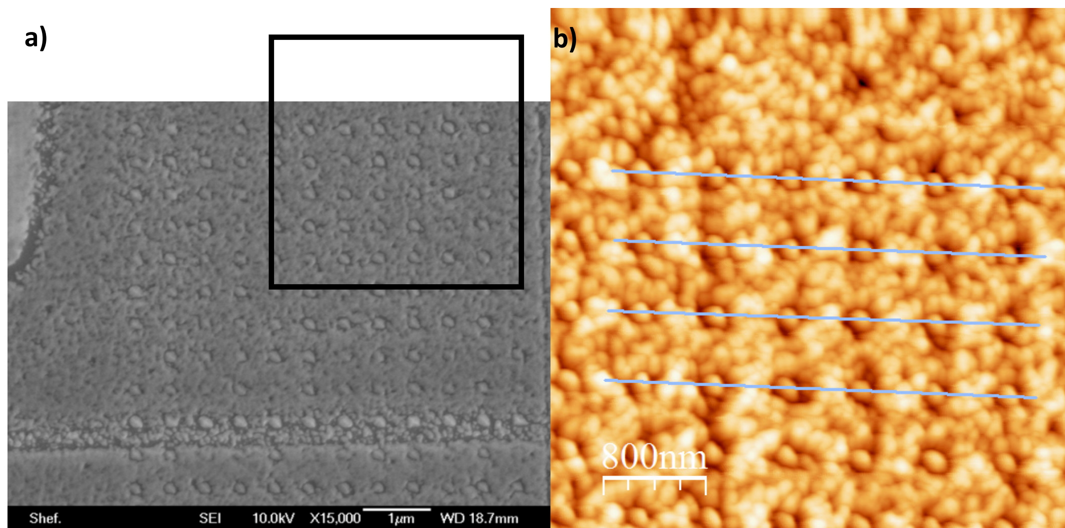

Figure 6-29 (a) The AFM investigated area is shown as the boxed area in the SEM secondary electron image. (b) The height and diameter data are gathered by taking four line profiles measured across the formed islands, as shown in the AFM image.

To evaluate the height and diameter of the islands, multiple line profiles are measured across the AFM images, as shown in figure 6-29b. The line profiles are averaged over multiple line scans to produce more accurate data and reduce the effect from surface roughness. Similar to the previous AFM analysis, the height is measured from background to peak and the diameter is measured as full width at half maximum. Four individual line profiles and their average are shown in figure 6-29a. The resulting height from AFM is 13.0±1.9nm and the diameter is 119.5±6.1nm. Both the height and the diameter are smaller than expected from wafer 2, which demonstrates that islands from wafer 3 are slightly smaller than from wafer 2, which may be explained by the lower InAs thickness deposited. The averaged line profile reveals

the islands are sitting in pits rather than having nucleated above the wetting layer. This might be the result of the different annealing technique used, or of a lower annealing temperature.

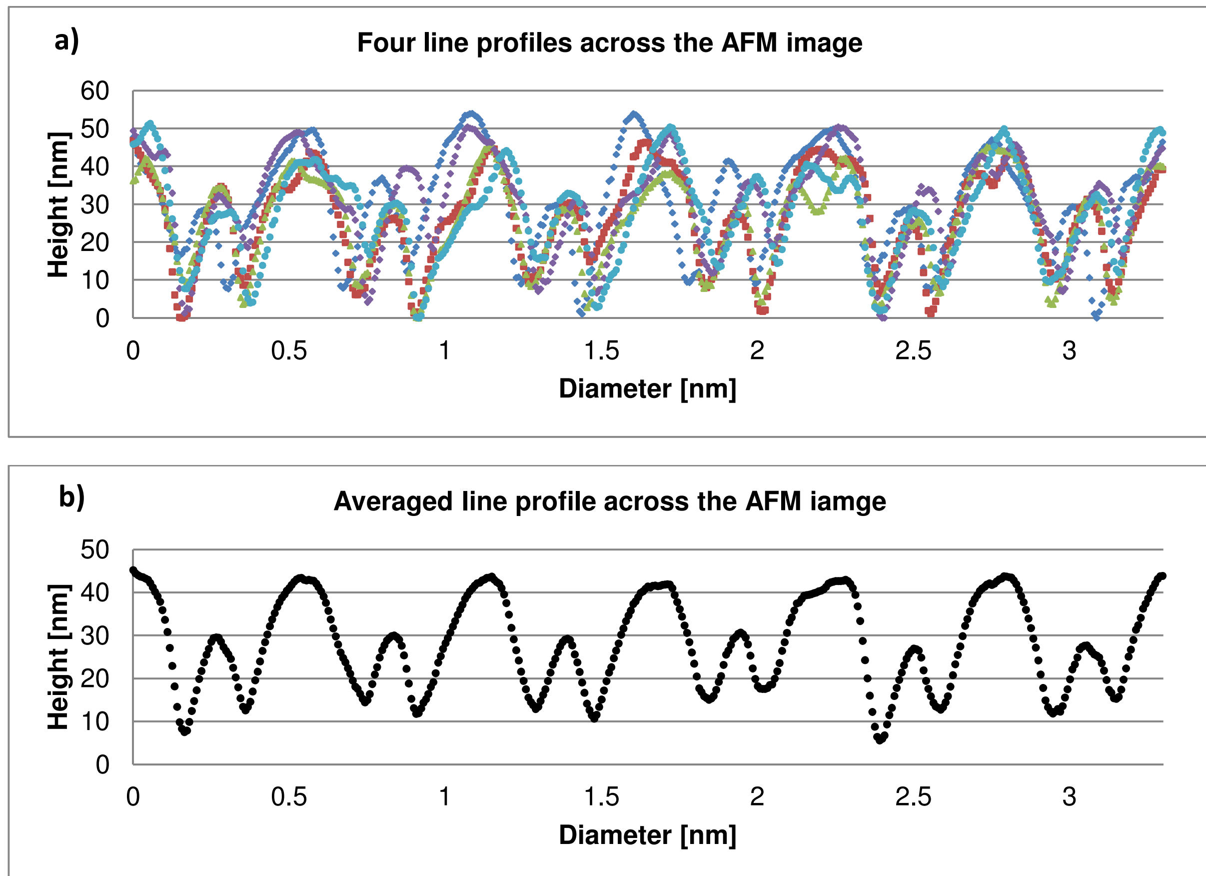

Figure 6-30 The four line profiles across four rows of islands as shown in figure 6-29 and the average line profile generated from them, which will be used to estimate the height and diameter.

The results from measuring two groups of nucleated islands are shown in table 6-8. The two sets of ion beam patterning parameters are chosen to compare islands formed over the patterns fabricated with the same accelerating voltage and similar ion dose, but different combinations of probe current and dwell time. These two sets show two different results: the higher probe current but shorter dwell time leads to wider islands; while the low probe current with longer dwell time yields smaller island sizes. To confirm this result, the thickness of the InAs wetting layer is estimated at different regions by flattening the island formed inside the pits. The volume of the island is calculated by equation shown below. The nominal thickness of the deposited InAs is 0.5nm, which is thinner than the estimated thickness of InAs. This can be explained as the islands are $In_xGa_{1-x}As$ instead of InAs similar to the 2nd wafer where the estimated In composition is between 0.10 to 0.25. The result shown in table 6-8 points out the patterns fabricated with high probe current and short dwell

time can attract more InAs to nucleate islands compared to patterns fabricated with lower probe current but longer dwell time.

(6.4)

(6.5)

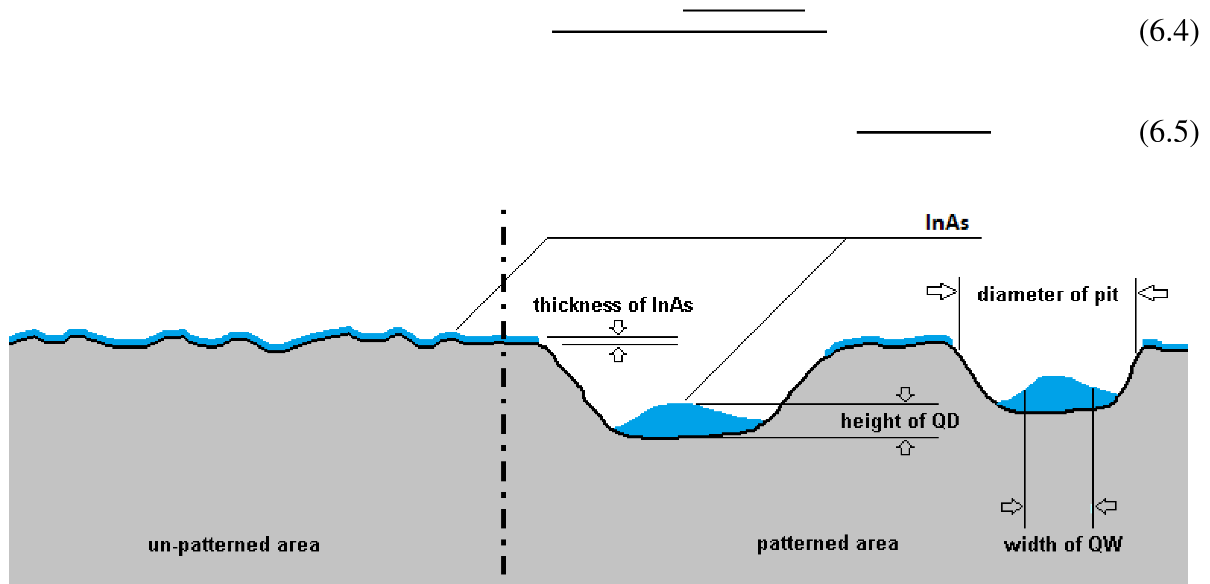

Figure 6-31 The fabricated patterns attract nearby InAs to form islands at the bottom of the patterned pit, in contrast to the unpatterned area, which only has a wetting layer.

20kV, 40pA, 5ms, 500nm

location	QD height [nm]	QD diameter [nm]	island volume $[nm^3]$	diameter of pit [nm]	thickness of InAs [nm]
region 4	n/a	n/a	n/a	n/a	n/a
region 5	14.5	244.2	339160	454	2.1
region 6	15.3	235.5	333565	422	2.4
region 7	14.6	210.3	252718	398	2
region 8	10.8	189.7	152962	431	1.1

20kV, 1.5pA, 125ms, 500nm

location	QD height [nm]	QD diameter [nm]	island volume $[nm^3]$	diameter of pit [nm]	thickness of InAs [nm]
region 4	12.1	107.3	54781	397	0.4
region 5	13	119.5	72728	452	0.5
region 6	n/a	n/a	n/a	n/a	n/a
region 7	14.1	111.2	68495	364	0.7
region 8	12.8	136.3	93220	432	0.6

Table 6-8 The height and diameter of islands formed in different regions with similar ion dose. The volume of the islands is estimated from equation (6.4). Two data points are missing as no islands have been observed (40pA, 5ms, region 4) or the formed islands had a too elongated shape (1.5pA, 125ms, region 6).

By comparing the result from overgrowth of all three patterned wafers, we can conclude that the influence from the thickness of the InAs is as follows: quantum dots formed on the 1st wafer almost everywhere, because the 1st wafer had a thicker InAs deposit (2ML). The

islands formed had a slightly higher density inside the patterned regions and closer to the edge of the patterned holes than in the unpatterned area. The islands on the 2nd wafer had a clearer preference for formation at the ion beam patterned areas. We have successfully produced island nucleation only at the patterned sites but nowhere else. The $In_xAs_{1-x}Ga$ islands have a lower In concentration around 0.16-0.22 but too large sizes to produce strong and sharp PL signals. This 3rd wafer had a similar result regarding the island nucleation at the patterned sites, which documents good reproductively for 1.6ML InAs deposition.

Chapter 7. Conclusion

We have done a series of experiments covering a wide range of the application of FIB, from basic imaging and the standard TEM cross-sectional sample preparation to some advanced projects, such as TEM aperture micro-machining and wafer nano-patterning. I'd like to summarize the major results in this chapter and include some outlook onto possible further research.

7.1. Summary of the main results

From comparing three types of resolution measurement for SEM, we have found that the measurement of dark space resolution down to about 5nm in our instrument, yields the best resolution result, compared to the apparent resolution of 14nm and 30nm from the measurement of power spectrum and line spread function. This is probably the reason why it is the most widely used resolution measurement technique in SEM and preferred by all manufactures. The orientation of the sample with respect to the position of the SE detector significantly influences the outcome of all techniques. When the sample is facing away from the detector, the captured image has clearly a better resolution than when the sample faces towards the detector. Because the secondary electron escaped from the sidewall of the edge can not hit the detector, which results in a shaper contrast difference. Regarding the measurement of ion beam size in FIB, it is technically more difficult and the measured resolution is worse than the real resolution. The best resolution at 30keV ion energy is 20nm with a probe current of 1.7pA, which is the lowest probe current we have. The inherent characteristic of ion beam imaging, i.e. ion beam sputtering, is influencing the imaging process. The scanning ion beam destroys/mills small gold particles and flattens sharp edges, which all directly worsens the result of measurement. The measured ion beam size helped later micro-machining projects by revealing the resolution limitation by machining, as features to be milled cannot be smaller than the image resolution. Principally, the resolution will be better if the accelerating voltage is reduced (5kV); however, the signal-to-noise ratio of the ion beam image will decrease, which makes aligning the ion beam column and precisely selecting the area to be milled more difficult.

Both TEM cross-sectional sample preparation and TEM aperture fabrication demonstrate the FIB micro-machining functionality. We have presented the complete procedure of an in-situ lift-out, including the operation of the gas injection system and the nano-manipulators. Some typical problems have been discussed with the corresponding solution. A few techniques about how to handle an insulating sample and avoid charging effects were introduced. E-beam deposition had been applied for the lift-out sample containing sensitive surfaces, such as the uncoated quantum dots. During the fabrication of the TEM apertures, we have removed a relatively large amount of material within a reasonable time. The milling speed and quality are increased by polishing off the top rough and hard oxide layer on Al samples. The difference between FIB milling an oxidized Al foil and a polished Al foil are show. The most obvious differences are higher sputtering yield and better quality of the fabricated trenches. By measuring eight square boxes with a length designed to be 13.5µm x 13.5µm, we got an average length of 13.49±0.48µm, which is a very good result. The slope of the side wall through a foil of thickness of 5.25µm is 4.25°. This is also a good example to demonstrate how a real problem can be solved by FIB micro-machining in practice.

The study of the InGaAs quantum dots nucleated on FIB patterned GaAs (100) substrates has been fairly successful. The results can be summarized by answering two questions: how to fabricate QDs over patterned substrates and how the patterning parameters influence the resulting QDs. To have quantum dots consistently nucleate only at the patterned sites but nowhere else, the two key effective factors are the thickness of InAs deposited and the ion dose at each individual patterned site. The ideal thickness of InAs deposited is slightly smaller than the critical thickness typically quoted for the In(Ga)As/GaAs quantum dot SK growth, which is 1.8ML [25]. We have shown formation of islands after 1.6ML InAs has been deposited on the 3rd wafer, which gave islands with a diameter of ~100nm. We guess an InAs thickness of 1.5ML or even 1.4ML can still produce islands at patterned sites, however, due to time constraint, we had no chance to test this in detail. It would be interesting to grow InAs with different thicknesses across a large patterned wafer, in order to evaluate the thickness for SK growth on a FIB patterned substrate. The other key factor, the ion dose per patterned site, has a visible influence on the pattern fabricated. We found island structures only appeared for patterns which are produced with ion dose within the range of $1x10^5$~$6x10^6$ ions/site and resulting shallow pits. With increasing ion dose, the ion beam first produces hillocks, then shallow pits and finally deep holes in the substrate and these different

structures result in different overgrowth results. The growth on a patterned substrate is influenced by the surface geometry, probably mainly steps and kinks. It is worth mentioning that the ion dose is the product of two ion beam parameters, the dwell time and the probe current. Patterns fabricated by a long dwell time and a small probe current can receive the same ion dose as patterns fabricated by a short dwell time but a large probe current, both of which results in islands formed but of different sizes, perhaps due to the large probe current implying a larger beam spread and producing a larger damaged area. The patterning ion beam parameters and the pitch of the array have strong influence on the size of the islands formed. As described for the 2nd wafer, the island heights are almost constant, covering a narrow range from 12nm to 25nm, with values slightly increasing with pitch. The diameter scales with the square root of the pitch and is also increasing with the dwell time and probe current, but not very strongly. For the 3rd wafer, which used different ion beam patterning parameters combined with a thickness change of the InAs, it is hard to tell the reason for the change in island size. In the micro-PL measurement of the 2nd wafer, we observed two rather broad peaks at ~878nm (1.41eV) and ~1152nm (1.08eV), which are from the underlying GaAs substrate signal and the InGaAs QD signal. From the latter peak wavelength we can estimate the compositional ratio of Ga:In atoms as 74:26 (i.e. $In_{0.26}Ga_{0.74}As$). The estimated In concentration is higher than the result of EDX analysis, which is 0.17. This composition difference could be caused by uniform In distribution inside the islands formed. By analysing the relation between the thickness of InAs deposited and the size of the fabricated QDs, we estimated for the 3rd wafer that the In composition inside the islands were 0.22±0.13, which had the similar size to the 2nd wafer. The fabricated regular QD are reportable with reasonable consistence and success ratio, which has been proven from 2nd wafer and 3rd wafer. But for application, the diameter is too high and In composition is too low, which still need some optimization and further study.

Regarding my personal skills, I have gained a lot of experience from using different instruments and equipment during the last few years, in both fabrication and investigation. We used FIB and MBE to pattern the substrates and overgrow them; AFM and SEM were used to collect topography information on the nucleated QDs; micro-PL and STEM-EDX analysis were performed to estimate the opto-electronic property and the chemical composition, respectively. This project provided me with a good opportunity to learn how to operate different equipment and use different lab techniques. However, a complicated

experimental project also means it can seriously suffer from machine downtime, which happened quite a few times during this project. While analysing the influence from the multiple ion beam parameters, this project involved a lot of statistical data analysis and gave me valuable experience about how to systematically extract useful information from a large and complicated data set.

7.2. Outlook for further study and research

Because of limitations of our FIB system, we do not have the opportunity to use low voltage (<10kV) ion beam to polish TEM membranes, in order to produce really thin (<30nm) samples without amorphous layer for high-resolution TEM. Regarding micro-machining, 3D-nanotomography 'slice and view' could be the next major application of FIB; especially as the technology of detecting various of signals has become mature in the last a few years. For microstructure analysis, electron backscatter defection imaging (EBSD) and secondary electron image (SE) could be installed; energy-dispersive X-ray spectroscopy (EDX), wavelength-dispersive X-ray spectroscopy (WDX) or mass spectroscopy (MS) could be useful to collect chemical information. The 10-100nm voxel resolution of FIB 3D-nanotomography has successfully filled the voxel resolution gap of 3D tomography technology between the light tomography (coarser) and TEM or X-ray tomography (finer) [67]. Application of electron beam and ion beam deposition is an interesting topic, which can be directly used to build 3D structures, such as nano-tools [68], nanotubes or electronic circuits. The fabricated coded aperture has not been used yet for diffractive imaging and in the TEM. It will be more complicated to produce a diffractive image with a coded aperture than a standard bright-field image, as we would have to decode the signal [34]. To produce a coded aperture containing more than 21x21 pixels with the existing FIB can be a challenge. The difficulty is increasing with the volume of the material that needs to be removed and is also related to distortions when scanning a larger field.

The study of the quantum dots nucleated on the patterned substrate is not complete yet. After knowing how to consistently produce regular quantum dot arrays on the patterned substrate, a further study could investigate the links between the ion beam patterning parameters and the opto-electronic properties of the nucleated dots further and fabricate QD arrays for real IR

applications. An aim could be to produce quantum dot arrays with smaller dots by tuning the patterning and growth parameters. Being not able to pattern larger fields of view (scale of mm) is also a problem at this stage. Rather than extending arrays in 2-dimensional space, stacking up multiple layers of quantum dots may enhance the photoluminescence performance as is often done in self-assembled QD epitaxy and could also be a possible direction for further study. The fabricated quantum dot arrays can produce 2D photonic crystals by nucleating dots at specific sites [69-71], creating a type of periodic dielectric or metallo-dielectric nanostructure with high and low refractive indices. By building materials which have different refractive indices (in 2D or 3D), we can build optical insulators or materials which are completely transparent at a given wavelength only [71]. Furthermore, regular quantum dots can also be used to produce perfect lenses and optical components on the surface of thin metal films [72].

As mentioned in the introduction chapter, FIB has been used as an essential tool in many areas. Since its inception, many new technologies and tools have been added to this platform and this is still continuing. These developments give FIB more flexibility to be applied over wider areas. Nowadays, research projects in engineering and science have more interest in nano- rather than micrometre scale structures and FIB has always been a technology to operate on that sub-micrometre scale. FIB instrumentation, therefore, has a very bright future.

Reference

[1] M. W. Phaneuf, "Applications of focused ion beam microscopy to materials science specimens," *Micron,* vol. 30, pp. 277-288, Jun 1999.

[2] S. Matsui and Y. Ochiai, "Focused ion beam applications to solid state devices," *Nanotechnology,* vol. 7, pp. 247-258, Sep 1996.

[3] I. J. Luxmoore, I. M. Ross, A. G. Cullis, P. W. Fry, J. Orr, P. D. Buckle, and J. H. Jefferson, "Low temperature electrical characterisation of tungsten nano-wires fabricated by electron and ion beam induced chemical vapour deposition," *Thin Solid Films,* vol. 515, pp. 6791-6797, Jun 2007.

[4] S. Nagamachi, M. Ueda, and J. Ishikawa, "Focused ion beam direct deposition and its applications," *Journal of Vacuum Science & Technology B,* vol. 16, pp. 2515-2521, Jul-Aug 1998.

[5] R. G. Forbes, "Understanding how the liquid-metal ion source works," *Vacuum,* vol. 48, pp. 85-97, Jan 1997.

[6] A. Wagner and T. M. Hall, "Liquid gold ion-source," *Journal of Vacuum Science & Technology,* vol. 16, pp. 1871-1874, 1979.

[7] D. R. Kingham and L. W. Swanson, "Sharp of a Liquid Metal Ion Source," *Appl. Phys.,* vol. A 34, pp. 123-132, 1984.

[8] F. A. Stevie, L. A. Giannuzzi, and B. I. Prenitzer, "The Focused Ion Beam Instrument," in *Introduction to focused ion beams: instrumentation, theory, techniques, and practice*, L. A. Giannuzzi and F. A. Stevie, Eds., ed New York: Springer, 2005, pp. 1-12.

[9] C. A. Volkert and A. M. Minor, "Focused ion beam microscopy and micromachining," *Mrs Bulletin,* vol. 32, pp. 389-395, May 2007.

[10] A. Benninghoven, "Surface-analysis by secondary-ion mass-spectrometry (SIMS)," *Surface Science,* vol. 299, pp. 246-260, Jan 1994.

[11] G. Gillen and S. Roberson, "Preliminary evaluation of an SF5+ polyatomic primary ion beam for analysis of organic thin films by secondary ion mass spectrometry," *Rapid Communications in Mass Spectrometry,* vol. 12, pp. 1303-1312, 1998.

[12] R. H. Livengood, S. Tan, R. Hallstein, J. Notte, S. McVey, and F. H. M. F. Rahman, "The neon gas field ion source-a first characterization of neon nanomachining properties," *Nuclear Instruments & Methods in Physics Research Section a-Accelerators Spectrometers Detectors and Associated Equipment,* vol. 645, pp. 136-140, Jul 21 2011.

[13] V. N. Tondare, "Quest for high brightness, monochromatic noble gas ion sources," *Journal of Vacuum Science & Technology A,* vol. 23, pp. 1498-1508, Nov-Dec 2005.

[14] *From the IMSA-100 system to the IMSA-Orsay-Physics-FIB*. Available: http://www.hzdr.de/db/Cms?pOid=23615&pNid=0

[15] L. Wang, "Design optimization for two lens focused ion beam columns," *Journal of Vacuum Science & Technology B,* vol. 15, pp. 833-839, Jul-Aug 1997.

[16] P. Kruit and X. R. Jiang, "Influence of Coulomb interactions on choice of magnification, aperture size, and source brightness in a two lens focused ion beam column," *Journal of Vacuum Science & Technology B,* vol. 14, pp. 1635-1641, May-Jun 1996.

[17] Y. Peng, T. Cullis, and B. Inkson, "Bottom-up Nanoconstruction by the Welding of Individual Metallic Nanoobjects Using Nanoscale Solder," *Nano Letters,* vol. 9, pp. 91-96, Jan 2009.

[18] Y. Peng, T. Cullis, and B. Inkson, "Accurate electrical testing of individual gold nanowires by in situ scanning electron microscope nanomanipulators," *Applied Physics Letters,* vol. 93, Nov 2008.

[19] J. F. Ziegler. (10/2/2013). www.srim.org.

[20] L. A. Giannuzzi, B. I. Prenitzer, and B. W. Kemshall, "Ion - solid interactions," in *Introduction to Focused Ion Beams : Instrumentation, Theory, Techniques, and Practice*, ed New York: Springer, 2005, pp. 13-52.

[21] *List of Periodic Table Elements Sorted by Atomic Number*. Available: http://www.science.co.il/PTelements.asp

[22] J. Gierak, D. Mailly, G. Faini, J. L. Pelouard, P. Denk, F. Pardo, J. Y. Marzin, A. Septier, G. Schmid, J. Ferre, R. Hydman, C. Chappert, J. Flicstein, B. Gayral, and J. M. Gerard, "Nano-fabrication with focused ion beams," *Microelectronic Engineering,* vol. 57-8, pp. 865-875, Sep 2001.

[23] F. Rinaldi, "Basic of Molecular Beam Epitaxy (MBE)," *Annual Report 2002, Optoelectronics Department, University of Ulm,* 2002.

[24] G. Biasiol and L. Sorba, "Molecular Beam Epitaxy: Principles and Applications," in *Crystal growth of materials for energy production and energy-saving applications*, R. Fornari and L. Sorba, Eds., ed: Edizioni ETS, Pisa, 2001, pp. 66-83.

[25] M. Gutierrez, M. Hopkinson, H. Y. Liu, A. I. Tartakovskii, M. Herrera, D. Gonzalez, and R. Garcia, "Critical barrier thickness for the formation of InGaAs/GaAs quantum dots," *Materials Science & Engineering C-Biomimetic and Supramolecular Systems,* vol. 25, pp. 798-803, Dec 2005.

[26] M. Sugawara, *Self-assembled InGaAs/GaAs quantum dots*. San Diego, Calif. ; London: Academic Press, 1999.

[27] N. Vladov, J. Segal, and S. Ratchev, "Measuring the apparent beam size of focused ion beam (FIB) systems," in *EMC2012*, Manchester, United Kingdom, 2012.

[28] S. P. Robert Fisher, Ashley Walker and Erik Wolfart. (2000, 1 June). *Fourier Transform*.

[29] J. Li, T. Malis, and S. Dionne, "Recent advances in FIB-TEM specimen preparation techniques," *Materials Characterization,* vol. 57, pp. 64-70, Jul 2006.

[30] L. A. Giannuzzi and F. A. Stevie, "A review of focused ion beam milling techniques for TEM specimen preparation," *Micron,* vol. 30, pp. 197-204, Jun 1999.

[31] H. Amari, L. Lari, H. Y. Zhang, L. Geelhaar, C. Cheze, M. J. Kappers, C. McAleese, C. J. Humphreys, and T. Walther, "Accurate calibration for the quantification of the Al content in AlGaN epitaxial layers by energy-dispersive X-ray spectroscopy in a Transmission Electron Microscope," presented at the 17th International Conference on Microscopy of Semiconducting Materials 2011, 2011.

[32] H. Amari, H. Y. Zhang, L. Geelhaar, C. Cheze, M. J. Kappers, and T. Walther, "Nanoscale EELS analysis of elemental distribution and band-gap properties in AlGaN epitaxial layers," in *17th International Conference on Microscopy of Semiconducting Materials 2011*. vol. 326, T. Walther and P. A. Midgley, Eds., ed, 2011, p. 012028.

[33] T. Ishitani, H. Tsuboi, T. Yaguchi, and H. Koike, "Transmission electron-microscope sample preparation using a fouced ion-beam," *Journal of Electron Microscopy,* vol. 43, pp. 322-326, Oct 1994.

[34] Y. B. Zou, B. Schillinger, S. Wang, X. S. Zhang, Z. Y. Guo, and Y. R. Lu, "Coded source neutron imaging with a MURA mask," *Nuclear Instruments & Methods in Physics Research Section a-Accelerators Spectrometers Detectors and Associated Equipment,* vol. 651, pp. 192-196, Sep 2011.

[35] S. Wang, Y. Zou, X. Zhang, Y. Lu, and Z. Guo, "Coded source imaging simulation with visible light," *Nuclear Instruments & Methods in Physics Research Section a-Accelerators Spectrometers Detectors and Associated Equipment,* vol. 651, pp. 187-191, Sep 21 2011.

[36] S. R. Gottesman and E. E. Fenimore, "New family of binary arrays of coded aperture imaging," *Applied Optics,* vol. 28, pp. 4344-4352, Oct 15 1989.

[37] D. Calabro and J. K. Wolf, "On synthesis of 2-dimensional arrays with desirable correlation properies," *Information and Control,* vol. 11, p. 537, 1967.

[38] S. Franchi, G. Trevisi, L. Seravalli, and P. Frigeri, "Quantum dot nanostructures and molecular beam epitaxy," *Progress in Crystal Growth and Characterization of Materials,* vol. 47, pp. 166-195, 2003.

[39] P. Bhattacharya, S. Ghosh, and A. D. Stiff-Roberts, "Quantum dot opto-electronic devices," *Annual Review of Materials Research,* vol. 34, pp. 1-40, 2004.

[40] N. L. Dias, A. Garg, U. Reddy, J. D. Young, V. B. Verma, R. P. Mirin, and J. J. Coleman, "Directed self-assembly of InAs quantum dots on nano-oxide templates," *Applied Physics Letters,* vol. 98, Apr 4 2011.

[41] J. Lee, T. W. Saucer, A. J. Martin, D. Tien, J. M. Millunchick, and V. Sih, "Photoluminescence Imaging of Focused Ion Beam Induced Individual Quantum Dots," *Nano Letters,* vol. 11, pp. 1040-1043, Mar 2011.

[42] J. Wang, J. Yuan, F. W. M. v. Otten, and R. Notzel, "Combining selective area growth and self-organized strain engineering for site-controlled local InAs/InP quantum dot arrays," *Journal of Crystal Growth,* vol. 335, pp. 25-27, 2011.

[43] J. L. Gray, R. Hull, and J. A. Floro, "Periodic arrays of epitaxial self-assembled SiGe quantum dot molecules grown on patterned Si substrates," *Journal of Applied Physics,* vol. 100, Oct 2006.

[44] X. Li and G. Ouyang, "Thermodynamic theory of controlled formation of strained quantum dots on hole-patterned substrates," *Journal of Applied Physics,* vol. 109, May 1 2011.

[45] S. Jeppesen, M. S. Miller, D. Hessman, B. Kowalski, I. Maximov, and L. Samuelson, "Assembling strained InAs islands on patterned GaAs substrates with chemical beam epitaxy," *Applied Physics Letters,* vol. 68, pp. 2228-2230, Apr 15 1996.

[46] T. Ishikawa, T. Nishimura, S. Kohmoto, and K. Asakawa, "Site-controlled InAs single quantum-dot structures on GaAs surfaces patterned by in situ electron-beam lithography," *Applied Physics Letters,* vol. 76, pp. 167-169, Jan 10 2000.

[47] S. Kalliakos, C. P. Garcia, V. Pellegrini, M. Zamfirescu, L. Cavigli, M. Gurioli, A. Vinattieri, A. Pinczuk, B. S. Dennis, L. N. Pfeiffer, and K. W. West, "Photoluminescence of individual doped GaAs/AlGaAs nanofabricated quantum dots," *Applied Physics Letters,* vol. 90, Apr 30 2007.

[48] S. Y. Chou, P. R. Krauss, and P. J. Renstrom, "Imprint of sub-25 nm vias and trenches in ploymers," *Applied Physics Letters,* vol. 67, pp. 3114-3116, Nov 20 1995.

[49] K. Pond, R. Maboudian, V. Bresslerhill, D. Leonard, X. S. Wang, K. Self, W. H. Weinberg, and P. M. Petroff, "Scanning-tunneling-microscopy of flat and vicinal molecular-beam expitaxy-grown GaAs(001)-(2x4) surface - The effect of growthrate," *Journal of Vacuum Science & Technology B,* vol. 11, pp. 1374-1378, Jul-Aug 1993.

[50] H. Hiroshima and M. Komuro, "Control of bubble defects in UV nanoimprint," *Japanese Journal of Applied Physics Part 1-Regular Papers Brief Communications & Review Papers,* vol. 46, pp. 6391-6394, Sep 2007.

[51] J. M. Gerard, B. Sermage, B. Gayral, B. Legrand, E. Costard, and V. Thierry-Mieg, "Enhanced spontaneous emission by quantum boxes in a monolithic optical microcavity," *Physical Review Letters,* vol. 81, pp. 1110-1113, Aug 3 1998.

[52] C.-C. Cheng, K. Meneou, and K. Y. Cheng, "Effects of nano-pattern size on the property of InAs site-controlled quantum dots," *Journal of Crystal Growth,* vol. 323, pp. 180-182, May 15 2011.

[53] M. Mehta, D. Reuter, A. Melnikov, A. D. Wieck, and A. Remhof, "Focused ion beam implantation induced site-selective growth of InAs quantum dots," *Applied Physics Letters,* vol. 91, p. 123108, Sep 17 2007.

[54] S. Kiravittaya and O. G. Schmidt, "Growth of three-dimensional quantum dot crystals on patterned GaAs (001) substrates," *Physica E-Low-Dimensional Systems & Nanostructures,* vol. 23, pp. 253-259, Jul 2004.

[55] D. Leonard, K. Pond, and P. M. Petroff, "Critical layer thickness for self-assembled InAs islands on GaAs," *Physical Review B,* vol. 50, pp. 11687-11692, Oct 15 1994.

[56] T. Walther, A. G. Cullis, D. J. Norris, and M. Hopkinson, "Nature of the Stranski-Krastanow transition during epitaxy of InGaAs on GaAs," *Physical Review Letters,* vol. 86, pp. 2381-2384, Mar 12 2001.

[57] D. R. Kingham and L. W. Swanson, "Shape of a liquid-metal ion source - A dynamic-model including fluid-flow and space-charge effects," *Applied Physics a-Materials Science & Processing,* vol. 34, pp. 123-132, 1984 1984.

[58] D. Leonard, S. Fafard, K. Pond, Y. H. Zhang, J. L. Merz, and P. M. Petroff, "Structural and optical-properties of self-assembled InGaAs quantum dots," *Journal of Vacuum Science & Technology B,* vol. 12, pp. 2516-2520, Jul-Aug 1994.

[59] R. Hull, J. Floro, J. Graham, J. Gray, M. Gherasimova, A. Portavoce, and F. M. Ross, "Synthesis and functionalization of epitaxial quantum dot nanostructures for nanoelectronic architectures," *Materials Science in Semiconductor Processing,* vol. 11, pp. 160-168, Oct 2008.

[60] R. Hull, J. A. Floro, M. Gherasimova, J. F. Graham, J. L. Gray, A. Portavoce, F. M. Ross, and J. Thorp, "Bridging the length scales between lithographic patterning and self assembly mechanisms in fabrication of semiconductor nanostructure arrays," in *16th International Conference on Microscopy of Semiconducting Materials*. vol. 209, T. Walther, P. D. Nellist, J. L. Hutchison, and A. G. Cullis, Eds., ed, 2010, p. 012003.

[61] R. Hull, J. A. Floro, M. Gherasimova, J. F. Graham, J. L. Gray, A. Portavoce, F. M. Ross, and J. Thorp, "Bridging the length scales between lithographic patterning and self assembly mechanisms in fabrication of semiconductor nanostructure arrays," *16th International Conference on Microscopy of Semiconducting Materials,* vol. 209, 2010.

[62] J. Y. Lee, M. J. Noordhoek, P. Smereka, H. McKay, and J. M. Millunchick, "Filling of hole arrays with InAs quantum dots," *Nanotechnology,* vol. 20, p. 285305, Jul 15 2009.

[63] M. Srujan, K. Ghosh, S. Sengupta, and S. Chakrabarti, "Presentation and experimental validation of a model for the effect of thermal annealing on the photoluminescence of self-assembled InAs/GaAs quantum dots," *Journal of Applied Physics,* vol. 107, p. 123107, Jun 15 2010.

[64] T. Nakaoka, T. Saito, J. Tatebayashi, and Y. Arakawa, "Size, shape, and strain dependence of the g factor in self-assembled In(Ga)As quantum dots," *Physical Review B,* vol. 70, p. 235337, Dec 2004.

[65] L. H. Li, E. H. Linfield, R. Sharma, and A. G. Davies, "In-assisted desorption of native GaAs surface oxides," *Applied Physics Letters,* vol. 99, p. 061910, Aug 8 2011.

[66] M. Rosini, M. C. Righi, P. Kratzer, and R. Magri, "Indium surface diffusion on InAs (2x4) reconstructed wetting layers on GaAs(001)," *Physical Review B,* vol. 79, p. 075302, Feb 2009.

[67] L. Holzer, F. Indutnyi, P. H. Gasser, B. Munch, and M. Wegmann, "Three-dimensional analysis of porous BaTiO3 ceramics using FIB nanotomography," *Journal of Microscopy-Oxford,* vol. 216, pp. 84-95, Oct 2004.

[68] R. Kometani, T. Hoshino, K. Kanda, Y. Haruyama, T. Kaito, J. Fujita, M. Ishida, Y. Ochiai, and S. Matsui, "Three-dimensional high-performance nano-tools fabricated using focused-ion-beam chemical-vapor-deposition," *Nuclear Instruments & Methods in Physics Research Section B-Beam Interactions with Materials and Atoms,* vol. 232, pp. 362-366, May 2005.

[69] K. Sakoda, *Optical Properties of Photonic Crystal*, Second Edition ed. Germany: Springer, 2005.

[70] G. Parker and M. Charlton, "Photonic crystals," *Physics World,* vol. 13, pp. 29-34, Aug 2000.

[71] T. Krauss, "Photonic crystals shine on," *Physics World,* vol. 19, pp. 32-36, Feb 2006.

[72] B. Barnes and R. Sambles, "Metal surfaces light up," *Physics World,* vol. 19, pp. 17-21, Jan 2006.